ANALYSIS AND DESIGN OF COMPACT LOW PROFILE ANTENNAS FOR FIXED VOLUME APPLICATIONS

BY

CARLO VAN NIEKERK

DISSERTATION

Submitted in partial fulfillment of the requirements
for the degree of Doctor of Philosophy in Electrical and Computer Engineering
in the Graduate College of the
University of Illinois at Urbana-Champaign, 2013

Urbana, Illinois

Doctoral Committee:

Professor Jennifer T. Bernhard, Chair
Professor Andreas Cangellaris
Professor Steven J. Franke
Professor Jose E. Schutt-Aine

ABSTRACT

In this document we have accomplished a number of tasks that bring value to the field. A circuit analysis was performed on a transmission line based metamaterial antenna (in particular, the Infinite Wavelength Resonant Antenna or IWRA). It was discovered that the antenna works in similar manner to traditional coupled transmission lines. In fact, further investigation using characteristic mode theory showed that the IWRA could be thought of simply as two closely coupled Planar Inverted-F Antennas (PIFAs) that are proximity-couple fed.

The concept of a Dual Reactively Loaded Monopole (DRLM) antenna is introduced, an antenna that features capacitive and inductive loading components. This new design allows for miniaturized performance with the benefit of tunability. The implementation of the DRLM antenna where the inductive loading is achieved by a lumped inductor as opposed to the conventional distributed copper strip shows relatively good performance when compared to the fundamental limit. This study demonstrates the viability of inductive loading by lumped element for radiating structures. The optimum position for the lumped inductor is determined by experimental means. The DRLM antenna with reduced height profile is analyzed, and it is determined that the antenna architecture is not well suited to extreme low profile applications (e.g., short-fat topology). Finally, a Stacked DRLM antenna is designed for the purpose of achieving wider impedance bandwidth. The final design has a bandwidth more than double the original single mode DRLM antenna, though now the tunability is limited. All antennas discussed are compared to the theoretical limits for antenna performance, and specific antenna structures are evaluated against Gustafsson's limit for the appropriate volume that best describes the antenna geometry. This presents a more realistic performance comparison than the spherical volume counterpart, Chu's limit.

To my wife, Leigh-Anne, for your love and support. Also to our beautiful daughter, Emily, for providing the impetus to keep working hard.

ACKNOWLEDGMENTS

First, I would like to thank my adviser, Professor Jennifer T. Bernhard, for the helpful advice and support she has provided me for the past few years of graduate school. Many times we would have meetings in her office and discussed theories or ideas to forward the project when it had seemingly stalled. Professor Bernhard was particularly successful in convincing me to not be discouraged by small detail problems and to instead focus on the big picture solutions. She has also been there to advise on issues outside of research, regarding career, job opportunities and family life.

Second, I want to thank the members of the Antenna Lab. The environment in the group is one that promotes creative thinking, hard work and also lots of fun. Our group meetings where we give constructive commentary on each others work was a particularly helpful exercise. A special mention to Dr. Jake Adams, Dr. Mike Daly and Dr. Tyrone Roach who as senior members of the group have often helped me understand difficult concepts and brain-storm solutions. I really appreciate and value the friendship of every member of the group.

Last but by no means least I would like to express by thanks and appreciation to my wife, Leigh-Anne. I could not have completed any of this without the love and support from her. Her support and words of encouragement have always been the fuel that kept me going through the high and low times. Thank you my love. Emily is too young to realize this but she got me through some long nights in the office, sometimes just staring at her picture would make me smile and feel that I could carry on for bit longer.

TABLE OF CONTENTS

CHAPTER 1

INTRODUCTION

Wireless systems are ubiquitous in everyday life, with a multitude of work-related or recreational applications. Even more applications for wireless system can be found in the military (or defense) sectors. Commercial applications include Wi-Fi, GPS, Cellular, Bluetooth, Satellite Comms and RFID (Asset Tracking). Defense-related applications include Mobile *ad hoc* Network (MANET), combat identification (CID), Unmanned Vehicles (UAVs) and body-wearable systems. For many, these applications have made life a little more convenient and represent items of necessity rather than luxury. This is because some of these services have brought about unprecedented access to information. Motivating research in this area is relatively easy given the broad array of applications in many markets. The value and growth of these market areas are substantial, incentivizing further research and development. For example, many businesses these days are relying on technologies like RFID to promote efficient locating and tracking of inventory or assets. The RFID market has seen robust growth, in fact, there are global market analysis reports that forecast a compound annual growth rate of 17% for the period 2011-2013 to a value of US$ 9.7 Billion [1].

One device that is integral to all wireless systems is the antenna. The antenna is a device that acts as a transducer between the guided transmission medium to the unguided (free space) propagating medium. Many antennas used in wireless applications are derived from microstrip antennas, also commonly known as "patch antennas." Patch antennas have many attractive attributes, namely that they are low-profile, conformal, easy to fabricate, low cost, and they are well-suited to integration with circuitry. These antennas are, however, notoriously narrow band due to their resonant operation.

Due to the big push for mobility and increased services in one package, the requirements of the antenna in the system have become more demanding. For example, in a cellular handset numerous services (like GPS, Wi-Fi, Bluetooth, etc.) need to be performed either using a complicated multifunction antenna or numerous antennas carefully distributed in the package. Increased system complexity often translates to increasing package volume designated for non-antenna hardware with a shrinking total package volume as devices are generally trending smaller in order to promote portability. Thus, the conventional patch antenna is too large (length $\approx \lambda/2$) for modern packages and has to be miniaturized to comply with package integration. This can be challenging, since the antenna performance as an efficient radiator is directly related to the volume it occupies relative to its operating wavelength. Also, as the antenna size is reduced, the ability to couple energy into the antenna from a guided transmission line is compromised because the resistance presented by the antenna trends lower while the reactance increases (i.e., the antenna looks like a capacitor) [2].

1.1 Goals and Impact

The goal for this research was to develop an understanding on how to best miniaturize a low profile antenna for a given set volume. Though the topic of miniaturizing planar antennas is one that has generated lots of interest [3], many researchers simply report miniaturization results without considering the electrical size and antenna performance [4]. The first half of this document focuses on an antenna (regarded by some to be a "metamaterial antenna") that has generated buzz for its apparent characteristics and its ability to miniaturize antenna structures. Our goal with this structure is to determine its operation using traditional analysis methods, and consequently deduce the source for miniaturization. The second half of this research is dedicated to the development of a compact low profile antenna using reactive loading and comparison of its performance to the fundamental limits.

This research has impact on the field of antennas and electromagnetics in numerous ways. First, an analysis approach for describing the operation of a metamaterial antenna which is based on coupled line theory. The analysis

involves the development of a circuit model, an approach which can easily be adopted for similar structures. Second, the fundamental concepts of reactive loading are leveraged to create an antenna geometry that supports increasing levels of miniaturization without increasing the antenna physical size. Third, the performance for lumped inductor loading is observed to be an adequate method for implementation. Also, a detailed formulation into the consequences of a height reduction is performed in order to establish the primary drivers behind performance degradation. Finally, a broadband design using the original antenna structure in a stacked topology is developed and optimized.

1.2 Outline

Chapter 2 focuses on general topics related to small antennas and a historical overview of the progress attained in the study of small antennas theory for the past few decades. In Chapter 3, the theory of characteristic modes is introduced and an example is provided in order to demonstrate its use for practical applications. This tool is used throughout this document for analysis purposes. A specific antenna, known as "Infinite Wavelength Resonant Antenna (IWRA)" is analyzed, a circuit model is developed and a traditional transmission line analysis is performed in Chapter 4. Claims on miniaturization, performance and operation are investigated. Miniaturization of low profile antennas using reactive loading is the topic of Chapter 5. This leads into the development and performance evaluation of the Dual Reactively Loaded Monopole (DRLM) antenna in Chapter 6. Finally, in Chapter 7 we conclude by highlighting the most impactful contributions this work has delivered as well as offering some direction for future work.

CHAPTER 2

SMALL ANTENNA THEORY

A convenient way to describe an antenna's size is to completely enclose the antenna by a sphere, so that the largest dimension of the antenna is roughly equal to the sphere diameter. This sphere is also known as the "Chu Sphere" [5]. The electrical size of the antenna is then given by the wavenumber, k, multiplied by the sphere radius, a (i.e., electrical size = ka). Figure 2.1 shows pictorially how the Chu sphere is defined for dipole-like antennas.

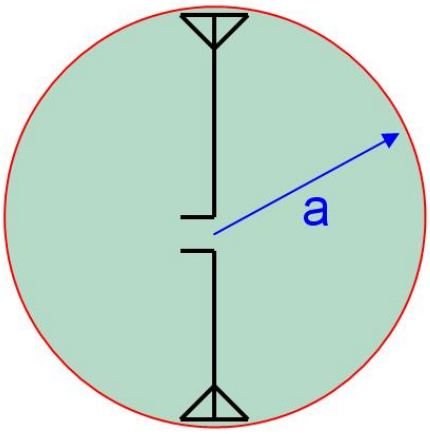

Figure 2.1: Chu Sphere for Dipole-like Antennas

The definition for the Chu sphere is more complicated for monopole-like antennas that require a large (relative to the antenna element) ground plane for operation. It is generally accepted that if the finite ground plane is large enough so that the antenna impedance characteristics are similar to the infinite ground plane case, then the dimensions of the ground plane do not need to be included in the definition of a and the largest dimension of the antenna would suffice [6]. In other words, for an antenna with a large ground plane, the sphere simply encloses the antenna along with its image, as defined by image theory, as shown in Figure 2.2.

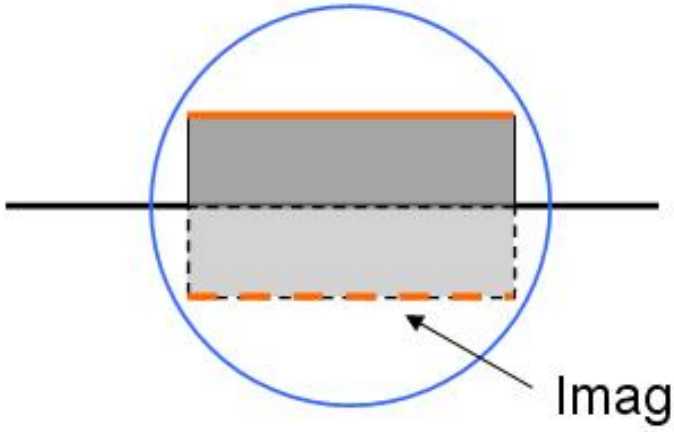

Figure 2.2: Chu Sphere for Monopole-like Antennas

An antenna is termed an electrically small antenna (ESA) if it has electrical size, $ka < 0.5$. Note: the terms "electrically small antenna" and "small antenna" are used interchangeably in this document and in the field, and refer to the case where the antenna occupies a Chu sphere with $ka < 0.5$.

2.1 Historical Overview of Small Antennas

One of the first people to investigate the correlation between antenna performance and antenna electrical size was Wheeler [2, 7, 8]. Wheeler's early work involved the analysis of two distinct simplified antenna types, namely, the capacitive (parallel plate capacitor) and inductive (coil inductor) small antenna that occupies equivalent cylindrical volumes. He quantified the radiation capabilities in terms of the so-called "radiation power factor" (RPF), which is the ratio of the radiated power to reactive power. The derived expression for the RPF shows a direct relation to the cylindrical volume enclosing the antenna and also the extent to which the volume is utilized by the antenna (given by the shape factor). Wheeler's definitions for radiation power factor can be seen as the inverse of quality factor (Q) for RC or RL circuits (antenna circuit models). The inverse of the RPF gives a good approximation for the minimum antenna Q (or maximum bandwidth) that relates well with

more elaborate methods derived by subsequent authors. Wheeler's work can only be used as a rough approximation, with the accuracy improving for very small antenna sizes. The inaccuracies for larger antenna sizes are due to the fact that his analysis does not account for higher order radiated spherical modes.

Though it is noted that Wheeler's RPF relates to the traditional circuit Q, his analysis did not specifically examine antenna Q as a fundamental property of small antennas. The fundamental relationship between antenna Q and electrical size was addressed in the seminal paper by Chu [9] in which he derived the minimum Q limit for omnidirectional antennas enclosed in a sphere around the antenna (i.e., Chu sphere). Chu's analysis involved describing a radiated field generated by sources distributed over a spherical surface as the sum of spherical wave modes. Chu proposed that since these spherical wave modes possess the property of orthogonality and thus there exists no coupling between any two spherical waves outside the antenna sphere, it would be possible that they be replaced by a number of independent equivalent circuits. In so doing, the space problem has been transformed into a circuit problem. Thus the antenna Q can be obtained by analyzing the equivalent network. Chu's analysis is specifically on omnidirectional antennas but many authors have followed and expanded on his analysis to other antenna types. Hansen simplified Chu's expression for minimum Q in [10]. Harrington [11] was the first to expand on Chu's analysis to include antennas radiating in both TE and TM modes. This work by Harrington eventually led to a lower minimum Q limit.

Earlier work (Chu and Harrington) produced approximate results for the minimum Q limit because they are based on analysis of equivalent circuits which model the radiated field when represented as spherical wave modes. The exact expression for antenna Q was derived by Collin and Rothschild [12], whose method involves determining the magnetic and electric energy by subtracting the energy density associated with power flow from the total energy density. Their analysis was confined to antennas radiating in TE or TM modes only. A more general result was presented by Fante [13], expressing the exact Q for a TM and TE configuration.

In the past decade, work by Best et al. [6, 14–18] in the small antenna domain has been comprehensive in terms of theory and design. The largest contribution to this topic has been the expression for approximate and exact radiation Q represented in terms of fields and impedance, and also determining a more precise relationship between Q and bandwidth [14]. Other work in this area involves researching specific antennas that approached the minimum Q limit (specifically self-resonant wire antennas). Studies into how wire geometry, wire folding and volume utilization would affect the antenna radiation resistance and Q were also undertaken [15]. A more restrictive radiation Q was determined by Thal [19], where he extended Chu's equivalent mode circuit approach by introducing an additional equivalent circuit to account for the energy stored inside the antenna sphere (previously assumed by Chu and others to be essentially zero). Thal also studied the relationship between gain, Q, and the energy inside the antenna sphere for a small antenna, with conclusions that they are indeed not independent of one another [20]. More recently, Gustafsson and his colleagues [21] derived Q and gain expressions for arbitrarily shaped small antennas. His novel approach involved using scattering theory to examine antenna Q. He showed that the theoretical limit on radiation Q increases for any shape that deviated from the ideal spherical shape and that maximum performance is achieved for shapes with aspect ratios between 1 and 2. The aspect ratio is defined as the ratio of the antenna's largest to smallest dimension.

2.2 Characteristics of Small Antennas

2.2.1 Directivity or Radiation Field Pattern

Small antennas approach the doughnut-shaped omni-directional radiation pattern of a Hertzian dipole with directivity, $D = 1.5$.

2.2.2 Radiation Efficiency

An antenna's radiation efficiency (η) describes how well energy accepted at its input is radiated into free space. Alternatively, it is the ratio of the power radiated by the antenna to the power delivered to the input terminals of the

antenna. The portion of energy that is accepted by the antenna and not radiated is lost in the antenna structure itself according to the conservation of energy principle. The energy loss manifests itself by heating the structure. There are two primary sources for the energy loss, conduction losses in the conductive parts and dielectric losses in lossy dielectric media. The loss mechanism is typically modeled as a series resistance, R_{loss}. The radiation efficiency η can be expressed as

$$\eta = \frac{R_{rad}}{R_{rad} + R_{loss}} = \frac{R_{rad}}{R_A} \tag{2.1}$$

where R_A is the total antenna input resistance, and is the summation of loss resistance (R_{loss}) and the radiation resistance (R_{rad}). As the antenna size (ka) decreases, the radiation resistance (R_{rad}) decreases and R_{loss} dominates in Equation 2.1. This results in lower radiation efficiency.

A practical method for determining the radiation efficiency η by separating R_{rad} from R_A was introduced by Wheeler and is known as the *Wheeler Cap* method [8]. The Wheeler cap is a spherical electric conducting shell that is approximately the size of a radiansphere (radius = $\lambda/2\pi$). Note the size and shape of the cap does not have to be exact [5]. Rather, it should be large enough so as to not unduly disturb antenna near fields while still preventing radiation, and small enough so that the spherical cavity resonances are not excited. Measurement of the radiation efficiency involves two impedance measurements (using a Vector Network Analyzer, VNA) at the operating frequency, with and without the cap over the antenna. The measurement without the cap allows R_A to be obtained, while with the cap we determine R_{loss} and consequently both η and R_{rad} can be computed.

2.2.3 Radiation Quality Factor (Q)

The radiation quality factor is a critical parameter for small antennas. This is because the fundamental performance limitations on small antennas are given by its radiation Q. The antenna Q is given by

$$Q = \frac{2\omega_0 max(W_E, W_M)}{P_A} \tag{2.2}$$

where W_E and W_M are the time-averaged stored electric and magnetic energies, and P_A is the antenna received power. The radiated power, $P_{rad} = \eta P_A$ where as before η is the antenna radiation efficiency. As an approximation, the relationship between Q and the 3 dB fractional bandwidth B is given by

$$Q \approx \frac{1}{B} \quad \text{for} \quad Q \gg 1 \tag{2.3}$$

Note this approximation improves as Q becomes larger. A more precise relationship between bandwidth and Q was derived by Yaghjian and Best [14]

$$B \equiv \frac{1}{Q}\frac{s-1}{\sqrt{s}} \tag{2.4}$$

where s is the maximum allowable voltage standing wave ratio (VSWR). As the antenna size decreases the radiation Q increases. For electrically small antennas, a fundamental limit for the minimum Q exists (assuming a singly resonant antenna) that is physically possible to attain given its enclosing sphere's electrical size.

2.2.4 Input Impedance

As a generalization, the input impedance of a small antenna will typically have a low resistance and high reactance [22]. As the antenna size decreases the radiation resistance R_{rad} decreases and thus X_A is the dominant term in antenna input impedance Z_A $(= R_A + jX_A)$. Hence, matching circuits are required to be able to operate antennas more efficiently. The use of external matching circuitry requires a physically small footprint which can be an issue in some cases. Thus it is desired to have self-resonant antennas. Some small antennas based on folding (or meandering) methods have produced antenna input impedances that approach commercial transmission line characteristic impedances (i.e., $Z_0 = 50\ \Omega$) [15].

2.2.5 Characteristics for Optimum Performance

Sievenpiper [4] has recently published a paper where numerous published papers with claims on small antenna performance are compared. The paper has a convenient chart showing the performance percentage bandwidth-efficiency

product ($B\eta$) as a function of electrical size (ka) and is compared the theoretical limit (shown in Figure 2.3).

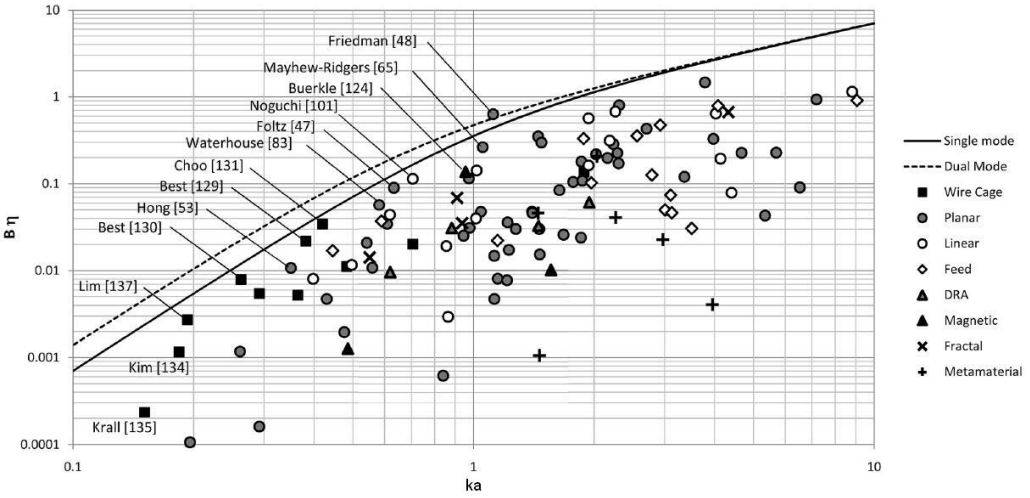

Figure 2.3: Sievenpiper Performance Chart [4]

As can be seen, wire cage antennas generally have the performance upper hand over other antenna types. It is interesting to note that planar antennas do well in approaching the theoretical limit for moderately sized antennas ($ka \sim 1$). Also, no electrically small antennas ($ka < 0.5$) is this study exceeded the $B\eta$ limit. It is noted that the optimum performance is approached if (1) any dielectric material constant (if used) is as low as possible, (2) the aspect ratio is close to unity, and (3) the fields fill the minimum size enclosing sphere with a great degree of uniformity.

2.3 Fundamental Performance Limit of Small Antennas

As shown by the historical overview, much work in the area of small antennas has been related to the exact formulation of the antenna performance for a given antenna electrical size. The antenna performance for small antennas is given by the antenna Q and the antenna electrical size is described by its ka value. The most widely cited version of the theorectical limit was derived by Chu [9] and is given by:

$$Q = \frac{1}{ka} + \frac{1}{n(ka)^3} \tag{2.5}$$

where n = 1 (single mode) and 2 (dual mode = both TE and TM modes). Using Equation 2.4 we can express Equation 2.5 in terms of the bandwidth-efficiency product. Note: Equation 2.6 shows the expression for bandwidth(B)-efficiency(η) for a VSWR value equal to 2.

$$B\eta = \frac{1}{\sqrt{2}} \left(\frac{1}{ka} + \frac{1}{n(ka)^3} \right)^{-1} \tag{2.6}$$

The Chu limit describes the minimum Q (or maximum bandwidth) that a small antenna can achieve given the size of its enclosed sphere. Most antennas have geometries that do not fully utilize the spherical volume and consequently their performance falls far short of the performance predicted by the theoretical limit. Recently, Gustafsson has developed revised limits for arbitrarily shaped antennas [21]. Gustafsson's limit is based on scattering theory and is given in terms of the quotient, D/Q, where D is the directivity and Q is the antenna Q-factor. For antennas which do not contain any magnetic materials, the limit is given by:

$$\frac{D}{Q} = \frac{\eta k_0^3 \gamma}{2\pi} \tag{2.7}$$

where η is the absorption effiency, which is a bounded value ($0 \leq \eta \leq 1$) and for many resonant antennas $\eta \approx 1/2$ [23]. In Equation 2.7, k_0 is the free space wavenumber and γ is the scattering polarizability dyadic. The polarizabilty dyadic is proportional to the physical area of the antenna as seen by an incident plane wave as well as the polarization of the wave. Though numerical calculation is the preferred method for determining γ, good agreement can be attained using the recently published approximate closed-form expressions which are based on fitted rational functions [24]. Of particular interest for the work in subsequent chapters are the Gustafsson limits for antennas which are best described by cylindrical shapes. Consider a cylinder with height h and diameter d as shown in Figure 2.4.

The expression for the high-contrast polarizability dyadic is given by

$$\gamma_c = \gamma_{ch}(\hat{x}\hat{x} + \hat{y}\hat{y}) + \gamma_{cv}\hat{z}\hat{z} \tag{2.8}$$

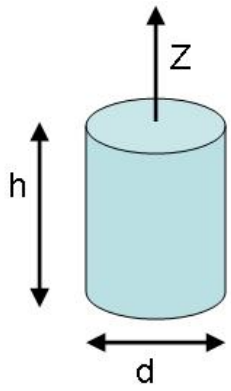

Figure 2.4: Cylindrical Volume

where γ_{ch} and γ_{cv} are the polarizability dyadics for the horizontal and vertical polarizations, respectively. The closed-form expressions are given for two regions of size aspect ratio, where the aspect ratio of the cylindrical volume, $\zeta = h/d$. For $\zeta \leq 1$,

$$\frac{\gamma_{cv}(\zeta)}{a^3} = \zeta \frac{6.241 + 59.056\zeta + 36.097\zeta^2}{1 + 5.2995\zeta - 1.92\zeta^2 + 7.453\zeta^3} \tag{2.9}$$

and for $\zeta > 1$,

$$\frac{\gamma_{cv}(\zeta)}{\gamma_{sv}(\zeta)} = \frac{1.135 + 24.004\zeta^{-1} - 4.355\zeta^{-2}}{1 + 13.851\zeta^{-1} - 6.093\zeta^{-2} + 21.706\zeta^{-3}} \tag{2.10}$$

where $\gamma_{sv}(\zeta)$ is the polarizability dyadic of a spheroid for a vertical polarized incident wave, and is given by

$$\frac{\gamma_{sv}(\zeta)}{a^3} = \frac{4\pi}{3} \frac{e^3}{\ln(1+e) + \ln\zeta - e} \tag{2.11}$$

where

$$e = \sqrt{1 - \zeta^{-2}} \tag{2.12}$$

The polarizability for the horizontal polarization γ_{ch} and $\zeta \leq 1$ is given by

$$\frac{\gamma_{ch}(\zeta)}{a^3} = \frac{16/3 + 59.47\zeta + 28.064\zeta^2}{1 + 6.087\zeta - 2.935\zeta^2 + 9.032\zeta^3} \tag{2.13}$$

and for $\zeta > 1$,

$$\frac{\gamma_{ch}(\zeta)}{a^3} = \zeta^{-2} \frac{12.565 + 13.932\zeta^{-1} - 2.804\zeta^{-2}}{1 + 0.456\zeta^{-1} - 1.1\zeta^{-2} + 0.809\zeta^{-3}} \tag{2.14}$$

Equation 2.7 can be rewritten for antenna Q as

$$Q = \frac{2\pi D}{\eta k_0^3 \gamma} \tag{2.15}$$

and thus a larger γ will result in a lower Q (or conversely larger bandwidth). Given the aspect ratio, the minimum Q is calculated using the largest γ from either polarization (horizontal or vertical). Note for the cylinder aligned with the z-axis as shown in Figure 2.4, a long thin cylinder (e.g., dipole antenna) will have $\gamma_{cv} > \gamma_{ch}$ while the opposite is true for a short, fat cylinder (e.g., circular patch antenna). For the sake of computing the Gustafsson limit, a directivity of 1.5 for small antennas is usually a good approximation. Finally, Equation 2.4 can be used to compute the bandwidth-efficiency product for Gustafsson's limit. A comparison between Gustafsson's limit for $\zeta = 1$ and Chu's limit is shown in Figure 2.5.

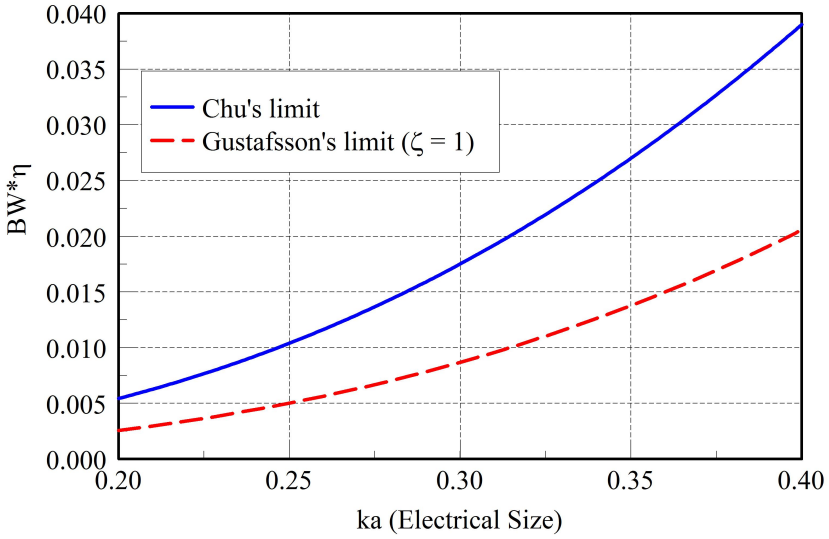

Figure 2.5: Comparison between the Chu and Gustafsson Limit

The maximum performance as described by the bandwidth-efficiency product is substantially less for Gustafsson's limit compared to the Chu limit. This is because the cylindrically shaped antenna will not utilize a spherical volume optimally. For small *ka*, the two limits converge while they diverge from one another for large values of *ka*.

It is possible to exceed the limit defined by Gustafsson (and/or Chu) if multiple resonant mode antennas are considered. This is because the theo-

retical limit is based on a singly resonant antenna (i.e., single series or parallel resonance). Additionally, it is known that an increase in bandwidth can be achieved by using a multi-resonant matching circuit and also the reflection coefficient is optimized within the band of interest. The maximum bandwidth using multi-mode techniques is ultimitely bounded by the Bode-Fano limit and is given by

$$B = \frac{1}{Q} \frac{\pi}{\ln\left(1/\Gamma_{max}\right)} \tag{2.16}$$

where B is the 3 dB fractional bandwidth, Γ_{max} is the maximum allowable reflection coefficient in the passband, and Q is the quality factor of the load or antenna.

2.4 Summary

This chapter has focused on giving the reader an overview on small antenna performance characteristics and also to show the progression of research that has formed the foundation for small antenna theory. In Chapter 3, we introduce an insightful analysis method that will be used throughout this document. The method is based on the theory of characteristic modes.

CHAPTER 3

THEORY OF CHARACTERISTIC MODES

A design and analysis tool that provides the user with a great deal of insight into the mode of operation is the theory of characteristic modes (CM). The theory was initially developed by Garbacz and Turpin in the early seventies [25]. The derivation was later altered and refined by Harrington and Mautz [26, 27]. CM was initially used for antenna shape synthesis [28, 29] and also to mitigate antenna scattering by using reactive loading [30].

The characteristic modes of a radiating structure (or conducting body) represent all the real current modes that are possible on a structure given its geometry. It is important to note that the modes are independent of the excitation but rather are entirely related to the conductor shape and size. Consequently, an antenna design would be a two-step process, where the first step would focus on the antenna size and shape. The size would control the resonant frequency while the shape is chosen to define the radiation characteristics of the antenna. Once the correct mode has been identified, the feed position and type is chosen that will excite the desired mode. For electrically small antennas, relatively few modes are required to accurately model it (typically three or four would suffice).

3.1 Formulation of CM

As shown in [31], characteristic modes (also known as characteristic currents) are the eigenfunctions of the following particular weighted eigenvalue equation:

$$X(\overline{J}_n) = \lambda_n R(\overline{J}_n) \tag{3.1}$$

and in matrix form:

$$[X](\overline{J}_n) = \lambda_n[R](\overline{J}_n) \tag{3.2}$$

where λ_n are the eigenvalues, $\overline{J}_n$ are the eigenvectors (or eigencurrents), and R and X are the real and imaginary parts of the impedance operator, respectively, given by

$$Z = R + jX \tag{3.3}$$

The impedance (Z) is obtained from an integro-differential equation. If Z is linear and symmetric, because of the reciprocity theorem, then R and X will also be linear and symmetric. Thus all eigenvalues λ_n are real and all the eigenfunctions, $\overline{J}_n$, can be chosen real or equiphasal (complex constant times a real function) over the conducting surface on which they were defined [26]. The orthogonality properties of characteristic modes stem from the choice for R to be a weighted operator in Equation 3.1. The orthogonality properties are given by,

$$\langle \overline{J}_m^*, R(\overline{J}_n) \rangle = \delta_{mn} \tag{3.4}$$

$$\langle \overline{J}_m^*, X(\overline{J}_n) \rangle = \lambda_n \delta_{mn} \tag{3.5}$$

where δ_{mn} is the Kronecker delta function (0 if $m \neq n$ and 1 if $m = n$).

The electric fields E_n generated by the characteristic surface currents J_n are known as the characteristic fields [26]. The characteristic fields are derived from Equation 3.1 and given as

$$\begin{aligned} E_n(\overline{J}_n) &= Z(\overline{J}_n) \\ &= R(\overline{J}_n) + jX(\overline{J}_n) \\ &= R(\overline{J}_n)(1 + j\lambda_n) \end{aligned} \tag{3.6}$$

Thus from Equation 3.6 we note that E_n is equiphasal, because it is determined from the product between a real valued quantity and the term $(1 + j\lambda_n)$. The orthogonality relationship of characteristic fields can be highlighted using the complex Poynting theorem:

$$
\begin{aligned}
P(J_m, J_n) &= \langle J_m^*, Z J_n \rangle \\
&= \langle J_m^*, R J_n \rangle + j \langle J_m^*, X J_n \rangle \\
&= \oiint_{S'} \overline{E}_m \times \overline{H}_n^* ds + j\omega \iiint_{\tau'} (\mu \overline{H}_m \cdot \overline{H}_n^* - \epsilon \overline{E}_m \cdot \overline{E}_n^*) d\tau \\
&= (1 + j\lambda_n)\delta_{mn}
\end{aligned}
\tag{3.7}
$$

The orthogonality principles of characteristic modes means that they radiate power independently (i.e., there is no coupling between modes). Thus the characteristic currents can be used as a basis set in order to expand the unknown total current (J) on the conducting body surface and can be expressed as

$$
J = \sum_n \frac{V_n^i J_n}{1 + j\lambda_n} \tag{3.8}
$$

The symbol V_n^i in Equation 3.8 is called the modal-excitation coefficient and is given by

$$
V_n^i = \langle J_n, E^i \rangle = \oint_n J_n \cdot E^i ds \tag{3.9}
$$

The modal-excitation coefficient describes how the applied excitation (given its position, magnitude, and phase) controls the contribution of each individual current mode (J_n) to the total current (J). The product, $V_n^i J_n$ represents the coupling between the excitation and the J_n mode, and determines how well a particular mode is excited by the antenna feed or incident field (for scattering applications or indirect feeding applications).

The eigenvalues (λ_n) which correspond to the characteristic modes (J_n) provide useful information for individual modes. The magnitude of the eigenvalue indicates how well the particular mode radiates (the closer to zero the better). The radiating power (real part) for each mode is normalized to unity as given by Equation 3.7. The reactive power, however, is directly proportional to the magnitude of the eigenvalue. Thus, when considering a particular mode with small magnitude eigenvalue, we can say that the mode radiates more power than it stores (i.e., reactive power). Resonant

modes are defined as modes with corresponding eigenvalues equal to zero, $|\lambda_n = 0|$. Also, the eigenvalue's sign indicates what type of energy storage is contributed by the mode. The mode contributes to storing magnetic energy if $\lambda_n > 0$ or electrical energy if $\lambda_n < 0$.

3.2 Analysis Example: Rectangular Patch Antenna

To illustrate the usefulness of CM, an analysis of a conventional rectangular microstrip patch antenna is performed. The goal of this type analysis is to be able to ascertain what modes are possible on this structure for the given band of frequencies of interest. The resonant frequencies that correspond to the modes are determined and also their current distributions. By calculating the eigenvalues it can be determined how each mode contributes to the total current at a specific frequency. This analysis is not concerned with feed selection because we are interested in determining all possible modes and not only those for a specific feed. The dimensions and properties of the rectangular microstrip antenna are shown in Figure 3.1. The ground plane is taken to be infinite in extent.

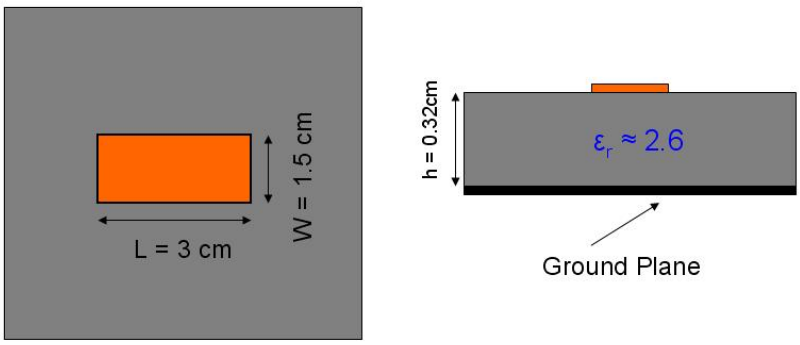

Figure 3.1: Rectangular Patch Antenna Layout

A numerical calculation of this structure is performed in the full wave simulation software FEKO, which is based on the Method of Momemts (MOM) code. FEKO is used to obtain the impedance operator (Z). Then, using Matlab code developed by Dr. J. Adams, the eigenvalues and eigenvectors are calculated by solving the eigenvalue problem (Equation 3.1). Figure 3.2 shows the eigenvalues for the five lowest order modes for the rectangular patch antenna.

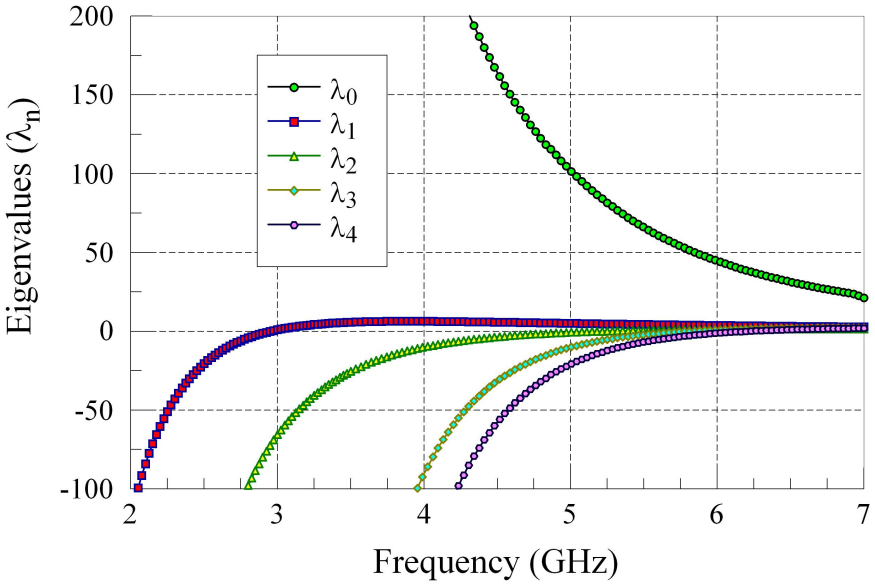

Figure 3.2: Eigenvalues for the Five Lowest Modes on the Rectangular Patch Antenna

Because of the very large values that the eigenvalues can attain, the plot above is zoomed in substantially. All eigenvalues (except λ_0) are negative at low frequencies and then rapidly increase in value until they cross the zero point and eventually settle at a small positive value. The frequency at which $\lambda_n = 0$ is defined as the mode resonance frequency. The zeroth-order eigenvalue is always positive and thus never resonates (i.e., no frequency where $\lambda_0 = 0$). It can be deduced that mode 0 stores magnetic energy since $\lambda_0 > 0$ and that all higher order modes store electric energy below their resonant frequencies.

There are other representations of eigenvalue information of interest. One such representation is Modal Significance (MS) [31]. Modal Significance shows at a glance how significant a particular mode's contribution is to the aggregated response. The modal significance is given by

$$MS = \left| \frac{1}{1+j\lambda_n} \right| \tag{3.10}$$

The MS for the rectangular patch antenna (RPA) is shown in Figure 3.3. The MS for a mode represents the normalized current amplitude for that mode. Thus a MS value of 1 (or peak) equates to mode resonance, while low MS values relate to modes that have weak radiation characteristics. Thus the

MS plot is an alternative representation of the eigenvalue plot (Figure 3.2) where it can be difficult to visualize the zero crossover resonance.

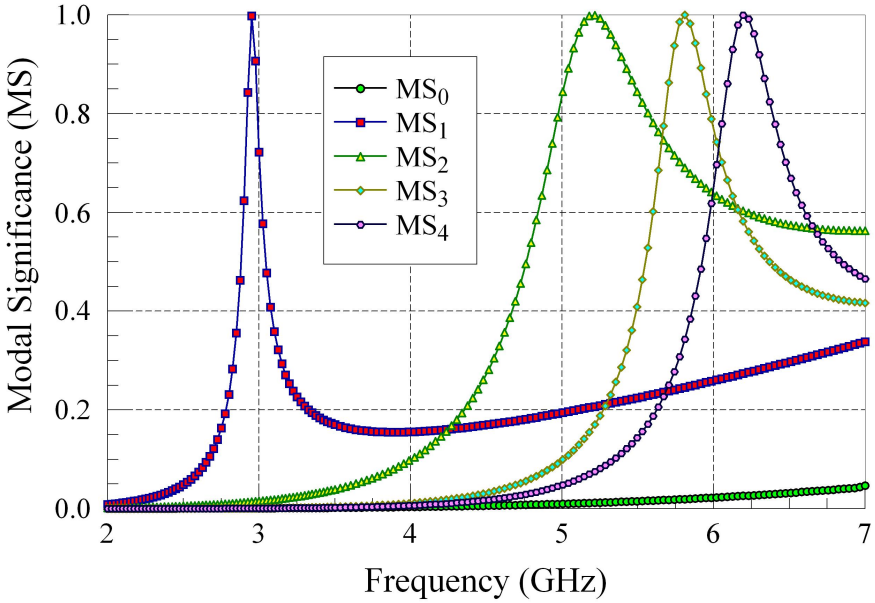

Figure 3.3: Modal Significance for the Five Lowest Modes on the Rectangular Patch Antenna

Another representation of the eigenvalue data is in terms of the characteristic angle (α_n). The characteristic angle represents the phase difference between the characteristic currents (J_n) and the characteristic fields (E_n). The characteristic angle is given by

$$\alpha_n = 180^\circ - \tan^{-1}(\lambda_n) \tag{3.11}$$

Figure 3.4 shows the characteristic angle plots for the five lowest order modes for the rectangular microstrip patch antenna. For this representation the resonant frequency is defined by a characteristic angle, $\alpha_n = 180^\circ$, and represents the frequency where the antenna radiates well. Characteristic angles close to 90° or 270° are associated with energy storage. Additionally, the slope of the characteristic angle curve around the resonance ($\alpha_n = 180^\circ$) gives information about the width of the radiation bandwidth. A gradual slope represents a wide bandwidth and a steep slope indicates a narrow bandwidth. Based on small antenna theory, as the antenna is electrically smaller we expect the radiation bandwidth to be narrower and from Figure 3.4 we do indeed see this phenomenon. The characteristic angle plot for mode 1 has

a steeper slope than higher modes, indicating the radiating bandwidth for mode 1 is narrower than higher order modes.

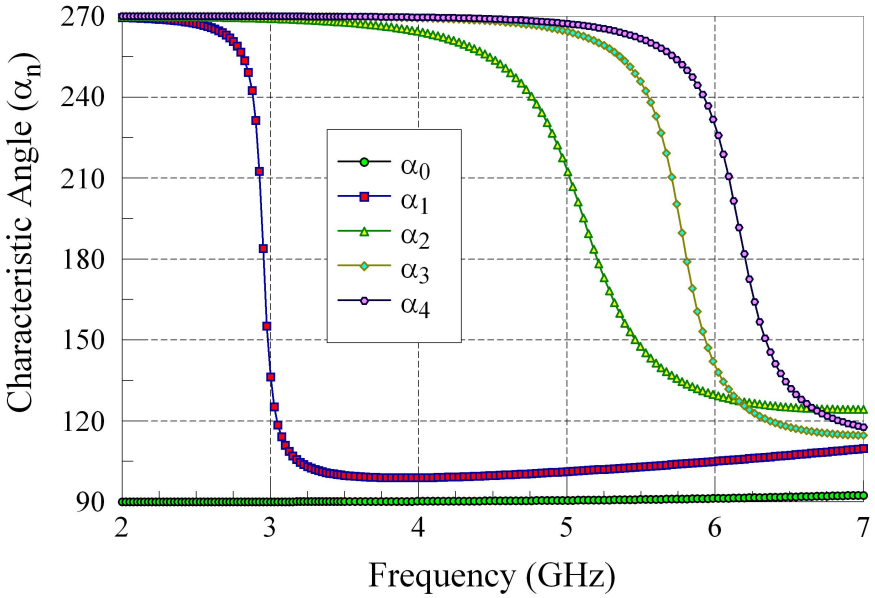

Figure 3.4: Characteristic Angle for the Five Lowest Modes on the Rectangular Patch Antenna

In order to visualize the current distributions for the individual modes, the calculated characteristic currents are returned into the FEKO software environment. Figure 3.5 shows the current distributions for mode 0 and mode 1.

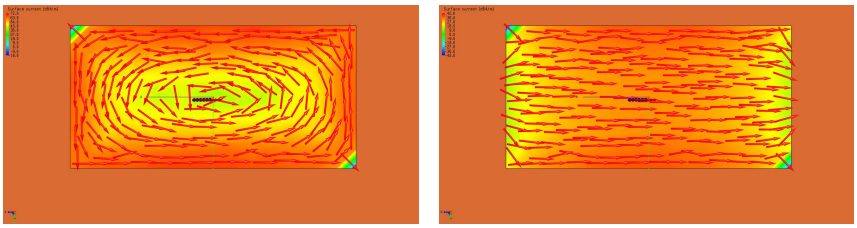

(a) Mode 0 (b) Mode 1 (2.95 GHz)

Figure 3.5: Current Distributions of the RPA for Modes 0 and 1

Mode 0 is a non-radiating mode, thus the current distribution shown in Figure 3.5(a) displays this phenomenon since the currents do not terminate but instead circulate. The current distribution for mode 1 (resonant frequency, $f_r \approx 2.95$ GHz) is the conventional radiating mode for a rectangular-shaped

patch, referred to as the TM_{10} mode. Figure 3.6 displays the current distributions for modes 2, 3 and 4.

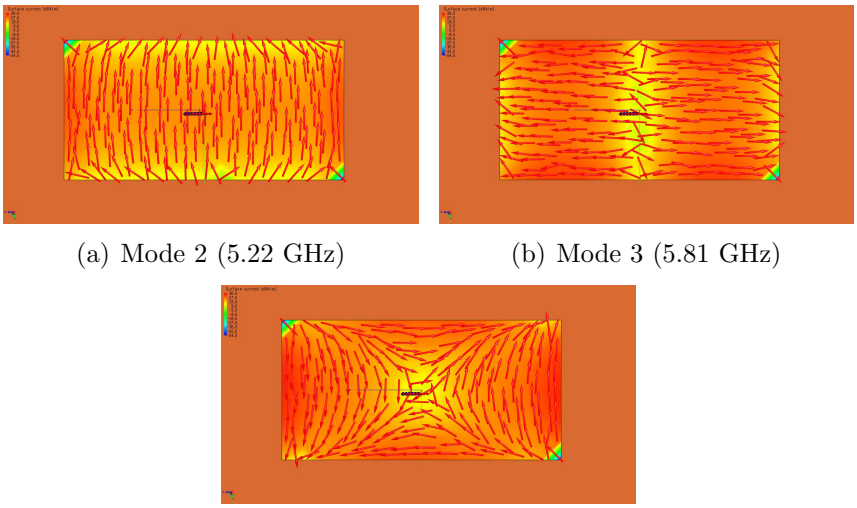

(a) Mode 2 (5.22 GHz)

(b) Mode 3 (5.81 GHz)

(c) Mode 4 (6.2 GHz)

Figure 3.6: Current Distributions of the RPA for Modes 2, 3 and 4

Mode 2 ($f_r \approx 5.22$ GHz) corresponds to the frequency at which the vertical dimension is a resonant length ($\approx \lambda_g/2$). Mode 2 is called the TM_{01} mode. Mode 3 ($f_r \approx 5.81$ GHz) corresponds to a horizontal electrical length of approximately 1λ (the current distribution of a full wavelength resonance has a null at the center with currents either side of null pointed in opposite directions as shown in Figure 3.6(b)). Mode 3 is logically termed the TM_{20} mode since its the full wavelength distribution in the horizontal dimension. Modes 4 and above are the higher order modes supported by the patch. Generally, an antenna engineer's goal is to design a patch antenna at mode 1 since this is its most efficient operating point. As the frequency of operation increases more modes contribute to the radiated power and consequently polarization purity is compromised, resulting in increased cross polarization.

A simple method to miniaturize this type of antenna is to meander the patch. The meandering is accomplished by cutting slots in the patch along the non-radiating edges. Figure 3.7 shows the layout for a typical meandered rectangular patch antenna (MRPA) (highlighting a zoomed in view of the slots with their dimensions). The slots that are removed from the patch are

0.2 cm x 0.75 cm in size, thus achieving a 50% meander (i.e., the slot depth is 1/2 the patch width).

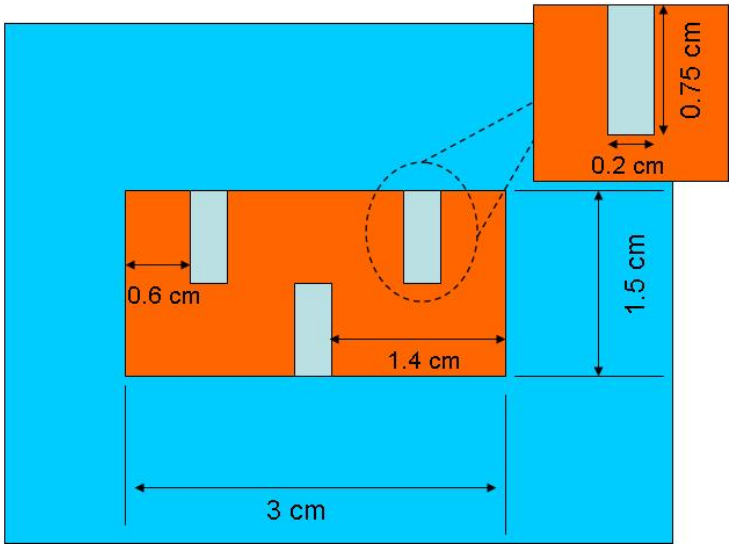

Figure 3.7: Meandered Rectangular Patch Antenna Layout

The characteristic angles for the first three modes (ignoring the non-radiating mode) are plotted in Figure 3.8.

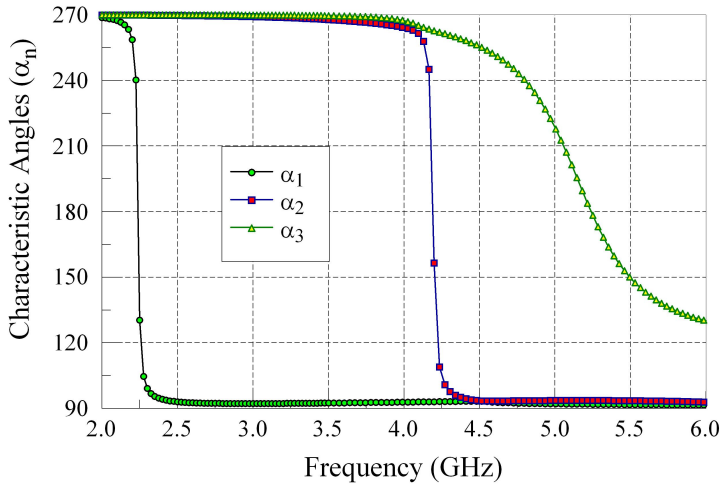

Figure 3.8: Characteristic Angles for Three Lowest Modes

Comparing Figures 3.4 and 3.8 it is observed that the modes derived from the horizontal dimension resonance (mode 1 and 3) are now resonating at substantially lower frequencies. Thus, the fundamental TM_{10} and TM_{20} mode resonant frequencies have been lowered and the antenna has been miniaturized. As a figure of merit, we can define a miniaturization factor (MF) [5]

as

$$MF = \frac{f_{ref}^{original}}{f_{ref}^{miniaturized}} \tag{3.12}$$

The higher the degree of miniaturization, the larger MF value, while no or little miniaturization is indicated when $MF \simeq 1$. The resonant frequencies of both the RPA and MRPA as well as the miniaturization factors are presented in Table 3.1.

Table 3.1: RPA and MRPA Mode Comparisons

Mode #	RPA (GHz)	MRPA (GHz)	MF
1	2.925	2.25	1.30
2	5.25	5.25	1
3	5.81	4.2	1.38

The current distributions for the MRPA (Figure 3.9) show that the TM_{20} mode for RPA has been lowered to below the static TM_{01} which is essentially unaffected by meandering the patch antenna, thus modes 2 and 3 have reversed orders for the MRPA configuration.

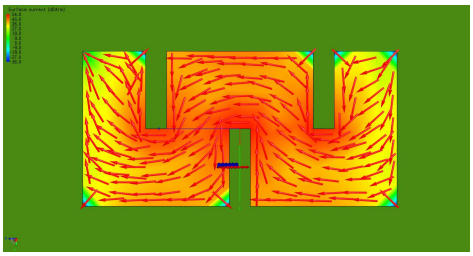

(a) Mode 1 (2.25 GHz)

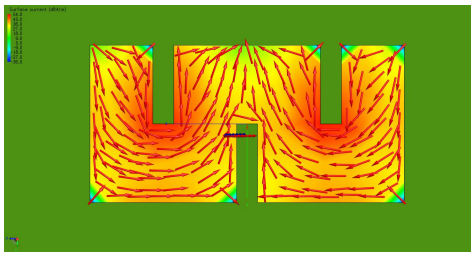

(b) Mode 2 (4.2 GHz)

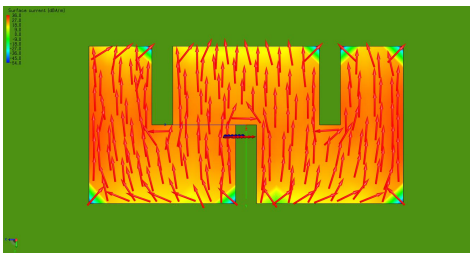

(c) Mode 3 (5.25 GHz)

Figure 3.9: Current Distributions of the MRPA for Modes 1, 2 and 3

By examining the current distribution for the fundamental radiating mode (mode 1), it is clear the miniaturization is achieved by effectively lengthening the current path, thus lowering lowering the resonant frequency. A consequence of meandering the radiating patch is an increased level of cross polarization of the radiated field (something to be aware of when using in polarization sensitive applications).

3.3 Summary

The theory of characteristic modes has been presented and its usefulness was illustrated by means of relevant examples. This method of analysis is extremely effective in simplifying complex radiating problems, thus allowing for insightful conclusions on operation and practical deductions on design guidelines. In Chapter 4 we analyze an antenna structure which has been reported to be a metamaterial antenna, called the "Infinite Wavelength Resonant Antenna (IWRA)." This antenna is claimed to have size independent properties, this would be very desirable, and we will evaluate these claims and generally develop a theory of operation for the IWRA.

CHAPTER 4

ANALYSIS OF THE INFINITE WAVELENGTH RESONANT ANTENNA

Recently, an antenna having both metamaterial characteristics and miniaturization capabilities was reported, and is known as a "Infinite Wavelength Resonant Antenna" or simply IWRA [32]. Claims about the IWRA miniaturization are a bit outlandish and in fact violate the fundamental limits established by Wheeler and Chu [2, 9]. Needless to say, a fair amount of speculation and debate over the validity of the theory on which metamaterials is based, exists in the electromagnetics community. Scepticism over the actual operation and performance obtained is also prevalent. So much so, that Munk [33] published a book where he criticizes metamaterial theory and offers alternative explanations for their characteristic behavior. The analysis conducted in this chapter ignores metamaterial theory and strictly applies traditional analysis methods in order to determine the theory of operation and the source of miniaturization.

Even though this structure will not be considered as a metamaterial antenna, the metamaterial theory is presented in the next section. This is done so that the reader can gain perspective into work conducted by other researchers on the IWRA.

4.1 Negative Refractive Index (NRI) Metamaterials

Veselago [34] performed an analysis on media having negative permittivity (ϵ) and permeability (μ). His conclusion that a material with simultaneous negative permittivity and permeability would result in a negative index of refraction ($n = -\sqrt{\mu\epsilon}$) has numerous implications when considering its application to Maxwell's equations. For instance, the electric ($\mathbf{E}$) field, magnetic ($\mathbf{H}$) field, and the wavevector ($\mathbf{k}$) for plane waves form a "left-handed" triad.

This indicates that the group ($\mathbf{v}_g$) and phase ($\mathbf{v}_p$) velocities have opposite directions. This is another way of saying that this media would support backward wave propagation but forward energy flow.

There are no materials in nature that possess negative permittivity and permeability. Thus, there exist methods for "artificially" producing an effective material (using periodic structures) where they exhibit the left-handed (LH) behavior in a finite frequency band. True interest in this area was sparked by experimental evidence of the LH behavior (the results are disputed by Munk [33]). Two sets of experiments are well cited, in the first the material was produced using a periodic arrangements of split ring resonators (SRRs) and the second, a periodic array of metallic thin wires was utilized to create a metamaterial at certain microwave frequencies [35, 36]. It is also common to realize this media by employing periodic reactively-loaded transmission line (TL) grids [37]. The TL-based materials have been shown to possess wider bandwidths than resonator-based NRI materials and also they can readily be manufactured using standard microstrip fabrication methods [5]. It is for this reason that the NRI-TLs are extensively used in printed antenna and radio frequency (RF) applications [38].

The circuit model for a standard lossless TL is a periodic structure where the smallest element that is repeated is termed the "unit cell." The unit cell is given by a series inductor (L_R) and a shunt capacitor (C_R), where subscript R specifies that these components are derived from RH behavior. For the NRI-TL model the components are swapped, so the model comprises of a series capacitor (C_L) and a shunt inductor (L_L), where the subscript L refers to components derived from the LH behavior. As mentioned before, there is no pure NRI media in nature and we have to introduce the LH phenomena in an host material which has conventional RH behavior. Thus, we never eradicate this RH behavior completely and so all practical NRI-TLs will be able to support both LH and RH propagation. The resulting medium is referred to as "composite right left handed" (CRLH) transmission line [39]. Figure 4.1 shows the circuit model for the CRLH TL unit cell.

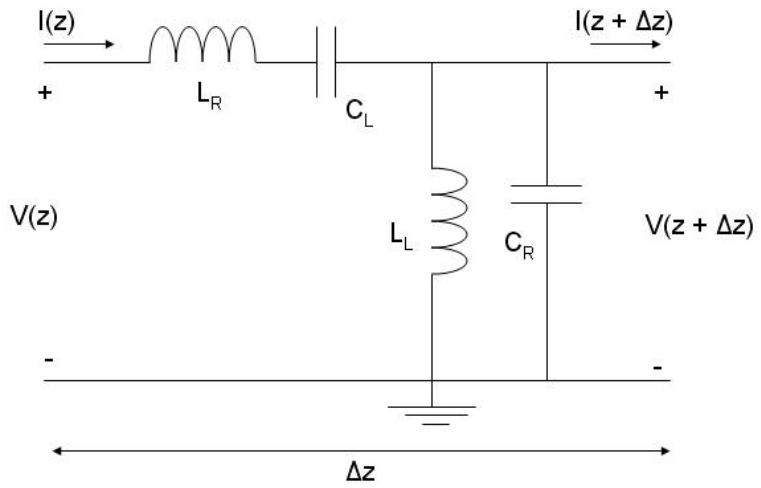

Figure 4.1: Circuit Model for the CRLH TL Unit Cell

4.2 Realization of the IWRA

The name coined to this antenna is hard to interpret: what does infinite wavelength mean practically? The name is derived from a phenomenon in the CRLH TL, known as zeroth-order resonance. The unit cell (Figure 4.1) supports a condition where the propagation constant is zero for a nonzero frequency (i.e., zeroth-order resonance). Zero propagation constant for nonzero frequency implies infinite wavelength, due to the inverse relationship. Since the resonant modes of an antenna are defined where a dimension (e.g., patch length) is a function of the propagation constant ($\beta_m l = m\pi$). Metamaterial believers argue that this phenomenon ($\beta = 0$ while $\omega \neq 0$) allows the IWRA to operate as a resonant antenna independent of its electrical size. This is in conflict with fundamental small antenna theory, effectively saying that electrically small antennas can easily be attained since the physical size of the structures can be arbitrarily chosen. Tuning of the resonant frequency is obtained by varying the effective components in the unit cell model (Figure 4.1).

An existing transmission line radiating structure (like microstrip planar antennas) has to be augmented to introduce left-handed components. These can theoretically be implemented with either lumped or distributed structures though lumped components would be impractical due to their incapability to radiate well. A popular choice of microstrip-type implementation of the CRLH TL is by using the so-called "Sievenpiper Mushroom" (SM) struc-

tures [40]. The mushroom structures comprise of a square metallic patch which is shorted to a ground plane with a via (or shorting post). Figure 4.2 shows pictorially how SMs when arranged in a periodic fashion adequately represents the CRLH TL.

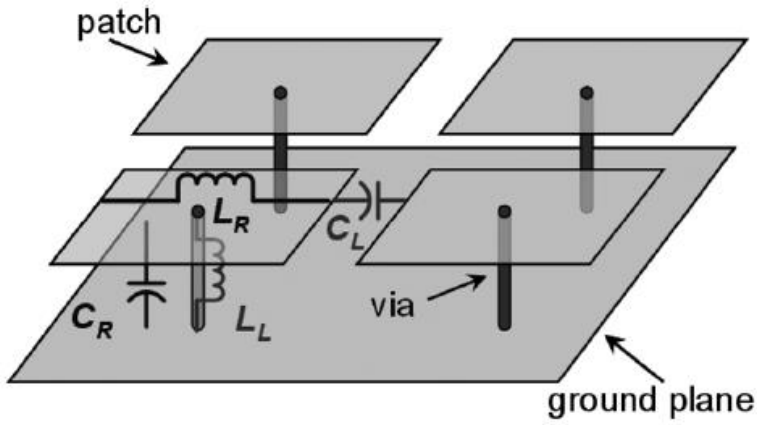

Figure 4.2: Realization of the CRLH TL Using Sievenpiper Mushrooms (SMs) [32]

It is shown that RH components are derived from the patch structure, the series inductor (L_R) is due to the self inductance of the patch and the shunt capacitor (C_R) stems from the parallel plate effects between the patch and the ground plane. The LH components result from introduction of the shorting post which gives rise to the shunt inductor (L_L) and a series capacitor (C_L) due to coupling between adjacent SM structures. Thus by altering the physical dimensions (or properties) of the SM structure the equivalent components in the CRLH TL models can be tuned.

4.3 Traditional Analysis of the IWRA

As mentioned in Section 4.2, the IWRA is said to be able to operate independent of its electrical size. These claims are counter to traditional small antenna theory presented by Wheeler [2] and Chu [9] who investigated the relationship between electrical size and bandwidth. Given the attributes for this antenna, it would be extremely useful to develop a theory of operation so

that it can be understood and used in an optimized manner. The IWRA was developed by Lai et al. [32]. The IWRA is shown in Figure 4.3. The IWRA has a relatively simple geometry (composed of rectangular patch elements). This makes modeling with transmission line models easier because they are well defined for rectangular shaped lines.

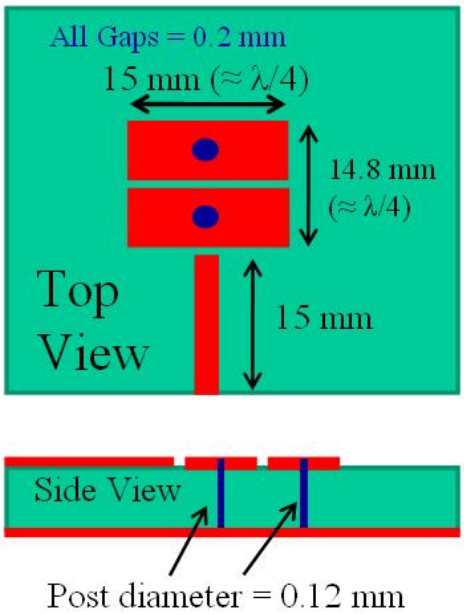

Figure 4.3: Two Unit Cell IWRA Physical Layout with Dimensions

The IWRA is essentially a reactively loaded microstrip patch antenna. It is fed by a proximity-coupled microstrip line with a characteristic impedance of 50 Ω. The radiating patch element has an air gap at its center that divides it into two smaller patches. These smaller patches have shorting posts at their geometric centers. This antenna is said to be a two cell version of the IWRA where the unit cell is a Sievenpiper mushroom (SM) structure [40]. The air gap provides a series capacitor and the shorting post appears as a shunt inductor element. By effectively including these reactive components, the resonant frequency can be reduced substantially, thus achieving antenna miniaturization of roughly 50% over the conventional microstrip patch antenna. The input S_{11} magnitude plot for the IWRA is shown in Figure 4.4. Note all full wave simulations are performed in Ansoft HFSS. Circuit simulations are conducted in Agilent's ADS.

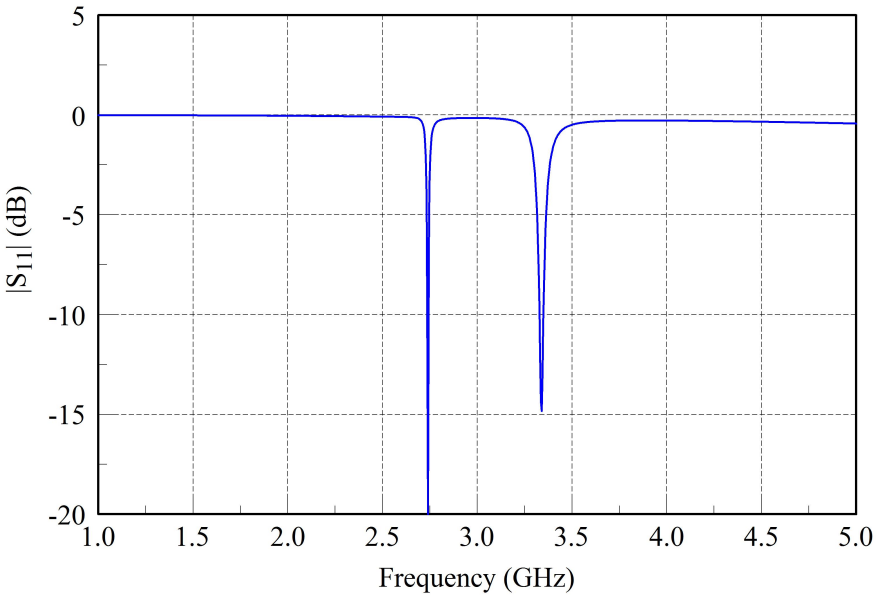

Figure 4.4: IWRA Reflection Coefficient ($|S_{11}|$) vs. Frequency

The reflection coefficient plot shows that there are two closely spaced modes (low reflection coefficient). These modes correspond to distinct field distributions on the antenna, as shown in Figure 4.5. At the lower resonance, the field distribution on the mushroom structures have odd symmetry. While at the upper resonant frequency the field distribution on the mushroom structures have even symmetry.

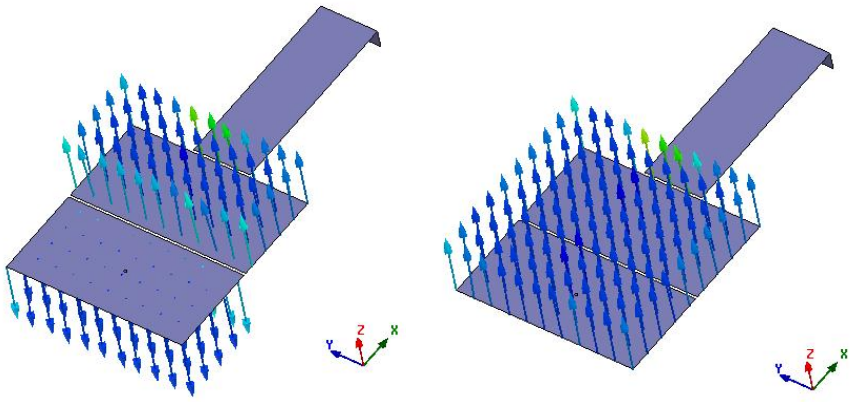

(a) Lower Frequency Mode (b) Upper Frequency Mode

Figure 4.5: IWRA E-field Distributions at the Lower and Upper Resonances

The IWRA has been researched by many groups with interest in leveraging its dual-frequency operation [41] or implementing techniques to increase its narrow bandwidth [42]. The use of reactive loading can also be used as an agent for frequency or pattern reconfigurability [43]. In summary, the IWRA's main advantage is that it achieves a degree of antenna miniaturization, supports multi-frequency operation, and has the potential for reconfigurability. Disadvantages include narrow bandwidth and lack of clear design methodology. The goal for this chapter is to develop the understanding of operation for this antenna that will lay the foundation for a clearly defined design guide that goes beyond the metamaterial analysis.

4.3.1 Circuit Modeling

Transmission line theory is well-established tool for developing insightful understanding for transmission line structures, like rectangular microstrip patch type structures. This antenna is similar in geometry to a conventional patch antenna but with strategically placed discontinuities. These discontinuities manifest themselves as reactive components. This is valid as long as the discontinuities are physically small relative to the operating wavelength. An approximate circuit model for the antenna can be developed by cascading transmission line models and discontinuity models in the correct order. Accurate transmission line models exist for the rectangular microstrip lines [44]. While closed-form expressions exist for some discontinuities, the components that make up the individual components will be extracted using full wave simulations.

For this particular radiating structure, we are interested in three microstrip discontinuities. These discontinuities are the gap between the two patch elements, the metallic posts that is connected between the patch elements to the ground plane and the open ends at the radiating patch edges. A microstrip transmission line (MTL) gap discontinuity can be modeled as a symmetrical pi-network, where the elements of the network are capacitive components. This can easily be explained when considering there is always a capacitive effect when two conductors are relatively close together and there exists a potential (or charge) difference between the conductors (e.g., parallel plate

capacitor). Given this phenomenon, it is reasonable to assume that the value of the series component of the pi-network is strongly dependent on the gap width while the shunt component values are strongly linked to the characteristics of the microstrip line itself (i.e., line width, line height above ground plane, etc.).

Since the metallic post is a physically short and thin wire, it appears as a single inductor (if losses are small) at RF frequencies. Finally, the open end of the microstrip radiator can be modeled as a rectangular slot. An accurate set of expressions for the slot impedance can be found in [44].

4.3.2 Component Extraction

The individual components that make up these discontinuities can be determined using network theory. A simple simulation experiment is carried out in order to extract the network parameters required to determine the component values of a given discontinuity. The experiment is conducted in a full wave electromagnetic solver (Ansoft HFSS) and its physical arrangement is shown in Figure 4.6.

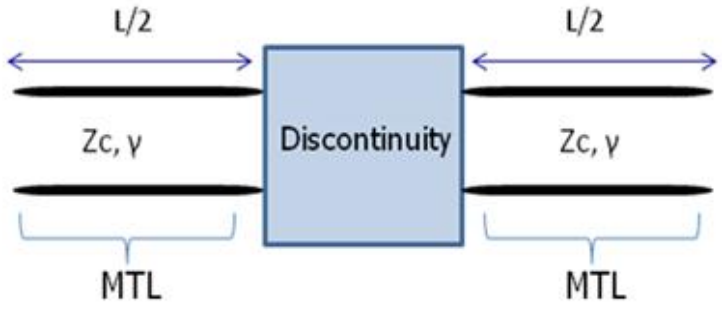

Figure 4.6: Test Circuit Configuration

The extraction of the discontinuity parameters involves a two-stage process. First, the circuit above is simulated without any discontinuity (i.e., just the microstrip transmission line), this allows for the determination of the line parameters Z_c (characteristic impedance) and γ (complex propagation constant). For the second stage, the discontinuity is inserted at the midpoint

of the line. From network theory, a two-port network formed by a cascade of sub-networks can be accurately described by an ABCD matrix that is obtained by multiplying the individual ABCD matrices of the sub-networks. Equation 4.1 describes this relation for the test circuit and is given by

$$ABCD_{TC} = ABCD_{MTL} * ABCD_x * ABCD_{MTL} \tag{4.1}$$

where $ABCD_{TC}$ = ABCD matrix for the entire test circuit, $ABCD_{MTL}$ = ABCD matrix for the MTL section and $ABCD_x$ = ABCD matrix for the network section that describes the discontinuity under test. The ABCD matrix for a microstrip line [45] is given by

$$ABCD_{MTL} = \begin{bmatrix} \cosh(\gamma L/2) & Z_c \sinh(\gamma L/2) \\ 1/Z_c \sinh(\gamma L/2) & \cosh(\gamma L/2) \end{bmatrix} \tag{4.2}$$

Given that the line parameters are extracted accurately in stage 1, the discontinuity parameters can be backed out using Equation 4.1 because it is the only unknown. If the ABCD matrix for the discontinuity is represented as

$$ABCD_x = \begin{bmatrix} A_x & B_x \\ C_x & D_x \end{bmatrix} \tag{4.3}$$

then individual terms of this matrix are given by,

$$A_x = \frac{1}{2}[A_t(\cosh(\gamma L)+1) - \frac{B_t}{Z_c}\sinh(\gamma L) - C_t Z_c \sinh(\gamma L) + D_t(\cosh(\gamma L)-1)] \tag{4.4}$$

$$B_x = \frac{1}{2}[-A_t Z_c \sinh(\gamma L) + B_t(\cosh(\gamma L)+1) + C_t(Z_c)^2(\cosh(\gamma L)-1) - \frac{D_t}{Z_c}\sinh(\gamma L)] \tag{4.5}$$

$$C_x = \frac{1}{2}[-\frac{A_t}{Z_c}\sinh(\gamma L) + \frac{B_t}{(Z_c)^2}(\cosh(\gamma L)-1) + C_t(\cosh(\gamma L)+1) - \frac{D_t}{Z_c}\sinh(\gamma L)] \tag{4.6}$$

$$D_x = \frac{1}{2}[A_t(\cosh(\gamma L) - 1) - \frac{B_t}{Z_c}\sinh(\gamma L) - C_t Z_c \sinh(\gamma L) + D_t(\cosh(\gamma L) + 1)] \tag{4.7}$$

where A_t, B_t, C_t, and D_t are the ABCD parameters for the test circuit in Figure 4.6 while Z_c and γ are the line parameters. Using Equations 4.4 to 4.7 it is possible to fit the circuit model to the extracted parameters. The shorting post can be modeled as a shunt inductor. Figure 4.7 shows the circuit model for a shunt component along with the corresponding ABCD matrix elements.

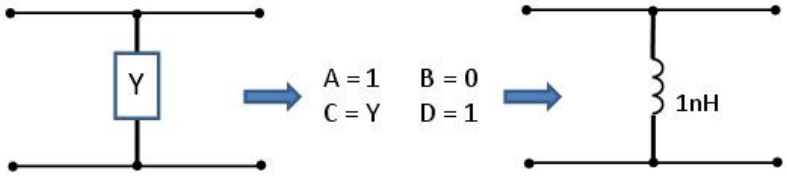

Figure 4.7: Shunt Circuit and Corresponding ABCD Elements

Thus the extracted parameter, C_x, is equivalent to the admittance of the shorting post discontinuity. Applying this methodology, a shorting post with length equal to 1.57 mm and diameter equal to 0.24 mm is equivalent to a 1 nH inductor. The full wave simulation (Ansoft HFSS) of the microstrip line with shorting post is compared to the microstrip line with a 1 nH inductor lumped component (using Agilent ADS software). The comparison shown in Figures 4.8(a) and 4.8(b) confirms that the component extraction for the shorting post is accurate. Note it is sufficient to compare the S_{11} and S_{21} parameters of the S-matrix since this is a symmetrical reciprocal network (i.e., $S_{11} = S_{22}$ and $S_{21} = S_{12}$).

A gap in the microstrip line can in general be modeled as a symmetrical pi-network where each element is capacitive. Figure 4.9 shows the circuit model for a pi-network along with the corresponding ABCD matrix elements.

From the ABCD relations shown in Figure 4.9, the B element of the matrix can be used to determine the series component and either A or D can

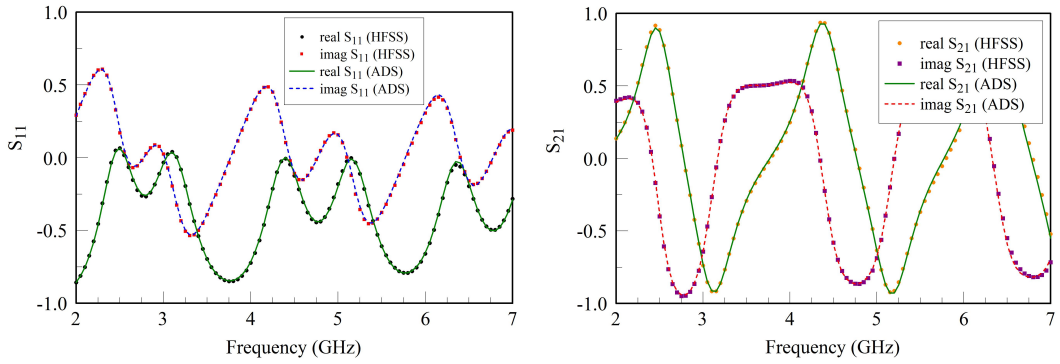

(a) S_{11} (b) S_{21}

Figure 4.8: Comparison of HFSS and ADS Simulations for the Shorting Post

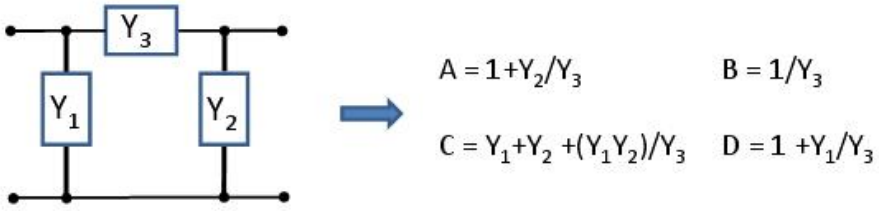

Figure 4.9: Pi-Network and Corresponding ABCD Elements

be used to determine the shunt components since $Y_1 = Y_2$ for symmetrical structures. Figure 4.10 shows the extracted pi-network that represents a 0.2 mm gap in a 15 mm wide microstrip line.

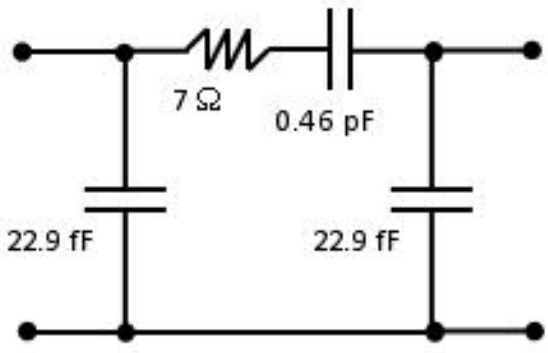

Figure 4.10: Extracted Component Values for the 0.2 mm Gap Discontinuity

The series component (Y_3) is described by a 7 Ω resistor in series with a 0.46 pF capacitor. Because the gap is very small (0.002λ) the loss (7 Ω resistor) across the gap is small and the coupling (0.46 pF $\leftrightarrow$ reactance $\approx$ 115 Ω $\ll$ reactance from shunt) is strong. The shunt component is represented by a 22.9 fF (reactance $\approx$ 2.3 kΩ). The gap discontinuity can be simplified by the single coupling capacitor series component. Figures 4.11(a) (S_{11}) and 4.11(b) (S_{21}) show the comparison of the physical gap simulation (Ansoft HFSS) with a circuit simulation (Agilent ADS) which includes the pi model.

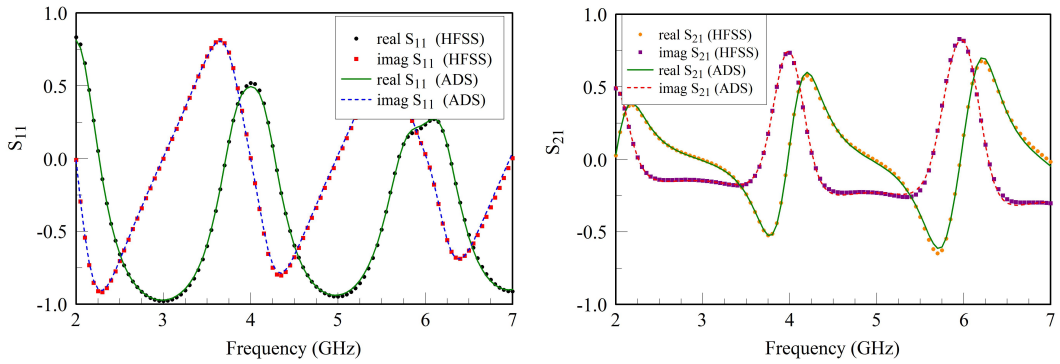

(a) S_{11} (b) S_{21}

Figure 4.11: Comparison of HFSS and ADS Simulations for the Microstrip Gap

4.3.3 Formation of the Antenna Circuit Model

Having developed a circuit model for all the discontinuities that exist in the antenna structure, it is now possible to construct a circuit model for the antenna, one that would mimic the resonant behavior and enable the careful study of the antenna operation. The microstrip patch with a shorting post is also known as a "Sievenpiper mushroom" (SM) structure [40]. The antenna radiating structure (excluding the proximity-coupled feed) can be seen as two SM structures separated by a gap. To account for radiation, the slot load is terminated to the radiating edges of the SM structure. Figure 4.12 highlights the antenna section with reference input plane (port). Note that the reference plane is indicated by a dashed line.

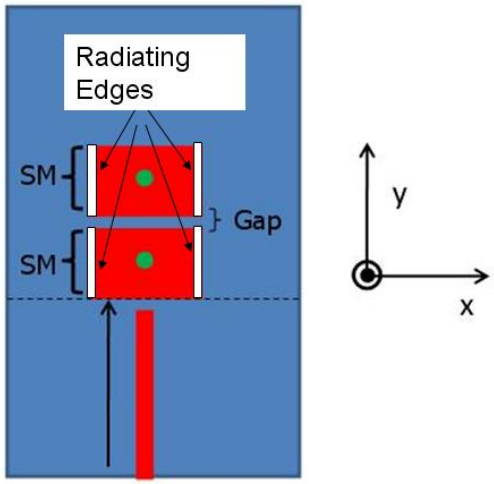

Figure 4.12: Antenna Layout Highlighting the Input Reference Plane (Dashed Line)

Because the patch element is much wider than it is long, the lowest order mode appears along the x direction. The width dimension for the patch is roughly a $\lambda/4$ at the upper resonance and thus the terminating slot loads are placed at the patch edges along the x direction (Figure 4.12). In the circuit model (Figure 4.13), the microstrip line (ML) is line section along the x direction from the edge to the shorting post, so it has a length equal to 7.5 mm and a width equal to 7.3 mm. Also, the slot load (SL) takes on the impedance that a uniformly excited slot with width equal to 7.3 mm and height equal to 1.57 mm. Note the shaded regions represent the sub-circuit model for the SM structure with the slot loads. The input impedance for the circuit model plot is shown in Figure 4.14.

The input impedance of the circuit model shows the existence of two parallel resonances or modes. These two modes correspond to the even and odd symmetry electric field distributions, shown earlier in Figure 4.5. This model does not include the proximity-coupled (gap) feed since it does not alter the performance of the radiating structure in any significant manner. The introduction of the gap feed simply provides impedance scaling and a small frequency shift in the resonances.

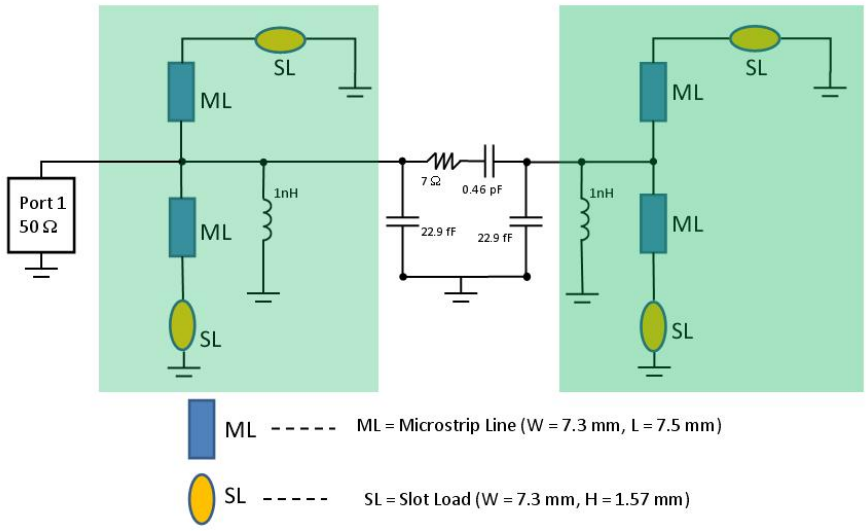

Figure 4.13: Circuit Model for the Reactively Loaded Microstrip Patch Radiator

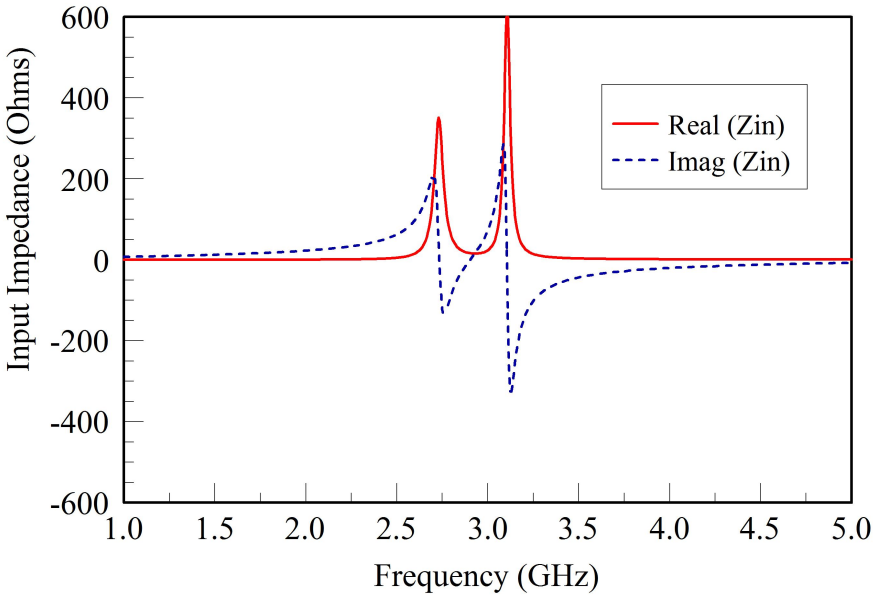

Figure 4.14: Input Impedance Plot for Circuit Model (Figure 4.13)

4.4 IWRA: Theory of Operation

An antenna structure that is composed of two resonant structures that are tightly coupled via a narrow gap is geometrically similar to traditional coupled transmission lines. When conductors are in close proximity with each other, energy will be coupled between them. The coupling mechanism between the conductors can be described by a pi-network (similar to the gap

model for microstrip lines) consisting of capacitors. Figure 4.15 shows the typical arrangement of two coupled lines over a common ground and also displays the model that describes the coupling dynamics.

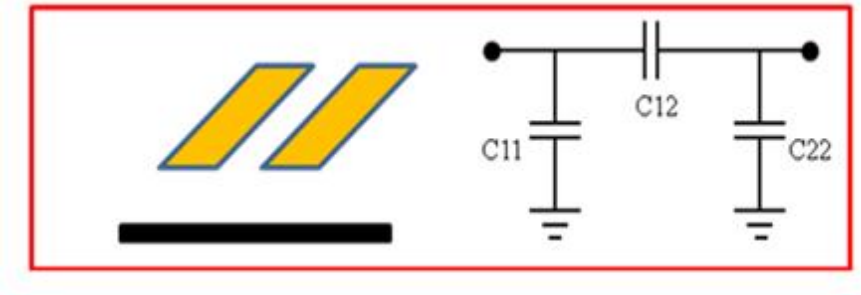

Figure 4.15: Coupled Transmission Lines

Coupled transmission lines support two distinct propagating modes, an even and odd mode. The even mode is characterized by even symmetry across the transmission lines (i.e., the currents flow in the same direction and the voltage potentials from each line to ground are equivalent) as shown in Figure 4.16. The series capacitor C_{12} is removed from the coupled line mode for the even mode case. This means that for the even mode the lines are essentially decoupled.

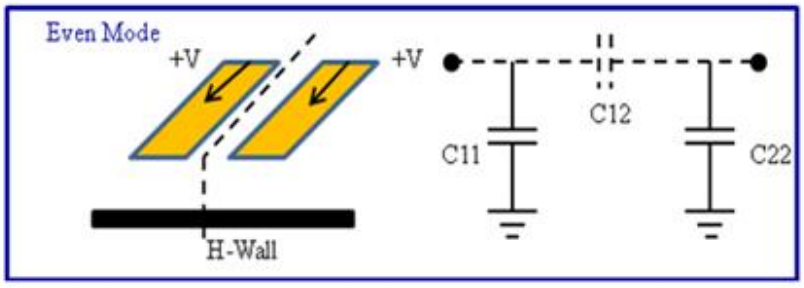

Figure 4.16: Even Mode for Coupled Transmission Lines

The coupled line odd mode is one where an odd symmetry is observed across the lines (i.e., the currents flow in opposite directions and the voltage potentials on the two lines oppose one another) as shown in Figure 4.17. Figure 4.17 also shows the modified couple line model for the odd mode.

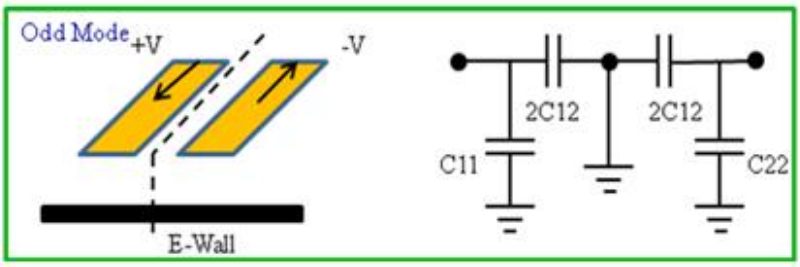

Figure 4.17: Odd Mode for Coupled Transmission Lines

Figure 4.18 shows the simulated surface currents on the antenna structure for the upper (Figure 4.18(a)) and the lower (Figure 4.18(b)) frequency modes. It is clear that upper mode has even symmetry in the current distribution while the lower mode has odd symmetry. Thus the hypothesis that this antenna operates on the same mechanism as coupled lines holds true.

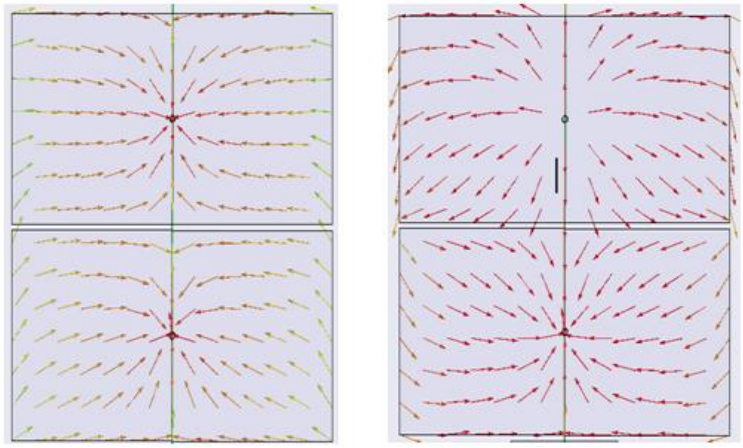

(a) Even Mode (b) Odd Mode

Figure 4.18: Simulated Surface Current Distributions on the SM Structures

By decomposing the modes, the design methodology is greatly simplified. The decomposition of these modes can be confirmed by applying the relevant gap models that correspond to the specific mode in question. For the even mode, the SM structures are effectively decoupled so this mode essentially corresponds to the input impedance of a single SM structure as shown in Figure 4.19.

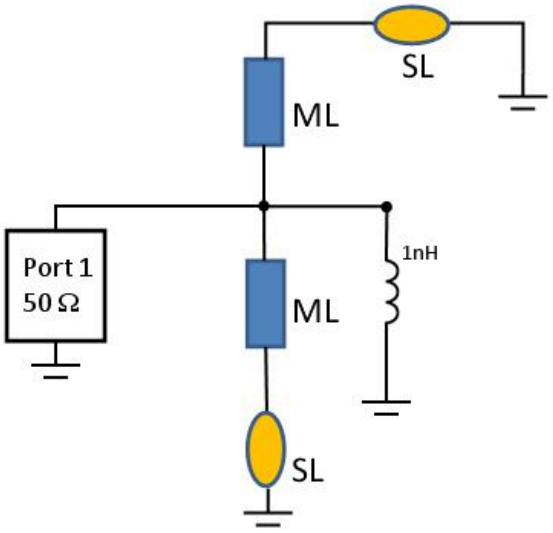

Figure 4.19: Even Mode Circuit Model

The input impedance response for the even mode circuit model has a single mode that appears exactly at the upper resonance for the complete circuit model as shown in Figures 4.20(a) and 4.20(b). Thus the resonance of the upper mode corresponds to the parallel resonance of the SM structure.

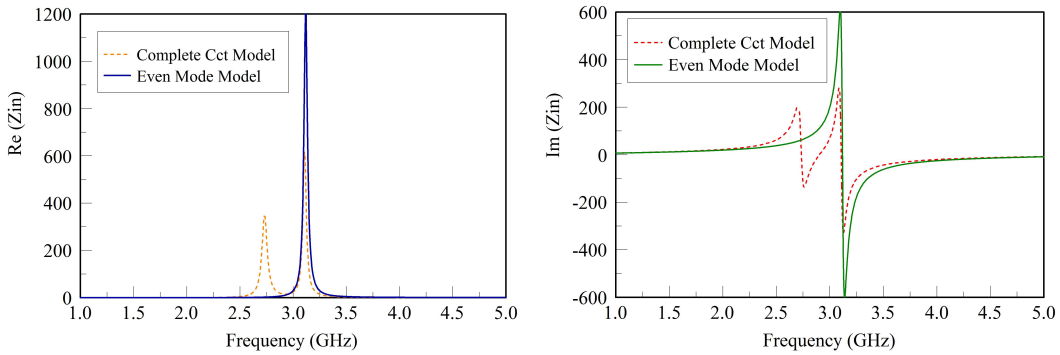

(a) Real Part

(b) Imaginary Part

Figure 4.20: Input Impedance Comparison between Even Mode and Complete Circuit Model

The odd mode circuit model is simply the complete circuit model with the gap model replaced with the odd mode coupled line model (Figure 4.17). The odd mode circuit model is shown in Figure 4.21. For this topology, the

SM structures are tightly coupled.

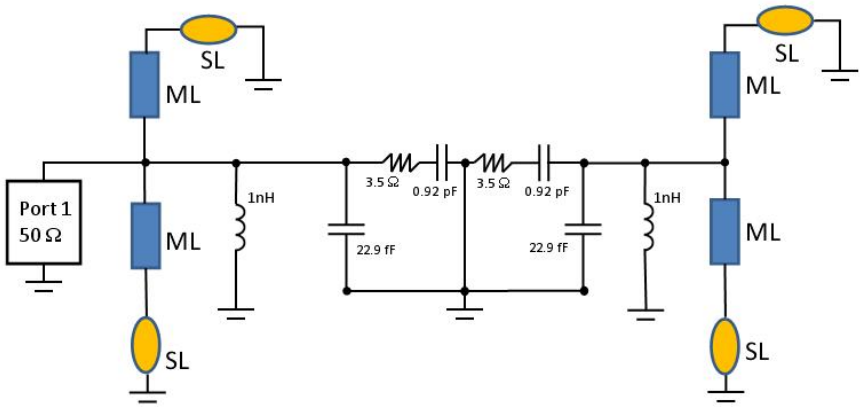

Figure 4.21: Odd Mode Circuit Model

The odd mode circuit model impedance response is compared to the complete circuit response in order to confirm the thesis that the odd mode circuit correctly describes the lower mode. Figures 4.22(a) and 4.22(b) show the comparison of the odd mode circuit and complete circuit impedance responses.

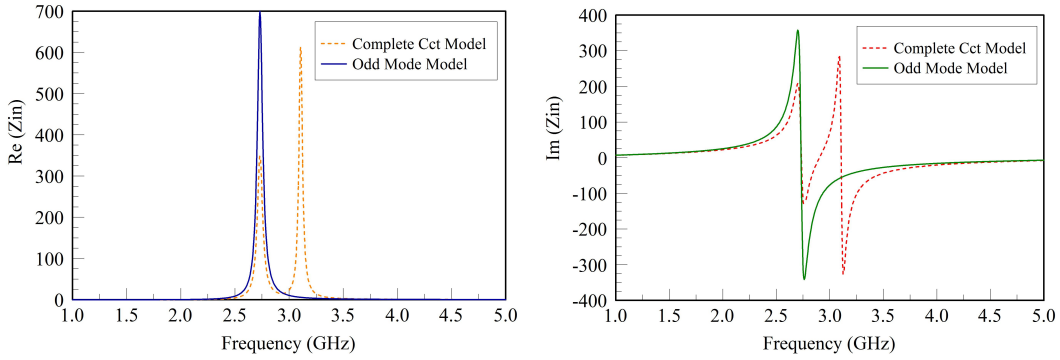

(a) Real Part (b) Imaginary Part

Figure 4.22: Input Impedance Comparison between Odd Mode and Complete Circuit Model

4.5 Design Guidelines

The source of the resonances has been identified and as such the design of this antenna can be greatly simplified compared to metamaterial approaches. The source of the even mode is a parallel resonance in the Sievenpiper mushroom structure. The resonating elements are the shunt inductance of the shorting post and the capacitance presented by the patch (forming a parallel plate with the ground plane). The resonant frequency for the SM structure can be expressed as

$$f_r = \frac{1}{2\pi\sqrt{L_{Post}C_{Patch}}} \tag{4.8}$$

where $L_{Post}(d_{Post},h_{Sub})$ and $C_{Patch}(A_{Patch},h_{Sub})$.

The post inductance is a function of the post diameter and its length (effectively, the substrate height). The patch capacitance is a function of the patch area and the substrate height as well as the substrate permittivity. Miniaturization of this antenna by establishing a lower operating frequency is a key attribute of this topology and leveraging this property is of interest. To lower the operating frequency, either the post inductance or patch capacitance can be increased. The inductance of the shorting post is inversely proportional to its diameter. The capacitance of the patch is directly proportional to the physical patch area. Increasing the patch area makes the antenna physically larger and thus would not be an ideal option, since antenna miniaturization is typically the goal for this antenna. But if we desire to increase the post inductance, the post diameter must be decreased and eventually a practical limitation is reached where the diameter is too narrow for the antenna to be fabricated.

The gap width between the two SM structures controls the coupling between the structures. The simplified version of the microstrip line gap discontinuity can be described as a single series capacitor. The capacitance of the gap increases as the gap narrows in width and vice versa. Figure 4.23 shows how the resonances for the antenna react to changes in the gap width capacitance.

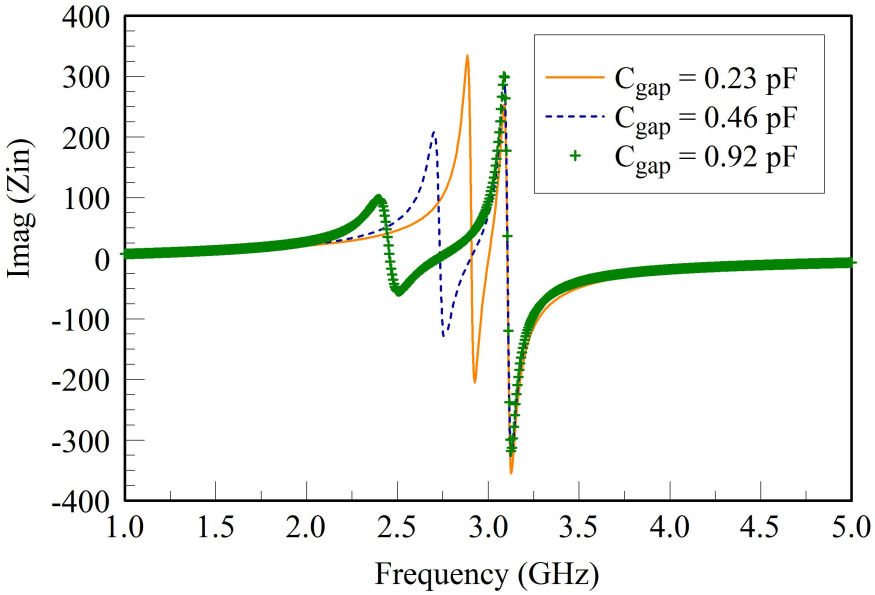

Figure 4.23: Imaginary Impedance Response for Changes in Gap Capacitance

The lower resonance (odd mode) is the mode where the structures are strongly coupled and as such this mode is greatly affected by variation in the gap between the SM structures. As the gap capacitance is increased (or gap width is narrowed) the lower resonance is moved lower in frequency while the upper resonance is essentially unaffected. Thus the lower mode can be controlled independently of the upper mode.

4.6 IWRA: Characteristic Mode Analysis

It is a very beneficial exercise to deconstruct a radiating structure and determine fundamentally which modes are capable of radiating power by performing a characteristic mode analysis on the IWRA. This form of study provides the user with an alternative (more instinctive) approach to determining the true mode of operation of a complex structure by breaking the problem down to the individual modes that are superposed to give the complete response. Recall, the characteristic modes (CM) are current modes that are defined by the shape and size of the conducting body. For a given feed, only the modes that are excited by that feed are supported. The IWRA is fed by a

microstrip gap feed (also known as a proximity-coupled feed). This type of feed will excite the lowest order modes for this structure. The lowest frequency resonance will be referred to as mode 1, the second lowest resonance is called mode 2 and so on. The current distribution for mode 1 is shown in Figure 4.24. Mode 1 corresponds to the odd mode resonance, where the current distribution has odd symmetry across mushroom surfaces.

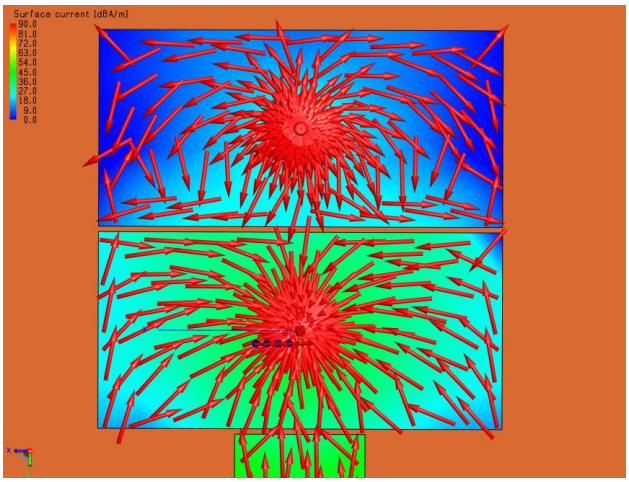

Figure 4.24: Current Distribution for IWRA at Mode 1 ($f_r = 2.6$ GHz)

The current distribution for mode 2 is shown in Figure 4.25. Mode 2 corresponds to the even mode resonance, where the current distribution has even symmetry across mushroom surfaces.

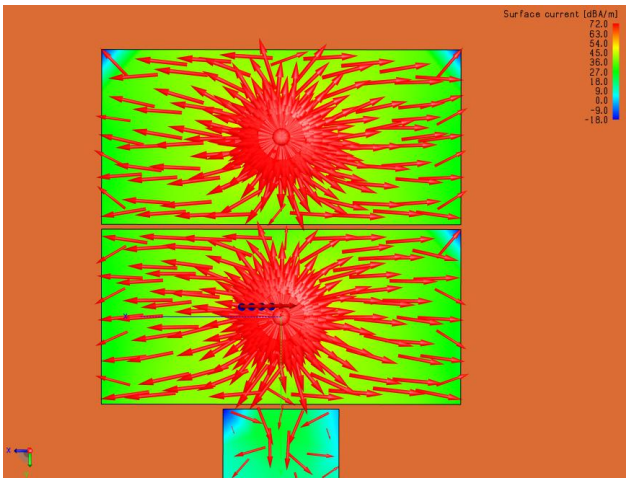

Figure 4.25: Current Distribution for IWRA at Mode 2 ($f_r = 3.44$ GHz)

The third characteristic mode (mode 3) looks like the conventional half-wavelength patch mode, shown in Figure 4.26. It is clear that the main radiating direction is transverse to the direction of the microstrip feed, contrary to the journal paper on which this study is based [32].

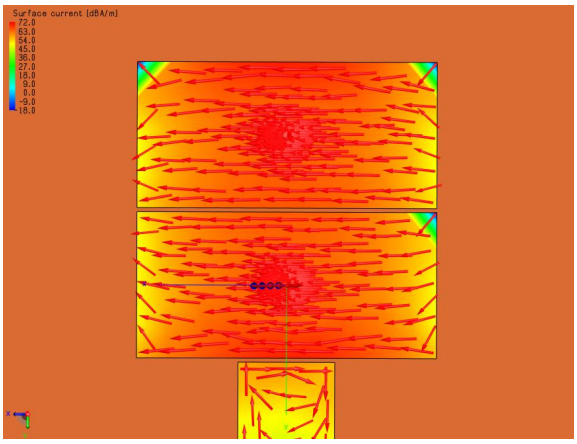

Figure 4.26: Current Distribution for IWRA at Mode 3 ($f_r = 6.2$ GHz)

For comparison, the mode 1 current distribution for a single cell IWRA is shown in Figure 4.27.

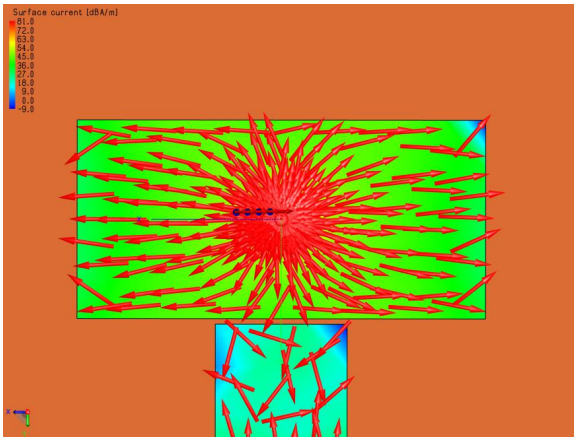

Figure 4.27: Current Distribution for the Single Unit Cell IWRA ($f_r = 3.32$ GHz)

This current distribution closely resembles the typical distribution for the planar inverted-F antenna (PIFA). In fact, the two-cell IWRA can be seen as two closely coupled PIFAs that are not directly fed. The resonant frequency of a PIFA is proportional to the distance of the null-voltage point

to the radiating edge. These principles can be applied to the IWRA in order to drive the resonant frequency down further by moving the shorting post from the center to the corner. By identifying the two-cell IWRA as a closely-coupled cascaded PIFA, it demonstrates that this geometry holds no significant benefit over other antennas of comparable size. Indeed, this analysis brings into question the benefit of the addition of the second cell, which simply introduces a poor radiating mode while increasing the physical size of the antenna.

4.7 Evaluation of IWRA Performance

In order to compare the performance of the IWRA to that of a reasonable benchmark antenna, it was compared to both the Disk Loaded Monopole (DLM) and the Quarter-Wave Patch (QWP) antenna. These comparison cases were chosen because the IWRA radiation characteristics are similar (in the odd mode) to the shorted quarter-wave patch antenna and similar (in the even mode) to the top-loaded monopole. Figure 4.28 shows the return loss responses for the IWRA, QWP and DLM antennas.

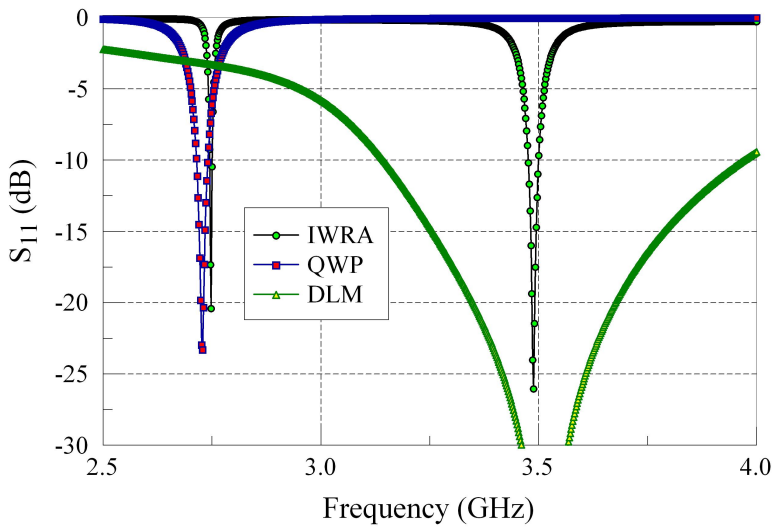

Figure 4.28: Comparison of the Return Losses for IWRA, QWP and DLM

Note the QWP is tuned such that it operates at the lower frequency mode of the IWRA and the DLM is designed to resonate at the upper resonant

mode of the IWRA. The radiation patterns of the two resonant modes for the IWRA are shown in Figure 4.29.

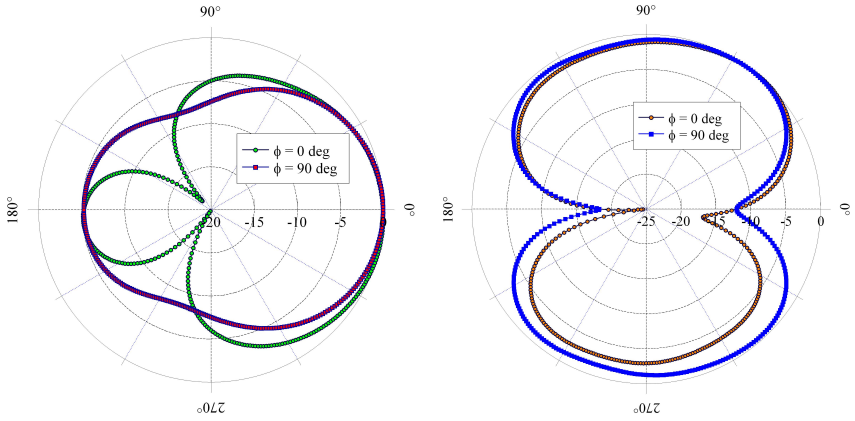

(a) Mode 1 (b) Mode 2

Figure 4.29: IWRA Radiation Patterns (Elevation Cuts) for Mode 1 and 2

The radiation pattern at mode 1 (Figure 4.29(a)) shows a typical broadside radiation pattern which is similar to a conventional microstrip patch antenna. The conventional microstrip patch antenna typically resonates at a frequency that corresponds to a patch length that is half the guided wavelength, but the two unit cell IWRA is closer to $\lambda/4 \times \lambda/4$ in size. Thus the IWRA mode 1 performance is compared with the quarter-wave patch (QWP) antenna which is similar in size and has similar radiation pattern characteristics (Figure 4.30). Figure 4.31 shows the quarter-wave patch (QWP) antenna.

The IWRA's radiation pattern at mode 2 resonance resembles one that is produced by a monopole antenna. In order to decrease the electrical size of the monopole it can be reactively loaded using a metal plate, for example a disk (i.e., forming a disk-loaded monopole). Thus mode 2 resonance of the IWRA is compared to the DLM antenna, and Figure 4.32 shows the DLM antenna radiation pattern at the mode 2 resonant frequency. Figure 4.33 shows the disk-loaded monopole (DLM) antenna.

Note both the QWP and DLM antennas are amended versions of traditional microstrip patch and conventional monopole antennas. The QWP has

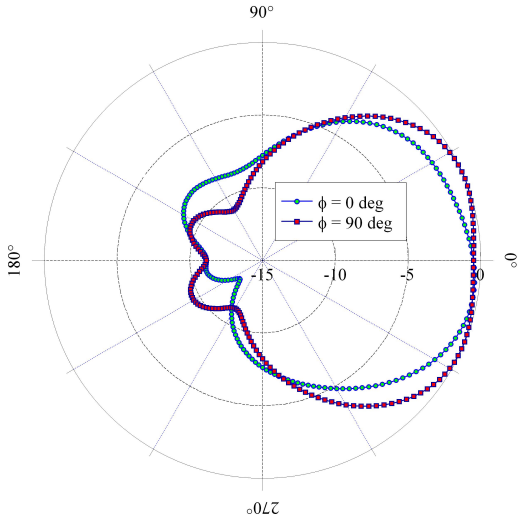

Figure 4.30: QWP Radiation Pattern (Elevation Cut) at Mode 1

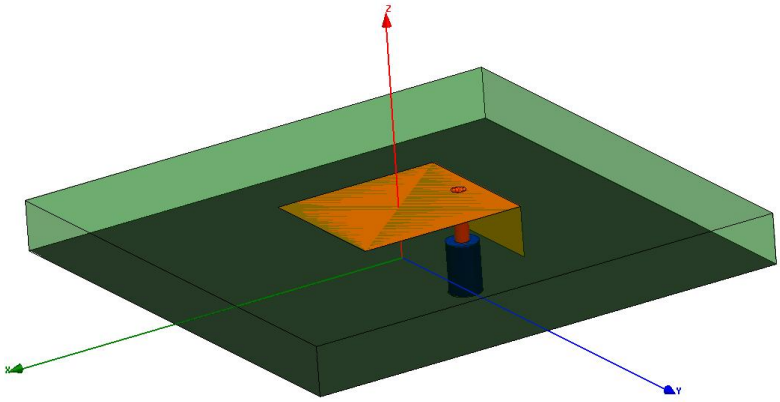

Figure 4.31: QWP Layout (HFSS)

a shorting plane and the DLM has the top hat loading. These modifications are included to force the structure to resonate at a lower frequency (i.e., these are miniaturization techniques). Even with these included the IWRA is still electrically smaller than both the QWP or DLM antennas for the same operating frequency. Table 4.1 shows the comparison of IWRA mode 1 performance compared with the QWP antenna and Table 4.2 similarly compares the IWRA mode 2 metrics to that of the DLM antenna.

The performance data shows that the IWRA operates as a smaller radiator when comparing the relative mode. More specifically, for mode 2 the IWRA is 74% the size for the comparable disk-loaded monopole antenna. The IWRA and QWP operate at electrical sizes for which the IWRA is 6.5%

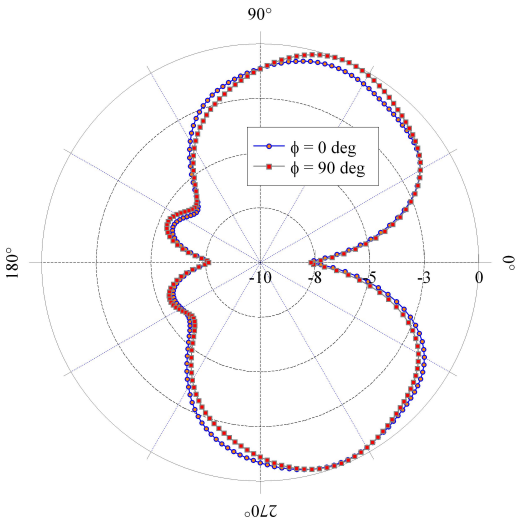

Figure 4.32: DLM Radiation Pattern (Elevation Cut) at Mode 2

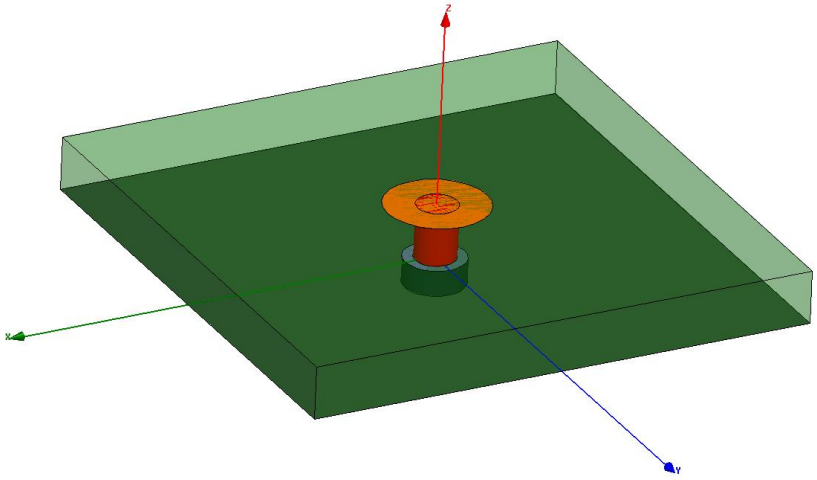

Figure 4.33: DLM Layout (HFSS)

Table 4.1: IWRA Mode 1 and QWP Antennna Comparisons

Property #	IWRA Mode 1	QWP
Fractional BW ($S_{11} \Rightarrow -10$ dB)	0.22%	0.98%
Radiation Efficiency (ϵ_r)	20.5%	87.2%
Electrical Size (ka)	0.92	0.98

smaller. This size reduction is achieved at the expense of other antenna metrics. Both bandwidth and radiation efficiency performance are weaker for the IWRA. The IWRA achieves miniaturization over other antennas with the same operating frequency and radiation pattern. Even with the sub-

Table 4.2: IWRA Mode 2 and DLM Antennna Comparisons

Property #	IWRA Mode 2	DLM
Fractional BW ($S_{11} \Rightarrow -10$ dB)	0.68%	23.4%
Radiation Efficiency (ϵ_r)	81.5%	99.6%
Electrical Size (ka)	1.17	1.58

stantial miniaturization achievement it is interesting to note that the IWRA cannot be classified as electrically small in the traditional sense (because $ka > 0.5$).

4.8 Summary

The IWRA is analyzed using traditional techniques. A circuit model is derived and the operational thesis is applied and verified. The structure is found to essentially be an arrangement of closely coupled indirectly fed PIFAs. Design guidelines are proposed given the determination of the independent sources of resonances. A characteristic mode analysis is conducted and the performance is evaluated against traditional antennas that possess similar radiation characteristics. More generally, an alternative analysis approach is developed which is based on sound fundamental methods and allows for more insight into operation and design than metamaterial theory. In Chapter 5 we investigate more generally the use of reactive loading to miniaturize low profile antennas.

CHAPTER 5

MINIATURIZATION BY REACTIVE LOADING

There are numerous techniques to achieve a more miniaturized planar antenna. The antenna can be made more compact by loading the structure with high-contrast materials, with high permittivity and/or high permeability. There exists for a certain range of values an approximate relation between the size reduction ratio and $\sqrt{\mu_r \epsilon_r}$, which is associated with how wave propagation is slowed in this medium. However, use of high dielectric constant materials often results in narrower bandwidths (due to increased antenna Q) and weak radiation efficiency which is associated with the excitation of surface waves. Additionally, there are many methods for miniaturization based on modifying and optimizing the antenna geometry and shape. These techniques generally involve bending, helical turns, meander-lines, antennas with volumetric curvature and fractal shaping. Slot or notch loading in the radiating element or ground plane is also utilized. Optimization methods, such as genetic algorithms, can be used to achieve the best antenna performance for given size constraints. Though useful these methods offer the user with very little insight into the antenna design methodology.

In the Chapter 4, the IWRA (which has been reported to be a "metamaterial antenna") was investigated in order to determine its mode of operation and its ability to miniaturize planar structures. Its operation was found to be similar to a reactively loaded patch antenna. In the performance comparison we observed that the traditional reactively loaded antennas had good relative performance, examples of these antennas are the top-loaded monopole and the quarter-wave patch antenna. In this chapter, we explore miniaturization of low profile antennas by means of reactive loading. Specifically, how to control the level of miniaturization without changing the volume the antenna occupies.

As an antenna is reduced in size the antenna's input impedance is increasingly dominated by a large reactive component. The introduction of the loading element is used to mitigate the effect of a large antenna input reactance. The reactive load is realized by modifying the existing antenna structure (e.g., Planar Inverted-F Antenna or PIFA can be seen as an inductively loaded patch antenna, where the shorting structure appears as a inductor).

We start this chapter with a review of the ever popular PIFA. The review is followed by a characteristic mode analysis. Given the understanding of the operation for this structure attained in the previous sections, a enhanced PIFA is developed based on meandering techniques and optimum radiator shape. The development of work in this chapter is based on performance optimization for Chu's limit (Equation 2.5).

5.1 Planar Inverted-F Antenna (PIFA)

Planar antennas are extremely popular choices for use in a wide range of applications, especially for hand held terminal applications (e.g., mobile telephone or computer). Many compact planar designs are variants of the PIFA. These planar topologies are capable of reducing the operating frequency substantially by fundamentally changing the resonance mechanism of the antenna. This phenomenon is best understood by exploring the evolution or development of the PIFA. The PIFA is a hybrid antenna configuration between the traditional quarter wavelength monopole and the microstrip patch antenna. Figure 5.1 shows the progression to the PIFA design.

The conventional straight-wire monopole is a quarter wavelength long (Figure 5.1(a)) and is fed at its base over a large ground plane. The straight-wire monopole is a resonant antenna. Its current distribution is sinusoidal with minimum current at the monopole apex while the maximum current is found at the feed point (or monopole base). The ILA (Figure 5.1(b)) is formed by applying a right angle bend to the straight wire monopole. This effectively miniaturizes the antenna height. The current distribution for the ILA is similar to the straight monopole, but the horizontal wire segment does

contribute to the cross polarization levels in the radiation pattern. When the ILA's horizontal dimension is reduced, the input impedance becomes reactive dominant, and in order to achieve an impedance of close to 50 Ω we incorporate a shorting stub, thus forming the Inverted-F Antenna (IFA), shown in Figure 5.1(c). Replacing the horizontal wire of the IFA with a planar conducting plate we obtain the Planar Inverted-F Antenna, shown in Figure 5.1(d). The PIFA is a resonant antenna that operates at a frequency where the patch length is approximately $\lambda/4$, effectively reducing the lateral size by at least 50% over the conventional microstrip patch.

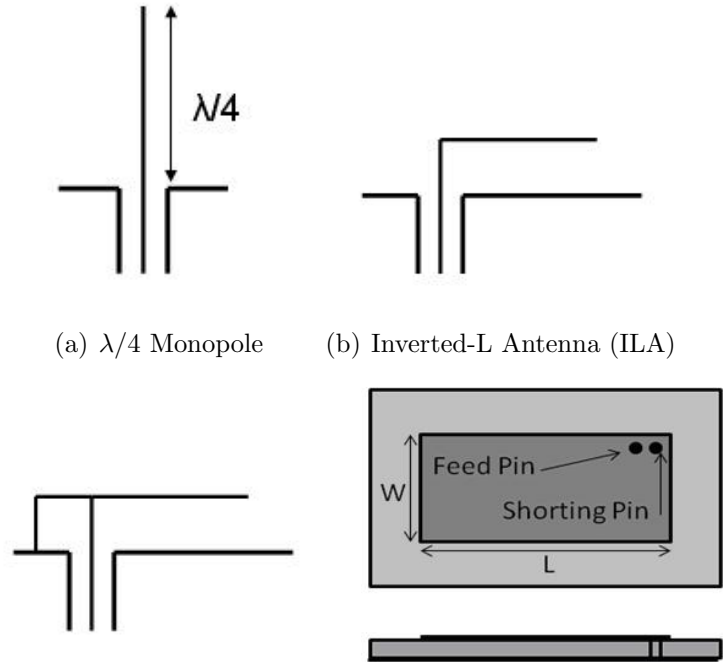

(a) $\lambda/4$ Monopole (b) Inverted-L Antenna (ILA)

(c) Inverted-F Antenna (IFA) (d) Planar Inverted-F Antenna

Figure 5.1: Development of the PIFA

Another way to think about how the PIFA operates is to examine the electric field distribution for the conventional microstrip patch antenna. Figure 5.2(a) depicts the layout for the conventional probe-fed rectangular patch antenna with the electric field distributions for the fundamental radiating mode [46]. The electric field is maximum at the radiating edges and zero at the patch center, exhibiting a half sinusoidal distribution.

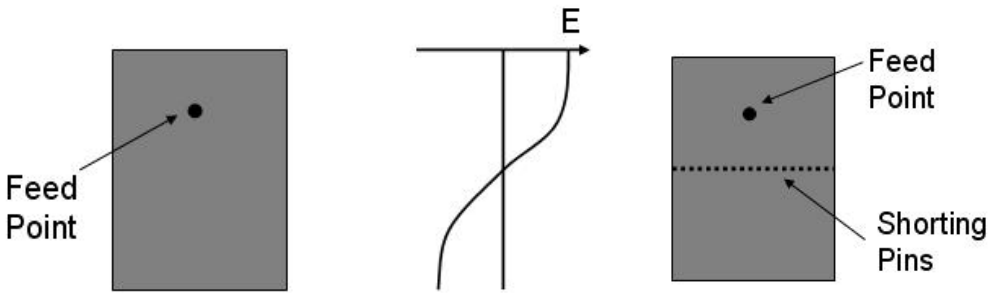

(a) Conventional Patch (b) Patch with Shorting Pins

Figure 5.2: Patch Electric Field Analysis [46]

The patch antenna with shorting pins (Figure 5.2(b)) has the identical electric field distribution since the pins do not disturb the field because it is zero at the patch center. Thus the second half of the patch is not excited in this case and can be removed, effectively creating a quarter wavelength patch antenna [47]. When the number of shorting pins is reduced, the resonant frequency is decreased, resulting in a more compact antenna. This is because the inductive load is inversely proportional to the number of pins. Further compactness can be achieved by utilizing a single shorting pin that is placed at the patch corner. The placement of the shorting pin at the corner forces the patch currents to take the longest path possible (longer current paths mean lower resonant frequencies). Figure 5.3 depicts the current path trajectory of two shorted patches, one where the entire width is shorted (Figure 5.3(a)) and the other where a single pin is placed at the corner (Figure 5.3(b)).

Given the current path trajectory for the PIFA with single shorting pin at corner, it is fair to approximate the resonant frequency as

$$f_r = \frac{c}{4(W+L)} \tag{5.1}$$

where c is the speed of light, W and L are the width and length of the patch. Equation 5.1 is fairly accurate for a PIFA with low height profile (i.e., h $\ll \lambda$). PIFA antennas are typically designed to operate in an air substrate medium and as such the relative permittivity of parameter is not included in Equation (5.1). This equation gives a good first approximation for the

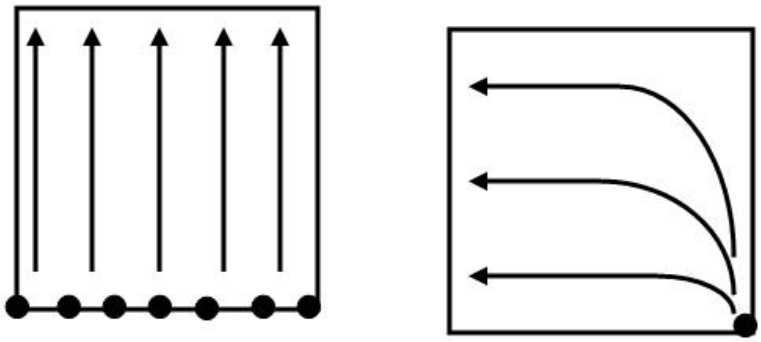

(a) Shorting Wall (b) Shorting Pin at Corner

Figure 5.3: Current Path Analysis [46]

resonant frequency of a single frequency PIFA but does not include post diameter, post length etc., which all affect the inductance presented by the shorting pin and consequently the resonant frequency. Nonetheless, the four in the denominator in Equation (5.1) gives an indication of the magnitude of size reduction that is capable with this topology. It is obvious that the radiation mechanism of the PIFA is no longer patch-like ($\lambda/2$ resonator) but rather monopole-like ($\lambda/4$ resonator). The primary attribute of the PIFA is the antenna miniaturization it can attain. As far as drawbacks, the relative bandwidth for the PIFA fundamental mode is narrow and the fabrication of the PIFA can be very difficult due to the close proximity of the feed and the shorting pin in order to excite the lowest order mode with a good 50 Ω match.

5.2 Shorted Patch: CM Analysis

The PIFA is also commonly known as a "Shorted Patch Antenna." Once again this antenna structure will be evaluated using characteristic modes (CM). This mode of analysis is effectively breaks down the antenna analysis problem into the individual modes that make up the total response. As a reference the conventional rectangular microstrip patch antenna (RMPA) is shown in Figure 5.4.

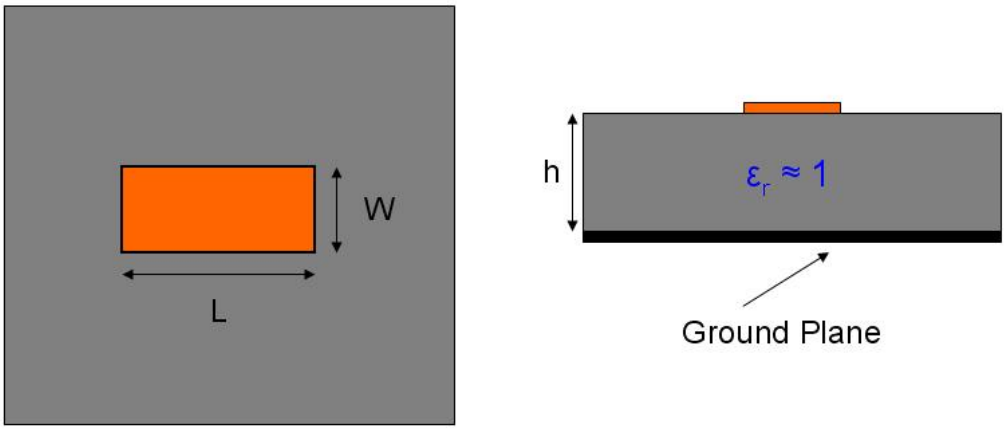

Figure 5.4: Rectangular Microstrip Patch Antenna (RMPA)

The dimensions of the patch (W x L) are 1.5 cm x 3 cm. The height (h) is 1.8 cm, which is relatively large, but is intended to enhance bandwidth capabilities and is chosen will future fabrication in mind. The patch radiator is suspended above the ground plane by an air substrate (realized by styrofoam in fabrication). Figure 5.5 shows the current distribution for mode 1 which resonates at 3.85 GHz. Mode 1 is the familiar TM_{10}, half sinusoid distribution, with current maximum at the patch center and current minimum at the radiating edges.

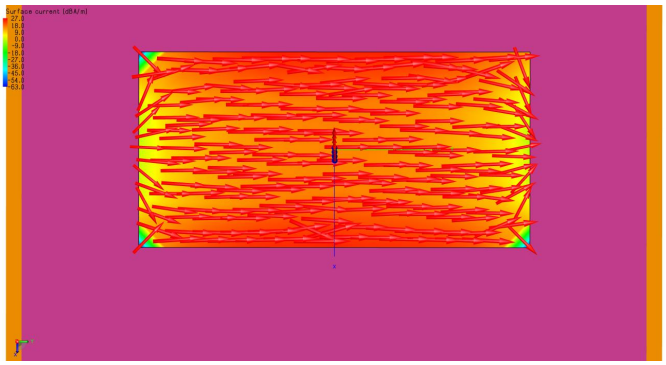

Figure 5.5: RMPA Mode 1 (3.85 GHz)

The patch with narrow shorting strip (planar version of the pin) is simulated and its lowest frequency mode's current distribution is shown in Figure 5.6(a). For this structure the lowest mode's current distribution is a quarter sinusoid, the current maximum is at the shorting strip's base and the current minimum is at the radiating edge ($f_r = 1.08$ GHz). As the strip

is widened to the full width (forming the standard quarter wavelength patch antenna) the inductance associated with the strip decreases, forcing the resonant frequency higher. Figure 5.6(b) shows the quarter wavelength patch antenna and its resonant frequency for mode 1 is $f_r = 1.52$ GHz.

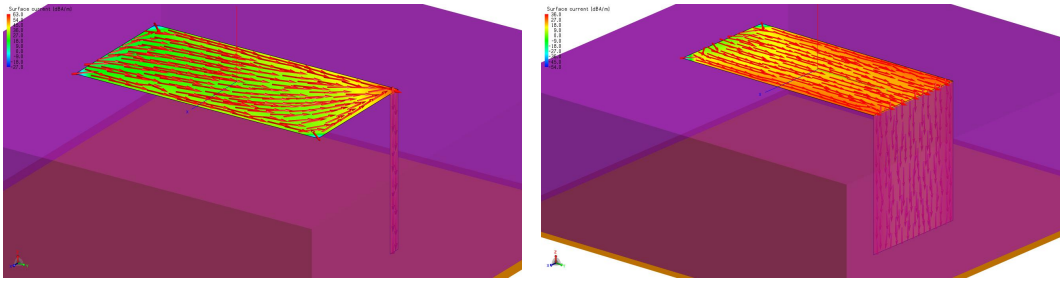

(a) Narrow Strip (1.08 GHz) (b) Wide Strip (1.52 GHz)

Figure 5.6: Shorted Patches

The miniaturization factors for the two shorted patch versions relative to the RMPA are tabulated in Table 5.1.

Table 5.1: MFs for Two Types of Shorted Patches

Shorted Patch Type	MF
Wide Strip	2.53
Narrow Strip	3.56

Given the superior miniaturization capabilities of the PIFA structure, it is logical to use it as a base to launch further miniaturization techniques. Next, an investigation into the potential to drive the resonant frequency down further by meandering the shorting strip.

5.3 PIFA with Meandered Shorting Plane

The meandered shorting plane is formed by strategically cutting slots from the shorting plane. For the analysis, two profiles for the meandered short were chosen, a gentle step-shaped meander line (Figure 5.7(a)) and a more

aggressive profile termed a S-shaped meander line (Figure 5.7(b)).

(a) Step Meander (b) S-shaped Meander

Figure 5.7: Meander Short Profiles

The CM analysis shows that the fundamental mode resonant frequency has indeed been decreased due to the lengthening of the current path to the short (i.e., increased inductive loading). The resonant frequency for the step meander short is $\approx$ 950 MHz and the S-shaped meander short is even lower at around 820 MHz. These miniaturization enhancements are included in Table 5.2, where the miniaturization factors are shown when compared to the original microstrip patch antenna operating frequency.

Table 5.2: Miniaturization Factors Including Meandered-Shorted Patches

Type of Shorting Plane	MF
Wide Strip	2.53
Narrow Strip	3.56
Step Meander	4.05
S-shaped Meander	4.7

As in many aspects of engineering there are tradeoffs and this case is no different. By increasing the number of round trips the meander line takes (i.e., decreasing the pitch) the lowest mode frequency is moved ever lower but there is a price, namely antenna performance deterioration (i.e., lower radiation efficiency). In order to evaluate the meandered shorting strip patch antenna the complete antenna including feed is simulated in Ansoft HFSS, a full wave electromagnetic solver. At this stage it is well understood that

this antenna behaves in a monopole-like manner (i.e., quarter wavelength distribution) thus it is essential to place the probe feed close to the shorting structure in order to adequately excite the desired mode. The meandering action taken to lengthen the shorting path has the effect of increasing the inductance of the shorting strip and as such a capacitively coupled feed is required to neutralize the reactance and approach a real 50 Ω impedance. The most straightforward feeding mechanism is simply placing the probe in close proximity to the meander line (exterior to patch boundary), as shown in Figure 5.8.

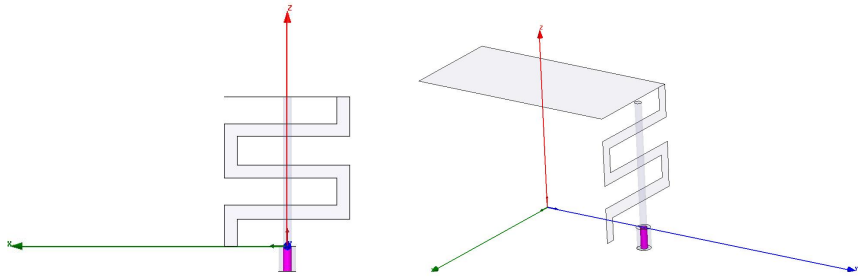

(a) View 1 (b) View 2

Figure 5.8: Proximity-Coupled Probe Feed Mechanism

A more fabrication-friendly feeding mechanism that avoids the need for as close a proximity arrangement of the meander structure and the probe is shown in Figure 5.9. This feed method has the probe on the interior of the patch, the probe has a small circular disk at its end and a relatively narrow coupling gap between the disk and the bottom side of the patch. The disk coupled feed provides more flexibility and thus a match to the system impedance is easier to implement. Additionally, with the feed mechanism on the interior the antenna is a more compact unit.

Simulations for both feed configurations (Disk-Coupled and Pin-Coupled) as well as for the two short circuit meander line profiles (Step and S-shaped) are conducted in the full wave solver HFSS by Ansoft. In order to quickly identify the specific configuration we use short labels which make reference easier (Table 5.3). Figure 5.10 shows the reflection coefficient frequency response data for the different feed and shorting mechanism profiles.

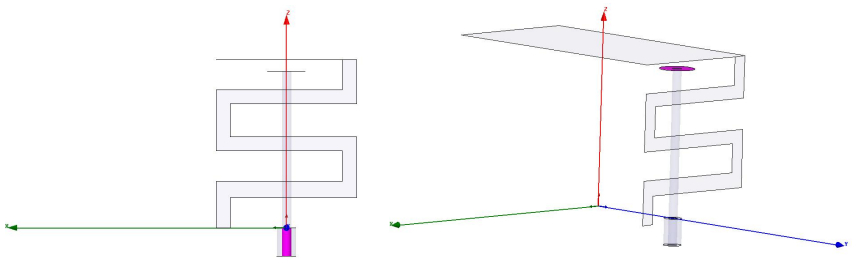

(a) View 1 (b) View 2

Figure 5.9: Disk-Coupled Probe Feed Mechanism

Table 5.3: Antenna Labels for the Feed and Shorting Configurations

Label	Configuration
A	Pin-feed, Step Short
B	Disk-feed, Step Short
C	Pin-feed, S-shaped Short
D	Disk-feed, S-shaped Short

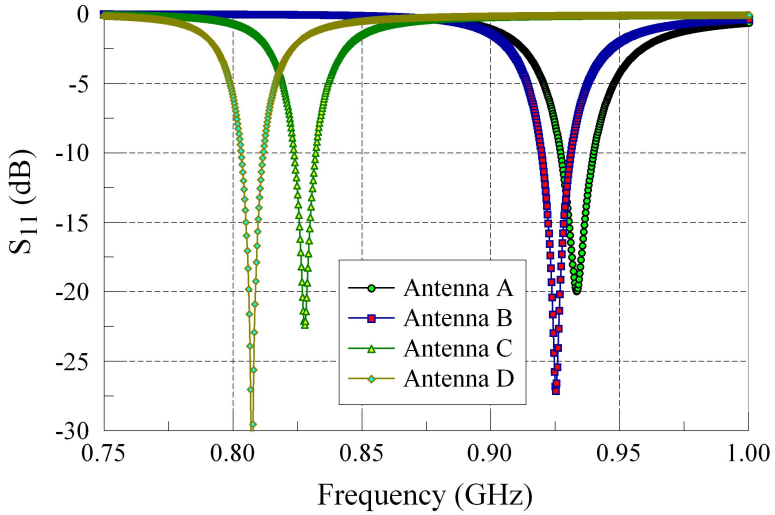

Figure 5.10: Reflection Coefficient for Various Feeding and Shorting Profiles

Some specific antenna performance parameters for the antenna models are shown in Table 5.4. Note that miniaturization factors are based on miniaturizing the original conventional patch (RMPA $f_{res} = 3.85$ GHz).

Table 5.4: Performance Parameters for Various Feed and Shorting Configurations

Parameter	Antenna A	Antenna B	Antenna C	Antenna D
f_{res} (MHz)	932.2	919	825.2	809.8
MF	4.13	4.19	4.67	4.75
ka	0.48	0.474	0.425	0.417
BW (MHz)	12.8	11.8	9	8.8
BW (%)	1.37	1.28	1.09	1.09
η (%)	88.9	89.3	78.6	77.1

As expected, the resonant frequency is decreased with a lengthening of the current path (i.e., S-shaped meander profile produces an antenna with lower operating frequency than the Step meander). As the antenna electrical size, ka, is lowered, the impedance bandwidth shrinks and the radiation efficiency drops. It is well known that structures with meander lines generally have weaker radiation efficiencies. This is because the structure supports current vectors that oppose one another in certain segments and consequently would yield some cancellation of generated fields and thus weaker radiation. Given this phenomenon, we have a tradeoff between the radiation performance and the level of miniaturization given the amount of meandering. Interesting to note that all the antenna models achieve small antenna status (i.e., $ka \leq 0.5$). Comparing the performance difference for the two feed methods it is observed that the disk-fed method offers additional miniaturization with comparable performance.

The rectangular shape of the antennas analyzed thus far make very poor use of the antenna spherical volume, this is depicted in Figure 5.11. Recall from the chapter on small antenna theory that optimum performance requires maximum use of spherical volume enclosing the antenna. A better use of volume, while maintaining the planar constraint, is to replace the rectangular patch with a circular patch. The circular patch would have a diameter equal to the rectangular patch diagonal length, as shown in Figure 5.11. Figure 5.12 shows the circular microstrip patch antenna (CMPA) with a curved step meander shorting strip.

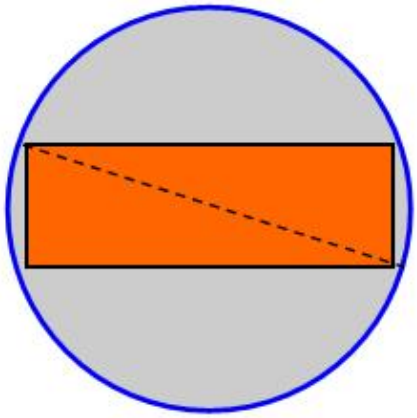

Figure 5.11: Top View, RMPA Inside Antenna Sphere

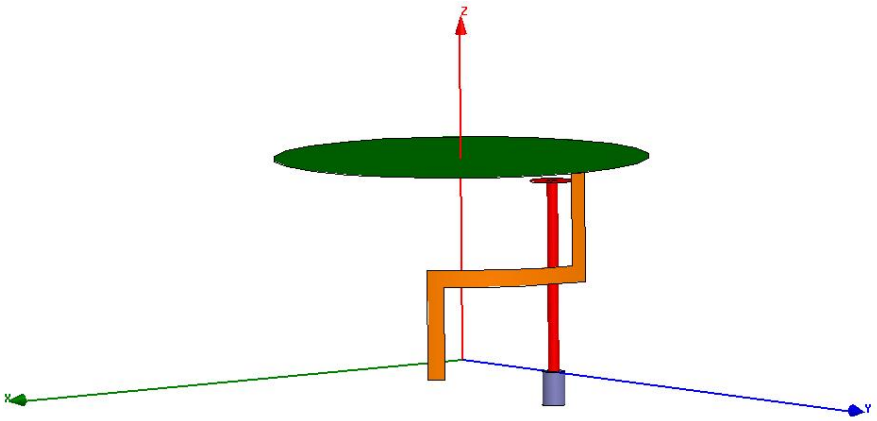

Figure 5.12: CMPA with a Curved Step Meander Shorting Strip

Given that the circular patch simply circumscribes the original rectangular patch and that the resonant frequency of the CMPA is related to its diameter, the resonant frequency will be lower than the RMPA. Thus for a given MF we can utilize a less aggressive meander profile for the shorting mechanism. Fewer turns in the meander short translate to higher radiation efficiency because there will be fewer paths with opposing current directions. The return loss frequency response for the CMPA with the two meander short profiles are shown in Figure 5.13. Given the advantages of the disk-feed mechanism highlighted earlier, this feed method is used to evaluate all future models in this chapter.

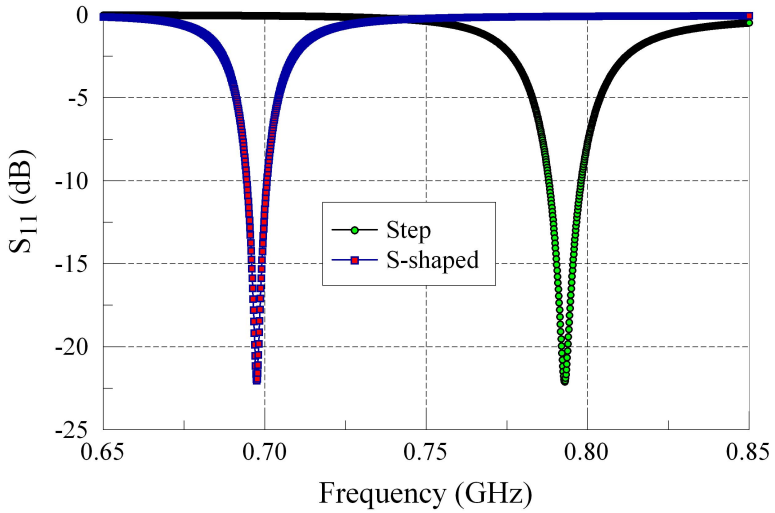

Figure 5.13: Reflection Coefficient for CMPA with a Curved Step and S-shaped Meander Shorting Strip

Once again a table is provided with some antenna performance parameters for the CMPA with the two shorting profiles (Table 5.5). Recall, the miniaturization factor data is referenced to the original conventional rectangular patch antenna (RMPA $f_{res} = 3.85$ GHz).

Table 5.5: Performance Parameters for CMPA with Different Shorting Configurations

Parameter	Step Meander	S-shaped Meander
f_{res} (MHz)	792.9	691.1
MF	4.86	5.57
ka	0.409	0.356
BW (MHz)	10.1	7.8
BW (%)	1.27	1.13
η (%)	85.4	71.4

The circular patch with the S-shaped meander short configuration yields the lowest operating frequency planar antenna thus far, it has a extremely small electrical size ($ka = 0.356$) and also the bandwidth and efficiency performance are adequate for most applications. The choice to switch a circular patch is justified by comparing the performance of the RMPA with the S-shaped meander (Antenna D) and the CMPA with the Step meander shorting profiles. The data is repeated in Table 5.6 for convenient viewing.

Table 5.6: Performance Comparison of the S-shaped Meander Shorted RMPA and the Step Meander Shorted CMPA

Parameter	S-shaped meander shorted RMPA	Step meander shorted CMPA
f_{res} (MHz)	809.8	792.9
MF	4.75	4.86
ka	0.417	0.409
BW (MHz)	8.8	10.1
BW (%)	1.09	1.27
η (%)	77.1	85.4

The CMPA operates at a slightly lower frequency than the RMPA. Thus it achieves a slightly better miniaturization factor and smaller electrical size. The bandwidth is larger for the CMPA model since it better utilizes the available volume and also it achieves improved radiation efficiency because of the less aggressive meander profile choice. Thus using the circular-shaped patch allows for better performance for a given volume versus the rectangular patch.

5.4 Summary

The investigation into the miniaturization of planar antennas is conducted is a systemic and logical manner. Starting with a conventional rectangular microstrip patch antenna (RMPA) which is a resonant antenna with its lowest operating frequency corresponding to a patch length to a half wavelength. Next, the patch antenna is drastically altered with the addition of a shorting element. This fundamentally changes the resonant behavior such that now its lowest order mode corresponds to $\approx \lambda/4$. It was found that the resonant behavior of the shorted patch was controlled by the inductance presented by the meandered shorting structure; the larger the inductance will result in the lower resonant frequency. The inductance of a metal strip is directly proportional to its length and inversely proportional to its width (thus increase inductance of strip by making it longer and thinner). Making the shorting strip narrower has practical and performance limitations and has been widely evaluated, here we focus on the lengthening of the strip to achieve in-

creased loading. In order to facilitate the lengthening of the shorting strip in a confined space it is meandered. Two meander profiles (Step and S-shaped) were investigated. Finally, in order to improve performance relative to Chu's limit we optimize the patch geometry to maximize area coverage in the Chu sphere by making the patch circular. Some of the questions that arose during this portion of the research were: (1) can a lumped inductor be used for inductive loading of an antenna (or radiating structure) and what are the performance tradeoffs associated with lumped inductor loading, and (2) how does the antenna design perform for even lower antenna height restrictions and can we achieve better performance by moving to a short-fat structure (i.e., compensate patch height reduction by increasing the patch radius so that thw volume remains constant)?

This chapter served as introduction or concept chapter for Chapter 6: Antenna Miniaturization for Fixed Volume Applications. The concept of controlling miniaturization of a fixed volume antenna design by increasing the loading is further explored. The performance of future designs are compared to theoretical limits based on their actual volume shapes (e.g., cylindrical shaped antenna compared to Gustafsson's limit for cylindrical volumes). The questions from this chapter are addressed, namely those pertaining to lumped inductor loading and antenna height reduction scenarios. Additionally, a design for bandwidth enhancement of the antenna is proposed and evaluated.

CHAPTER 6

ANTENNA MINIATURIZATION FOR FIXED VOLUME APPLICATIONS

In this chapter, a antenna design is proposed that can be miniaturized within a fixed volume. The motivation for such an antenna design problem stems from applications that require electrically small antennas with frequency agility and are constrained by package size. As shown in the previous chapter, the PIFA represents a good tradeoff design of a miniaturized design with adequate performance. In this chapter the PIFA design is extended to encourage further miniaturization, all while holding the volume the antenna occupies constant.

There are essentially two parameters that can be used to increase the inductance of a distributed shorting strip (e.g., metal copper strip), these are to make the shorting strip/pin narrower or to increase its length. The PIFA structure has a quarter wave current distribution with the peak current located at the shorting strip base. Narrowing the shorting strip would increase the effective resistance of the line, the large resistance in conjunction with high currents due to the mode distribution can result in significant power loss (I^2R losses). Additionally, it can be difficult to accurately control the thickness of the strip during fabrication and thus it not desired for it to be a critical design dimension. Given these issues it is best to pursue the other means of achieving antenna miniaturization, that being the lengthening of the shorting strip.

It is necessary to increase the antenna height (from the conventional PIFA design) so that there is sufficient room for the lengthened shorting trace. This allows for the evaluation of numerous meandering styles that can be employed to allow for further increase in length. With an increase in antenna height and longer shorting trace lengths, the antenna no longer behaves like a PIFA and is now essentially an Inductively loaded, Top-loaded Monopole Antenna

or Dual Reactively Loaded Monopole (DRLM) Antenna. Figure 6.1 shows the DRLM antenna, the geometrical profile of this shorting strip is designated as the Step profile, since the traditional vertical strip is interrupted with a horizontal step.

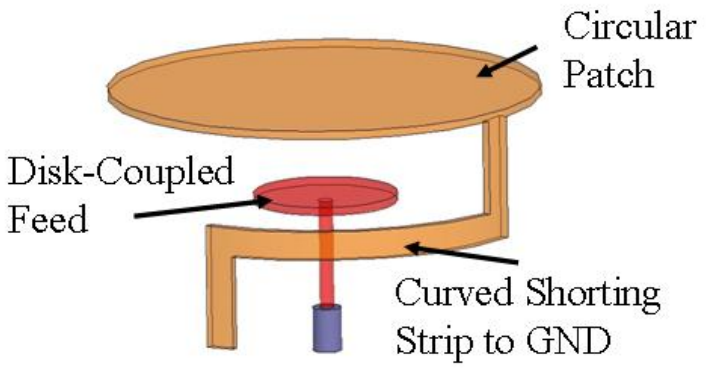

Figure 6.1: DRLM with Step Profile Shorting Strip

The PIFA is commonly implemented on a rectangular patch element but this is replaced for a circular patch because our intention is to compare the antenna's performance against Gustafsson's limit for cylindrical volumes. The antenna volume is cylindrical and is fully described by its height and radius (or diameter). The shorting strip is curved along the perimeter of the patch. This is done to satisfy the constraint that the entire antenna be enclosed in a fixed volume and still achieve varying degrees of miniaturization without increasing the size of the antenna. Finally, the antenna is probe-fed by a proximity-coupled disk. This allows for flexibility in fabrication, with two degrees of freedom (the gap between the feed disk and the patch and the radius of the feed disk) to establish a good match.

6.1 Miniaturization Mechanism

Lengthening of the shorting strip can be achieved in a variety of meander styles. Four types of meandered shorting geometries are evaluated. They are designated as the following:

- Step Profile
- Horizontal Meander Profile

- Vertical Meander Profile
- Helical Profile

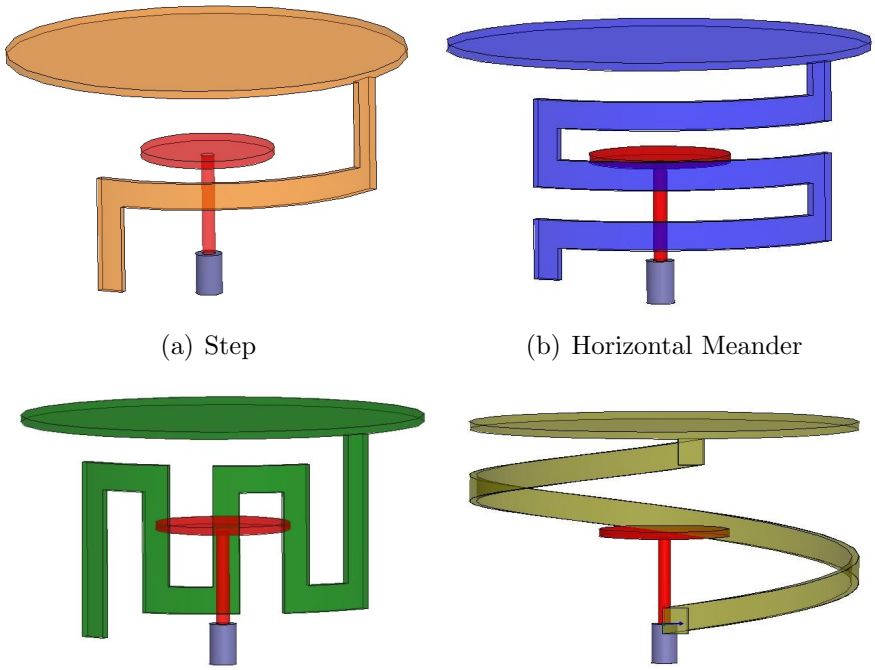

(a) Step (b) Horizontal Meander

(c) Vertical Meander (d) Helical

Figure 6.2: Shorting Profile Geometries

The Step profile is formed by introducing a step in a vertically aligned shorting strip, see Figure 6.2(a). The horizontal section of the step profile can be extended to increase the path length of the shorting structure and thereby force a lower frequency of resonance. The arc length of the horizontal section can be described by the subtended angle, called the Shorting Profile Angle (SPA) or α. Figure 6.3(a) shows a step-meandered PIFA with $\alpha = 90°$. Figure 6.3(b) is annotated with relevant labels that are common to all models. The patch height and radius are given by P_H and P_R, respectively. Similarly, the feed disk height and radius is described by FD_H and FD_R, respectively. The antenna dimensions are as follows: patch height (P_H) = 1.5 cm and patch radius (P_R) = 1.5 cm. The feed dimensions (FD_H and FD_R) are adjusted in order to achieve good match to the 50 Ω standard. The feed position is kept static at the origin.

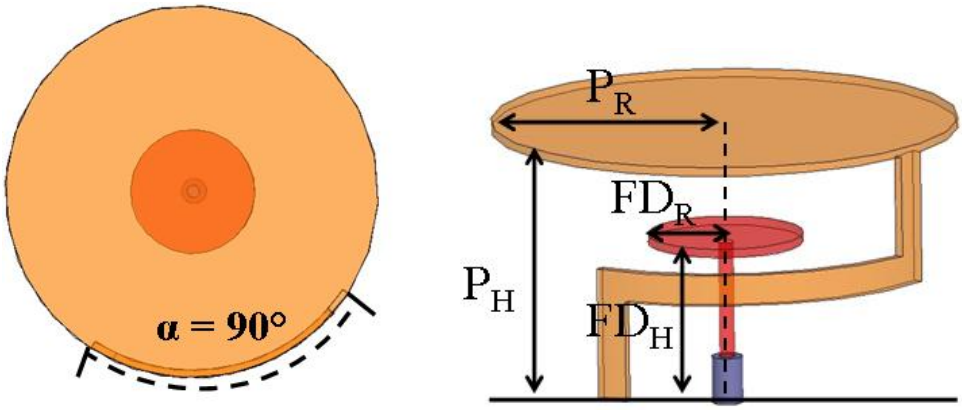

(a) Top View (b) Front View Annotated

Figure 6.3: Step ($\alpha = 90°$) - DRLM Antenna

The horizontally meandered PIFA is shown in Figure 6.2(b). As shown, the shorting structure is formed by replacing the vertically aligned shorting strip by a meandered line. The horizontal meander line is characterized by longer horizontal sections than vertical sections. The number of meandered sections in the line is a function of the patch height and the line width (for this study, the topology of three equally spaced horizontal segments has been chosen). Similarly, the vertically meandered PIFA is constructed with the long segments in the vertical directions while shorter segments are found in the horizontal direction as shown in Figure 6.2(c).

The three profiles mentioned thus far (step, horizontal and vertical) have an associated shorting profile angle (α) which is used primarily to control the resonant frequency. The larger α is, the lower the resonant frequency and vice versa. The miniaturization capabilities are evaluated for the Step, Horizontal and Vertical meandered profiles for a fixed volume antenna. Figure 6.4 shows the achievable electrical sizes given by ka of the various antennas with variation in α. The range of α is different for each profile but there is overlap between $90° \leq \alpha \leq 270°$. The difference in α ranges for the profiles are based on the useful bandwidth at the high end ($\alpha > 270°$) and due to geometry on the low end ($\alpha < 90°$). For example, for values of α below 90°, the vertical meander profile has its vertical segments too close to each other and for α larger than 270° the bandwidth-efficiency product is too low to be useful.

The entire electrical size (ka) range is between 0.2 and 0.46, this corresponds to a frequency range of $\approx$ 0.5 - 1 GHz. In terms of specific electrical dimensions, the patch height and radius assume dimensions between 0.025 λ_0 and 0.05 λ_0 while the patch circumference ranges between 0.118 λ_0 and 0.236 λ_0.

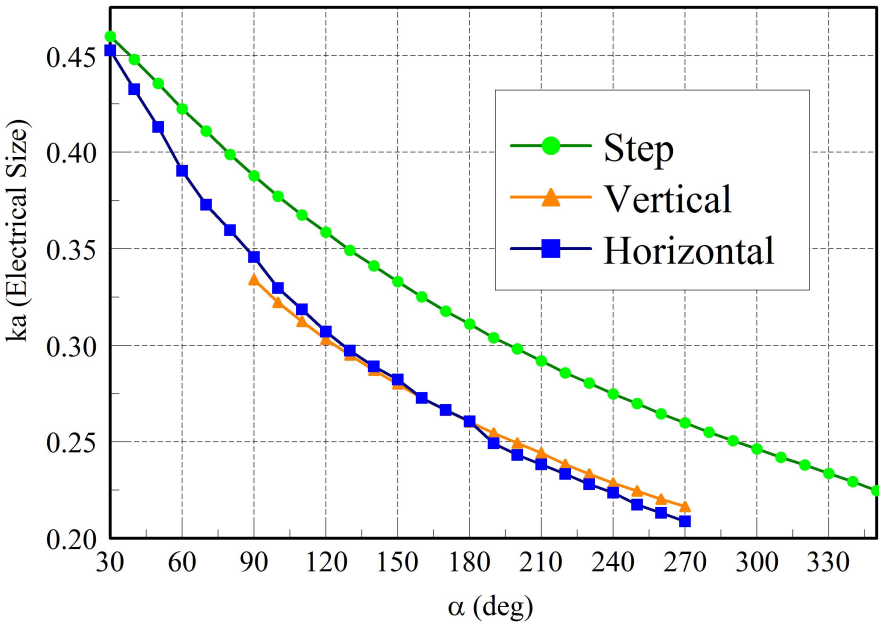

Figure 6.4: Electrical Size for the Step, Horizontal and Vertical Meandered Profiles as a Function of α

As shown in Figure 6.4, as the shorting profile angle is increased, the electrical size for the antenna decreases monotonically. As α is increased the electrical size for the Step and Horizontal-Meandered Profiles diverge, the vertical difference between the curve represents the "miniaturization gain" of one profile over the other. The Horizontal- and Vertical-Meandered profiles operate at similar electrical sizes for a given α, the corresponding Step profile model is consistently electrically larger. Note that for lower values of α (below 180°) the Horizontal profile is fractionally larger electrically versus the Vertical case. For α larger than 180° the situation is reversed, with the Horizontal case now electrically smaller than the Vertical. A slight nuance about this experiment needs to be explained in more detail here regarding the Horizontal and Vertical profiles. The Horizontal profiles structure essentially remains the same as the shorting profile angle increase, so the only thing that changes is that horizontal sections get longer. The Vertical profile

changes in a similar fashion (i.e., the horizontal sections get longer while the number of vertical sections remain the same). A simplistic way to visualize this is to imagine the vertical profile as a spring that is compressed when α is small and is stretched out when α is increased. The vertical geometry is constrained to this growth trajectory to simplify the analysis and make it as linear a process as possible. Thus the vertical profile displays a plateau effect, a situation where for increasing values of α, the amount of miniaturization attained is reduced. This allows the Horizontal profile case to surpass the Vertical as the profile to produce the smallest antenna for high values of α. Finally, the Helical - DRLM Antenna is shown in Figure 6.5. It is constructed by wrapping the shorting strip in a helical fashion. The level of miniaturization for the helical model is controlled by adjusting the pitch. Figure 6.6 shows the range of electrical sizes attained by the antenna for a range of pitch values.

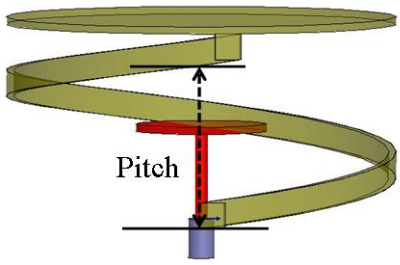

Figure 6.5: Helical - DRLM Antenna

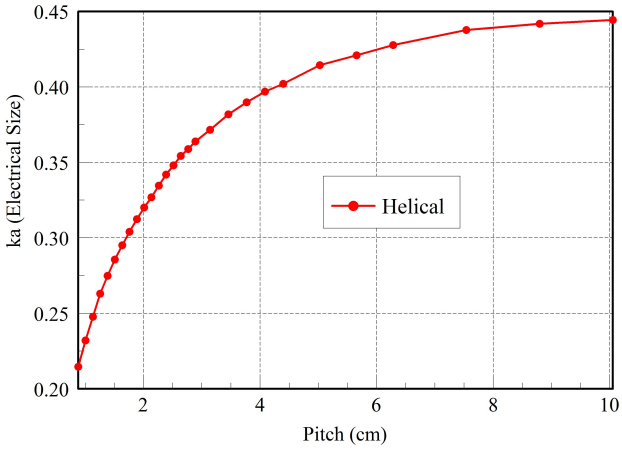

Figure 6.6: Helical - DRLM Antenna, *ka* vs. Pitch

Given that the method of describing the tuning parameters for the models are difficult because the Step, Horizontal and Vertical profiles are described by the shorting profile angle and this does not exist for the Helical case (where it is instead described by the pitch). Alternatively, in Figure 6.7 we plot the electrical sizes from the data in Figure 6.4 and 6.6 but in terms of the shorting trace length, β.

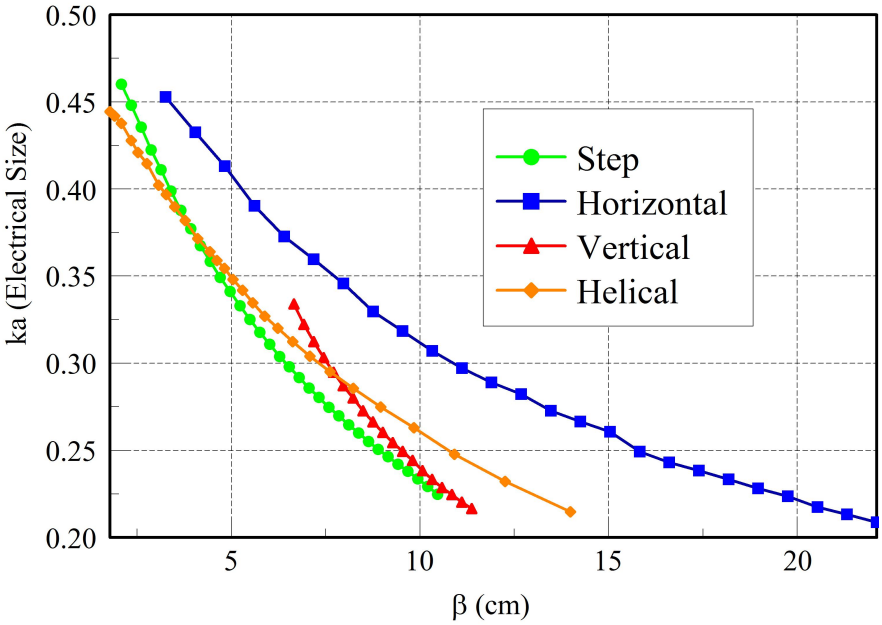

Figure 6.7: Electrical Size vs. β

The trace length can be used as a proxy for the cost and complexity of the antenna fabrication (i.e., a larger β is harder to mill, shape, and solder in place accurately). Figure 6.7 shows that for a given electrical size the Step profile is the shortest while the Horizontal profile would be by far the longest trace, with the Helical case being the second longest. Given that the levels of miniaturization of the Horizontal and Vertical profiles are similar, it is clear that the antenna with a Vertical profile would be easier to realize.

Figure 6.8 shows the bandwidth-efficiency product versus ka for the antenna with the various shorting tab profiles, all compared to the Gustafsson limit for a cylinder with $\zeta = 1$. Note that the physical volume is held constant while the electrical volume is tuned by adjusting the shorting profile angle (α) and the pitch where appropriate. Figures 6.9 and 6.10 show the

ka range divided into two regions, this enables the reader to better see the variation in the data.

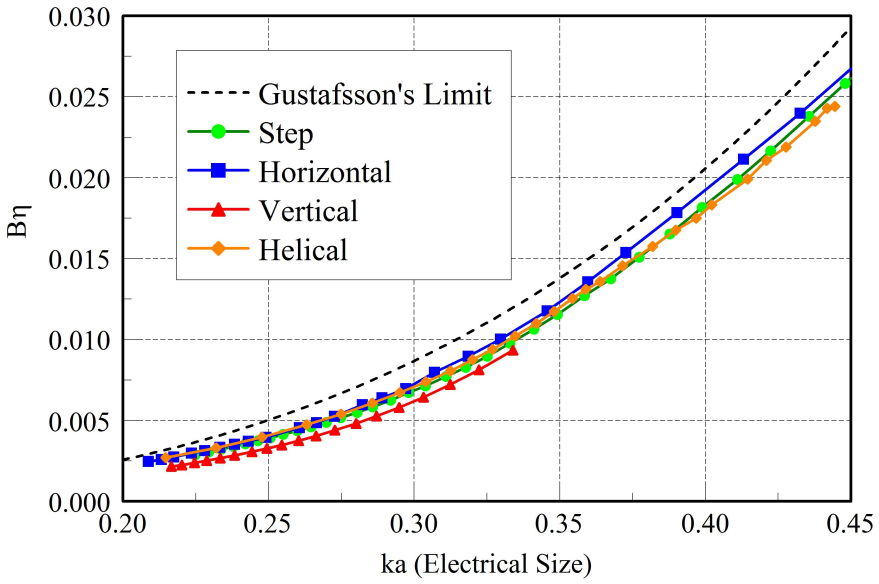

Figure 6.8: Bandwidth-Efficiency (Bη) vs. ka Compared to Gustafsson's Limit

We observe that comparable performance for the Horizontal, Helical and Step profiles for $ka \leq 0.3$ while above this ($0.3 \leq ka \leq 0.35$) the Horizontal profile marginally outperforms the rest. The Vertical profile is a clear laggard of the group for the entire range. The Vertical profile is a structure that has the current path meandering along the vertical direction (or perpendicular to the ground plane). These currents are the main source of the radiating field in a monopole-type antenna. Thus meandering in this direction results in opposing currents in close proximity and consequently a field that undergoes destructive interference. As a result the performance, in particular the radiation efficiency is weaker than the non-vertically meandered profile antenna models.

The upper range ($0.35 \leq ka \leq 0.46$) shows a outperformance by the Horizontal profile once again. The marginal outperformance by the Horizontal profile model can be attributed to the fact that it utilizes the antenna volume better than the other profiles. The trace length is longer and its geometrical shape realizes an effective area larger than the Step and Helical profiles,

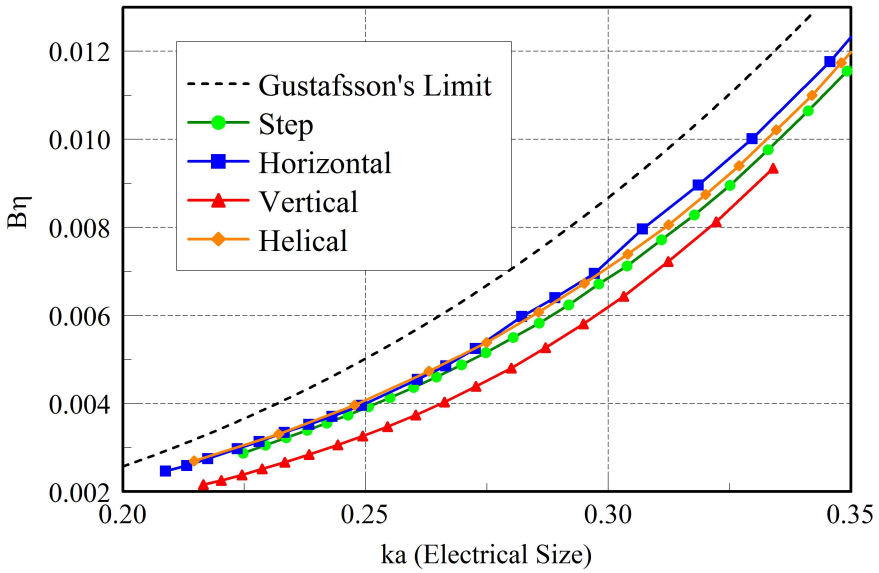

Figure 6.9: Bandwidth-Efficiency (Bη) vs. ka Compared to Gustafsson's Limit ($0.2 \leq ka \leq 0.35$)

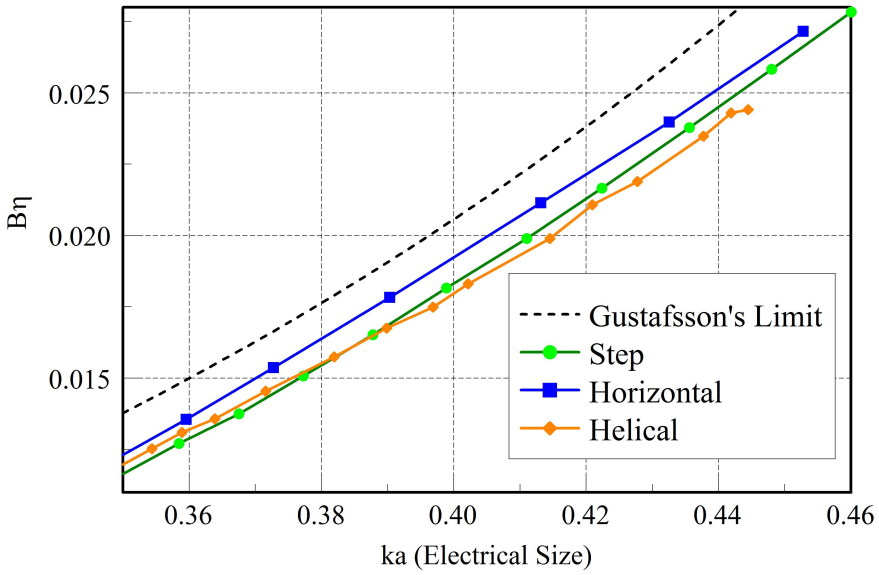

Figure 6.10: Bandwidth-Efficiency (Bη) vs. ka Compared to Gustafsson's Limit ($0.35 \leq ka \leq 0.46$)

which can be thought of as first-order versions of a horizontal meander pattern. Figure 6.11 represents the performance data of Figure 6.8 in a different manner; here the deviation or difference relative to Gustafsson's limit is plotted relative to the antenna's electrical size.

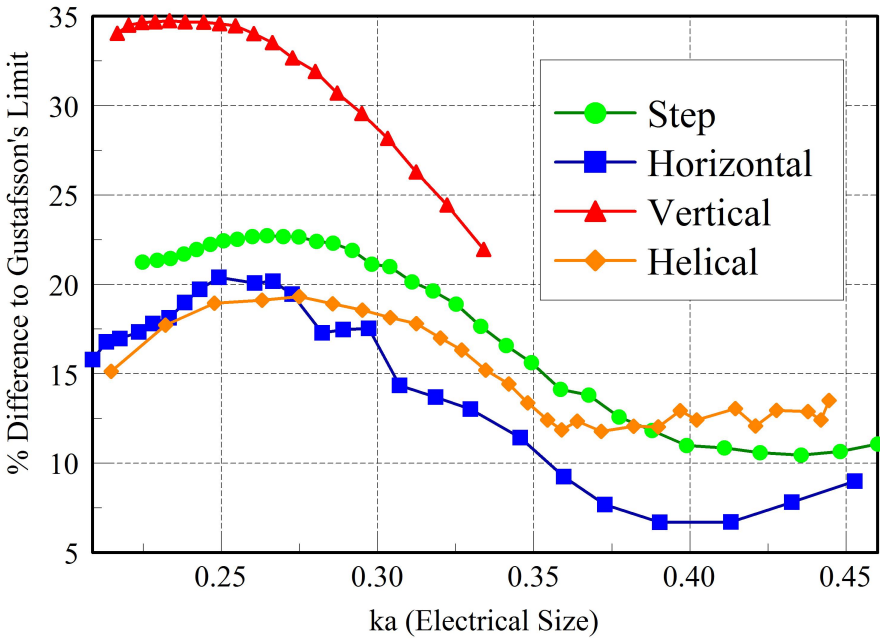

Figure 6.11: Percentage Difference Relative to Gustafsson's Limit vs. ka

Figure 6.11 shows a defined trend, that for small electrical sizes $ka < 0.35$ the difference increases and then peaks around $ka = 0.275$ and then decreases slightly. For the Horizontal, Helical and Step profiles; differences from the limit of below 13% are observed for $ka \geq 0.35$. The performance data in this format, clearly shows the performance edge that the Horizontal profile has over the other profiles. The Vertical profile has large percentage difference to Gustafsson's limit and this highlights that the vertical currents on the antenna are extremely significant.

There exist two distinct regions, low difference ($ka < 0.35$) and high difference ($ka > 0.35$) relative to Gustafsson's limit. In the low difference region the shorting profile angle is small ($\alpha < 90°$) while in the high difference region $\alpha > 90°$. Thus the performance degradation is strongly correlated with large value for the shorting profile angle. This phenomenon will be referred to as the "wrap-around effect," since large α's mean the shorting trace is wrapping around the antenna perimeter. Horizontal current elements on the shorting trace would have opposing elements and leading to a degradation of performance relative to potential.

6.1.1 Fabrication and Measurements

Antennas with the various meandered shorting profiles were fabricated by milling out the entire antenna structure from a copper sheet (16 oz) and then folding/bending each into the appropriate three-dimensional shape. Figure 6.12 shows a top view picture with a US quarter coin to show the relative feature size. Photographs of the Step, Horizontal, Vertical and Helical - DRLM antenna implementations are shown in Figures 6.13 and 6.14.

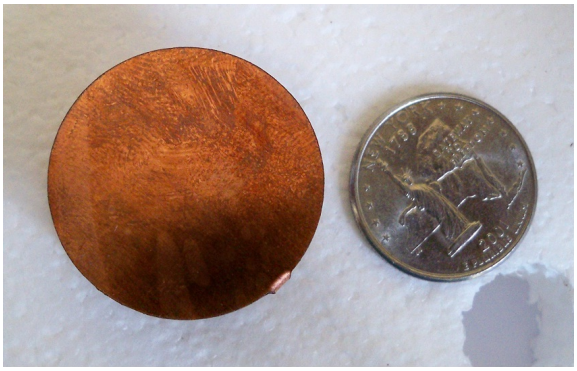

Figure 6.12: Antenna Top View

(a) Step

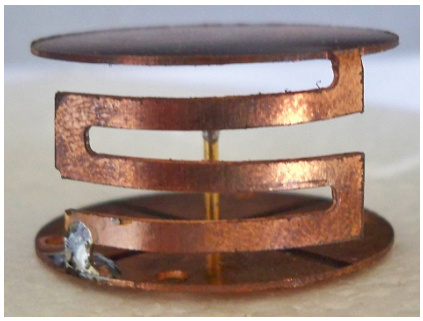

(b) Horizontal Meander

Figure 6.13: Fabricated Antenna Models (Step and Horizontal)

The measured data will be presented in two ranges of electrical sizes; this is done so as to make the presentation clear. The first range is designated as "moderately tuned" and it corresponds to antenna models with ka between 0.33 and 0.4, as shown in Figure 6.15.

(a) Vertical Meander (b) Helical

Figure 6.14: Fabricated Antenna Models (Vertical and Helical)

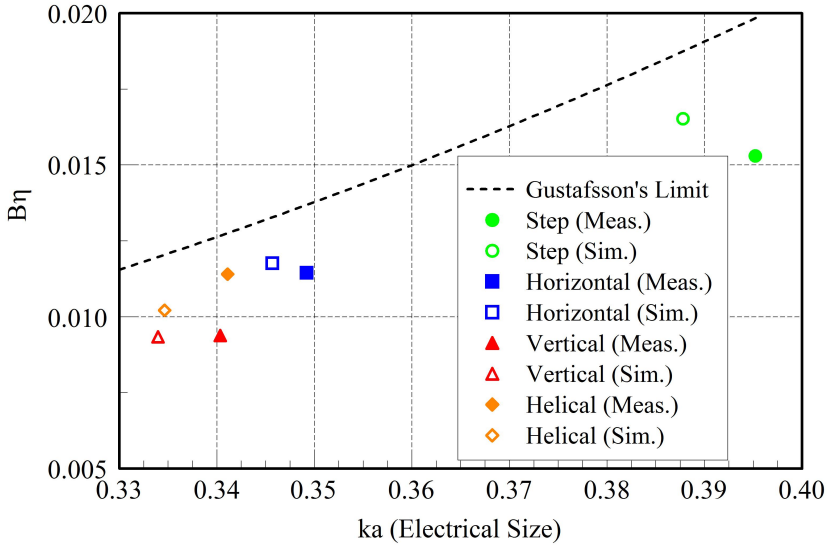

Figure 6.15: Measured and Simulated Performance for Moderately Tuned Antenna Models

There is generally good correlation between the measured and simulated models. The measured resonant frequencies were constantly larger than simulated by a small amount; this can be explained by slight fabrication imperfections (e.g., variation in patch or feed disk height). In Figure 6.16, the data comparison for the lower range designated as "more aggressive tuning" is shown. For this category, two DRLM antennas with the Horizontal profiles ($\alpha = 180°$ and $270°$) were constructed.

In this range, the fabricated antennas produced resonant frequencies that were lower than predicted by the simulation. Also, for the case with $\alpha = 180°$,

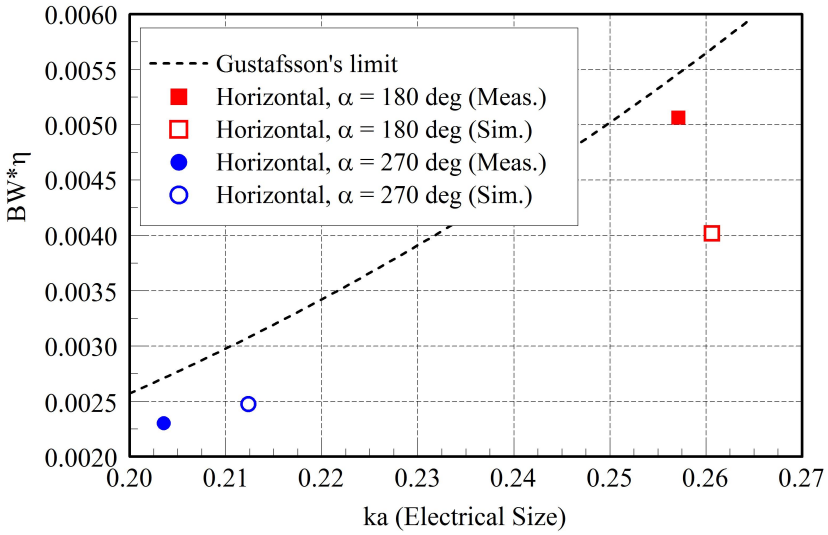

Figure 6.16: Measured and Simulated Performance for More Aggressively Tuned Antenna Models

the measured performance is much better than the simulated result. One important fact to remember is that as mentioned before the fabrication of these are more complicated to produce. Thus slight deviations from its ideal geometry are very hard to avoid. Figure 6.17 shows the reference coordinate system that will be used when describing the measured radiation patterns.

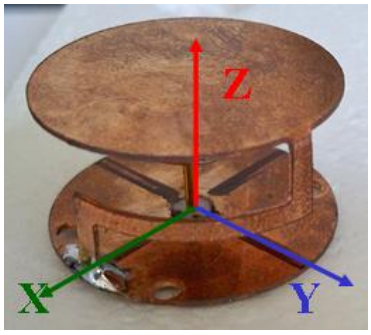

Figure 6.17: Reference Coordinate System

Radiation patterns for all the antenna models from Figures 6.13 and 6.14 are shown in Figure 6.18.

The measured radiation patterns show that this antenna radiates in a similar manner as the monopole antenna, with its characteristic null in the pattern normal to the ground plane. The radiation in the back half plane is large because the ground plane is only 0.75 λ_0 × 0.75 λ_0 in size.

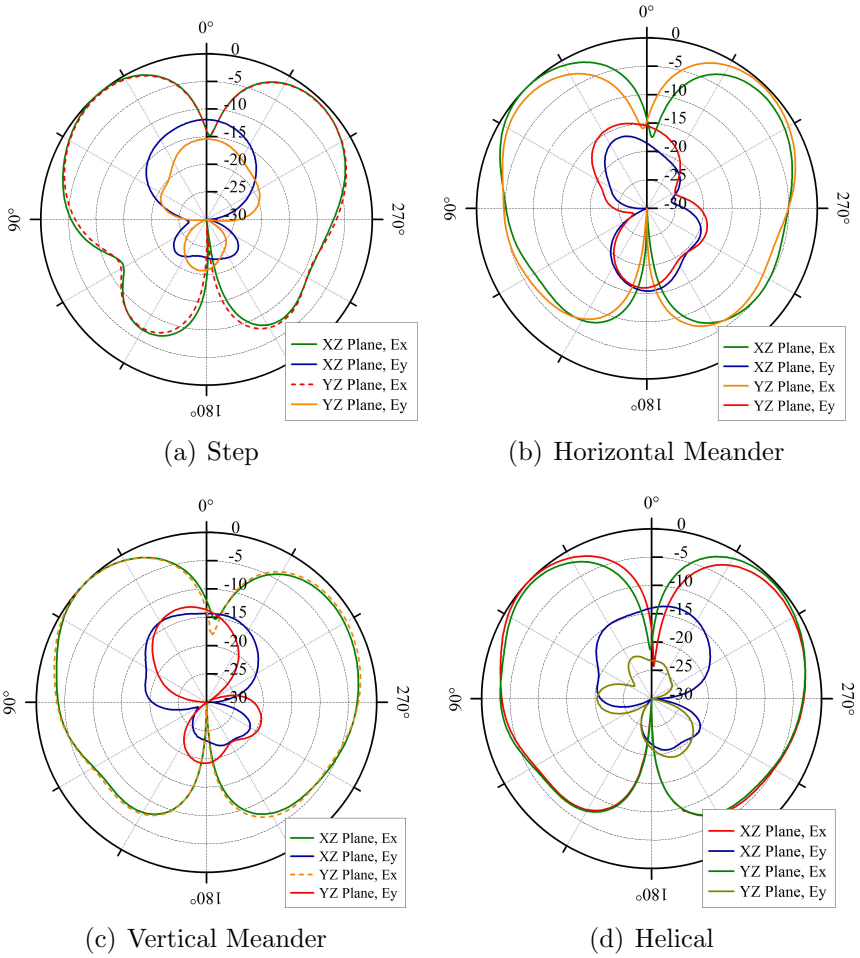

(a) Step (b) Horizontal Meander

(c) Vertical Meander (d) Helical

Figure 6.18: Radiation Patterns for Fabricated Antennas

In this section, we demonstrated an antenna capable of miniaturization with the constraint of a fixed volume by leveraging the PIFA design using meandered shorting profiles to increase the inductive loading effect. The best performing shorting profile styles were those based on achieving increased loading by meandering purely in the horizontal direction (e.g., Step, Horizontal and Helical).

6.2 Lumped Element Implementation

The shorting pin or strip can be modeled as a shunt inductor from the patch edge to the ground plane. As such, a logical question is: Can a lumped inductor be used as a substitute for the meandered shorting strip? How will the resulting performance be compared with the distributed implementation? In this section we explore the performance of the DRLM antenna where the inductive loading is applied using a lumped inductor.

Lumped inductors used in RF applications are known to have certain drawbacks, such as large physical size and conductive losses. An inductor with a high quality factor (Q-factor) is desired, since this implies low loss. Based on a search of RF magnetic component catalog from the manufacturer Coilcraft, inductors were chosen from the Midi Spring Air Core (MSAC) Inductors product line. These inductors boast high Q and current handling in the frequency range of interest. Figure 6.19 shows a photograph of these type of inductors. The package area for this inductor is roughly 5 x 6 mm with a height of 4.5 mm. Plots for inductance and Q versus frequency for the inductors are shown in Figures 6.20(a) and 6.20(b) respectively.

Figure 6.19: MSAC Inductor [48]

In particular, we chose to use the 22 nH inductor which has a peak Q-factor of 215 at 600 MHz, thus the Q is in excess of 200 for the frequency range of analysis (500 - 1000 MHz), see Figure 6.20. Also, the inductance remains

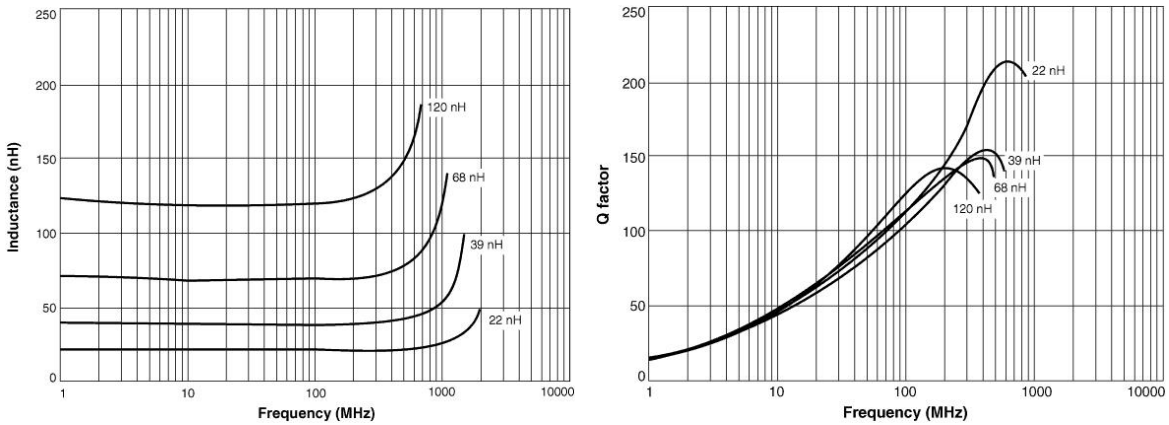

(a) Inductance vs. Frequency (b) Q vs. Frequency

Figure 6.20: MSAC Inductor Data [48]

fairly constant up to 1 GHz. It is useful to use the inductor in our full wave simulations in order to characterize its influence on the performance of the antenna for minor adjustments in application. At microwave frequencies the inductor is no longer accurately described by a single element but instead a more complicated circuit arrangement is required. Figure 6.21 shows the Coilcraft model derived from 2-port measurements. The model component values for the MSAC inductors are shown in Table 6.1.

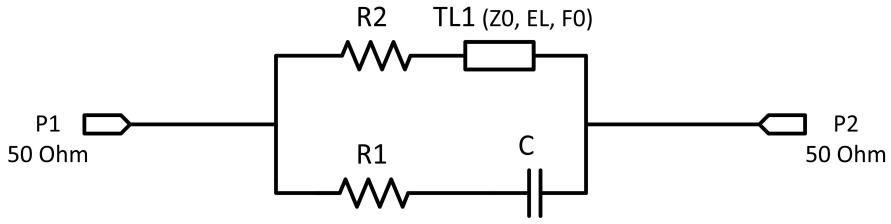

Figure 6.21: Coilcraft Transmission Line Model for the MSAC Inductors [49]

In order to implement this model in Ansoft HFSS, a first-order approximation of this circuit was derived, since the transmission line would be difficult to be applied to the antenna model. Thus the ideal transmission line is approximated using a fixed inductor with the value of 20 nH for the 22 nH MSAC inductor model. Figure 6.22 shows the corresponding lumped circuit model for the 22 nH MSAC inductor.

Table 6.1: Values for 22nH, 33nH, 47nH and 56nH Inductors

Parameter	22nH	33nH	47nH	56nH
R1 (Ω)	2.278	8.126	1.208	1.208
R2 (Ω)	0.1502	0.2307	0.3135	0.4015
C (pF)	0.1721	0.1754	0.2342	0.2312
TL1:Z0 (Ω)	209	245.2	307.5	366.1
TL1: EL (deg)	45.12	65.8	63.68	63.68
TL1:F0 (MHz)	1198	1370	1177	1177

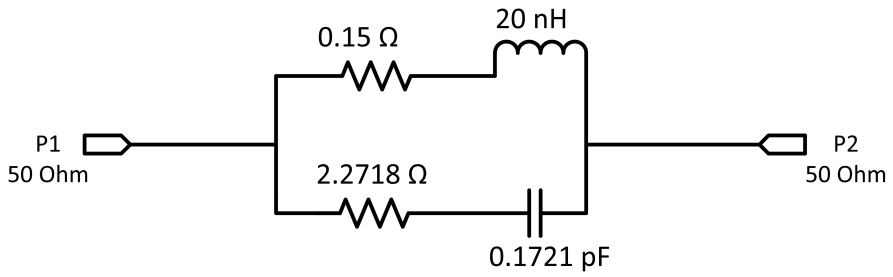

Figure 6.22: Lumped Circuit Model for the MSAC 22nH Inductor

The transmission line model in Figure 6.21 is directly derived from measurement data and thus S-parameter data from this model will be referred to as the measured S-parameters. The S-parameters extracted from the lumped circuit model will be referred to as the circuit model S-parameters. The circuit model and measured S-parameters are compared in Figure 6.23. Note that this comparison is limited to frequencies below 1 GHz and features the magnitude responses of the reflection (S_{11}) and transmission (S_{21}) coefficients. For the frequency range shown the correlation in magnitude responses is very good. Thus the circuit model from Figure 6.22 is used in the full wave solver as lumped RLC boundary elements in order to accurately represent the effect of the 22 nH MSAC inductor at microwave frequencies.

Given the small inductor package size relative to the antenna height it stands to reason that the placement of the inductive load would affect the antenna performance. The effect of inductive load placement has been studied on electrically small monopole antennas in order to determine the tradeoffs related to radiation efficiency and impedance matching capabilities [50]. Based on work by Hansen [50], it is shown that an improvement in radiation resistance of up to four times over the unloaded case can be achieved as

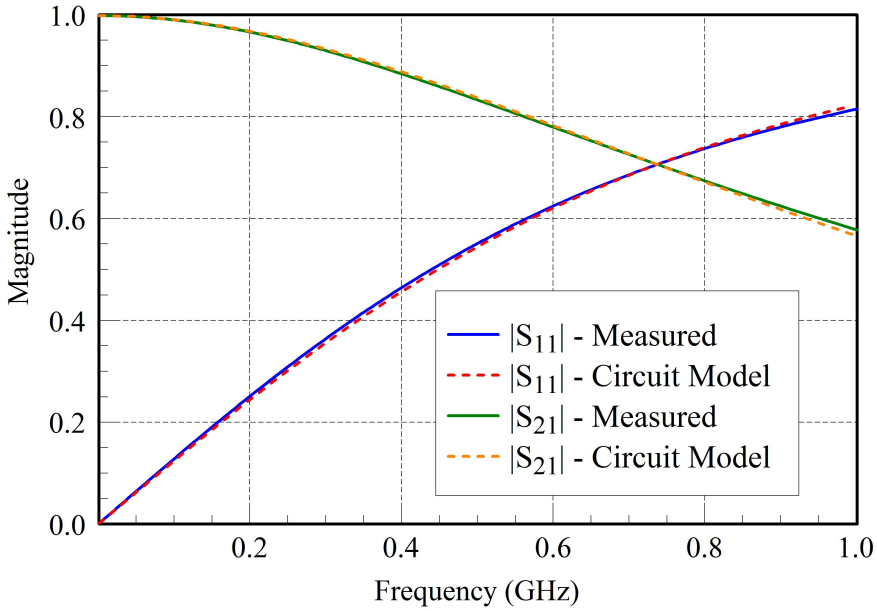

Figure 6.23: S_{11} and S_{21} Magnitude for the Transmission Line Model Supplied by Coilcraft Compared with a Circuit Model for the MSAC 22 nH Inductor

the inductive load is moved away from the feed point (or current maximum) and toward the monopole ends (or current minimum). The efficiency, on the other hand, is shown to peak when the load point is at about 40% of the monopole length from the feed point (or current maximum).

We will restrict placement of the lumped inductor to the vertical shorting strip, somewhere between the ground plane and the patch. The performance will be determined as a function of position. Both full wave simulation using the circuit model for the lumped inductor and measurements from fabricated units will be performed. The performance for three specific positions will be evaluated which are designated as the top, middle and bottom. The top position has the one terminal of inductor fixed to the patch and the other attached to a vertically aligned shorting strip. For the middle position the inductor is placed in the center between the patch and the ground plane. And finally, the bottom has the inductor fixed to the ground plane and the strip. Figure 6.24 shows the fabricated Lumped Inductor - DRLM Antenna in the specific positions of Top, Middle and Bottom. For this experiment the patch height and radius are equal to 1.5 cm, thus the antenna volume is equivalent to the distributed implementation in Section 6.1.

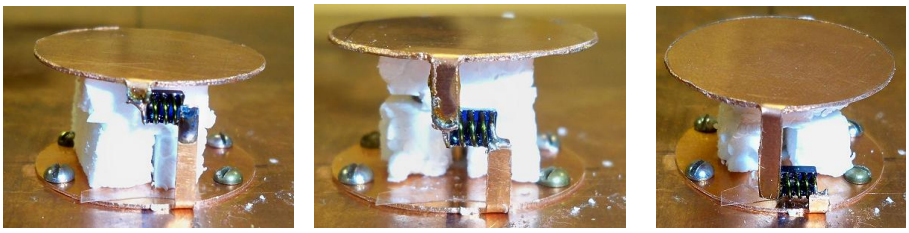

(a) Top (b) Middle (c) Bottom

Figure 6.24: Fabricated DRLM Antenna with Lumped Inductor in the Top, Middle and Bottom Positions

The bandwidth-efficiency product versus electrical size for the simulated and measured antennas is shown in Figure 6.25. This plot shows that in both simulation and measurement there is a defined trend in the performance relative to its position. There is a gradual degradation in performance as the lumped inductor is moved down the vertical shorting strip. This result is expected since the current distribution is a maximum at the base of the shorting strip and gradually decreases toward the patch. Higher currents result in larger conductive losses and thats why the top position is the best performing one.

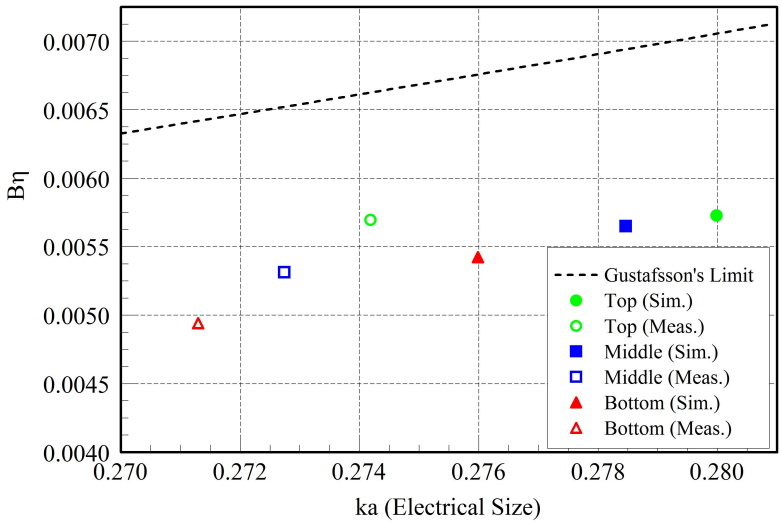

Figure 6.25: Simulated and Measured Data for DRLM Antenna with Lumped Inductor Model vs. Position

The specific bandwidth, resonant frequency, radiation efficiency and difference relative to Gustafsson's limit is shown in Table 6.2 for simulated antenna and in Table 6.3 for the measured case.

Table 6.2: Simulated Data for Lumped Inductor - DRLM Antenna

Position	f_r(MHz)	%BW	η(%)	Difference/Gustafsson (%)
Top	630.2	0.74	77.86	18.81
Middle	626.8	0.73	77.44	18.59
Bottom	621.2	0.71	76.37	19.72

Table 6.3: Measured Data for Lumped Inductor - DRLM Antenna

Position	f_r(MHz)	%BW	η(%)	Difference/Gustafsson (%)
Top	617.1	0.74	77.3	14
Middle	614	0.72	74.2	18.5
Bottom	610.6	0.71	71	23

The measured results for the lumped inductor - DRLM Antenna show good correlation between simulation obtained using a simplified circuit model. The fabricated antenna operates at a lower resonant frequency than in simulation, most likely due to structural difference during fabrication. Additionally, the slope of data points for Top, Middle and Bottom is much sharper than the corresponding simulation data due to the rapid decrease in radiation efficiency. The measured result shows a low difference to Gustaffson's limit (14%).

In Figure 6.26 we compare the result obtained for the lumped inductor - DRLM and the distributed line - DRLM antennas (i.e., Step, Horizontal, Vertical and Helical DRLM Antennas). The simulated results for the lumped case agree very well with distributed line implementations. However, the result for the measured lumped inductor - DRLM antenna show an outperformance over the distributed line - DRLM antenna as highlighted by the data point clearly above the other data traces and in close proximity to Gustafsson's limit. This result would have us believe that the lumped inductor implementation would yield a better performing antenna. It should be remembered that the electrical size of the antennas we are comparing is in the

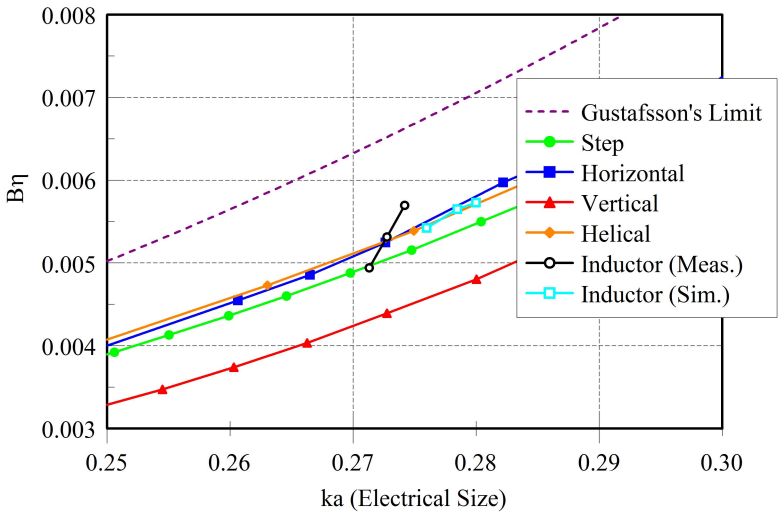

Figure 6.26: Lumped Inductor - DRLM vs. Distributed Line - DRLM

region where the distributed line - DRLM experience performance degradation (in fact, it is roughly at its peak difference to Gustafsson's limit) due to the wrap-around effect discussed in Section 6.1. Thus since this effect is not present for the lumped element implementation an antenna with improved performance can be achieved using lumped loading for small electrically sized antennas.

The radiation pattern for the fabricated antenna with the lumped inductor in the Top position is shown in Figure 6.27. The radiation pattern features two cut planes (refer to Figure 6.17 for reference) XZ and YZ. Both polarizations, co- and cross-polarizations are shown. Note the patterns are taken at the operating frequency (i.e., minimum reflection coefficient).

The radiation patterns are very similar to those with the inductive loading implemented with distributed elements (i.e., Step, Horizontal, Vertical and Helical profiles) and indicate the characteristic pattern of a monopole-type antenna on a finite ground plane. The cross-polarization level is a little higher than with distributed elements but overall the cross-polarization levels are similar to PIFA antennas which are used in applications where this is not that important. Even though there is a substantial difference between the measured and simulated data, the trends in the data are the same. The main takeaway is that the lumped inductor is a viable candidate for induc-

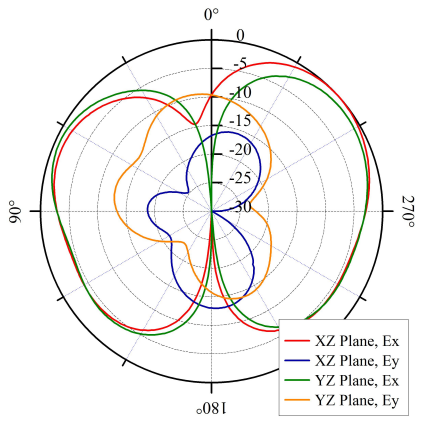

Figure 6.27: Measured Radiation Pattern for DRLM Antenna with Lumped Inductor in Top Position

tive loading for the antenna. For the best performance-size tradeoff the Top position should be chosen.

The tuning ability and performance of the lumped inductor implementation of the DRLM Antenna with different inductor values is observed in Figure 6.28. Note that all inductors are MSAC inductors. The inductor values to be used are the 22 nH, 33 nH, 47 nH and 56 nH and they are used in the Top position. Also the cylindrical volume is slightly different for this experiment. The patch height is 1.8 cm and radius is 1 cm. This is done so that antenna after loading is still in the frequency range of interest (i.e., if these inductor values were applied to the original antenna size then the resonant frequency would be lower and consequently the bandwidth too narrow).

A hybrid approach is investigated, where the distributed and the lumped model are used together to improve the performance of the distributed model by diminishing the wrap-around effect. The particular hybrid configuration we will explore features the Step-DRLM with a "ideal" lumped inductor element in the top position. The shorting profile angle is kept static ($\alpha = 90°$) while the variable loading is achieved by changing the inductance for the lumped component. Figure 6.29 shows the percentage difference to Gustafsson's limit comparison between the distributed-only (Step-DRLM) and the hybrid configuration (distributed and lumped) antennas. The hybrid configuration data is for inductance values between 1 nH to 30 nH. As the figure shows, the difference to Gustafsson's limit is decreased for moderate levels

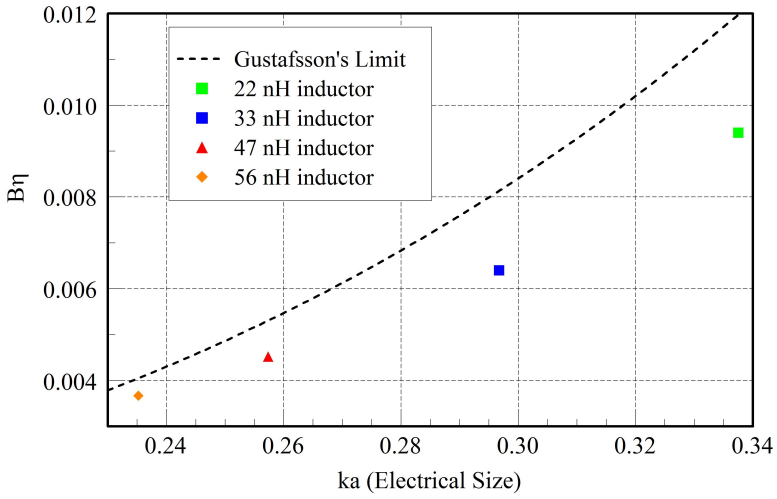

Figure 6.28: Measured Performance for Lumped Inductor- DRLM Antenna with Variation in Inductance

of loading. As the inductance increases further the difference to Gustafsson essentially trends to the curve traced out by the distributed-only case.

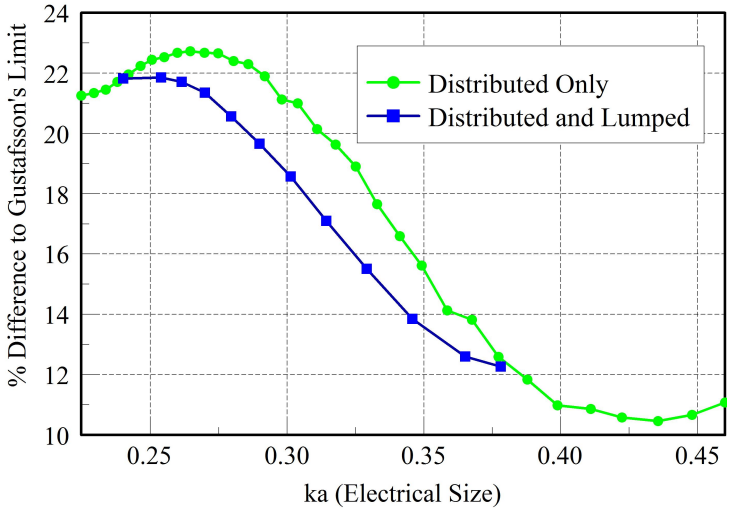

Figure 6.29: Hybrid Configuration Data for Lumped Inductor and Step - DRLM

In this section, we demonstrated the viability of inductive loading antennas using lumped inductors. These devices have always been assumed to be too lossy for microwave applications but they were found to be comparable to their distributed counterparts. In fact, measurements indicate that the lumped inductor loading antenna yields better performance for low ka an-

tennas. We also identified the optimum position for a lumped inductor with small footprint (i.e., Top position, connected to the patch). In simulation we showed that the antennas configured with distributed line loading can see a performance improvement if moderate levels of lumped inductive loading are used in conjunction. This performance improvement is related to absence of the wrap-around effect in the hybrid configuration (i.e., small shorting profile angles, $\alpha \leq 90°$).

6.3 Analysis of Low-Profile Tradeoffs

A decrease in the antenna height results in a severe degradation of performance as given by bandwidth and efficiency. The radiation efficiency is directly related to the radiation resistance which in turn is proportional to the vertical height of a monopole type antenna. The reduction in bandwidth can best be understood by deriving an equivalent lumped circuit model and examining the effects of a height contraction on the circuit's performance.

When evaluating the tradeoffs associated with a height reduction for this antenna it is insightful to use a simplified lumped circuit model to better understand the dynamics at play. The fundamental or lowest resonant mode is dominated by a parallel resonance and consequently can be modeled by a parallel RLC circuit. The elements of this parallel RLC circuit are associated with the geometric features of this structure. The shunt capacitance (C) is derived from the parallel plate effect between the circular patch and the ground plane. The meandered shorting strip represents the shunt inductance (L) and finally the associated radiation resistance (R) can be seen as a shunt resistance. Figure 6.30 shows the Step profile antenna model annotated with parallel RLC component labels and the associated geometrical features that manifest these component effects.

A parallel RLC circuit is described by its resonant frequency and its quality factor (or simply Q), where the parallel resonant frequency f_0 is defined as

$$f_0 = \frac{1}{2\pi\sqrt{LC}} \tag{6.1}$$

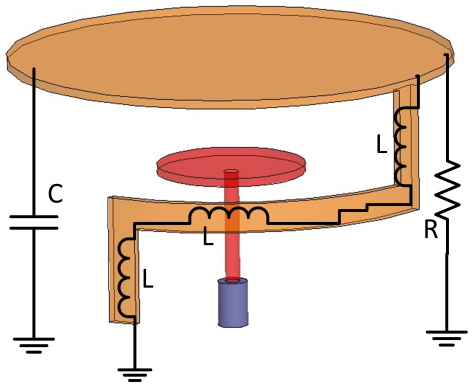

Figure 6.30: Antenna Model with Step Profile Shorting Strip and Parallel RLC Components

while the Q_p is

$$\begin{aligned} Q_p &= R/(\omega_0 L) \\ &= \omega_0 RC \end{aligned} \tag{6.2}$$

where $\omega_0 = 2\pi f_0$. The shunt inductor L is derived from the relatively thin strip to ground, thus a reduction in antenna height would lead to a shorter shorting strip length and consequently the inductance would decrease. The shunt capacitance is determined to be due to parallel plate effect between the ground and the monopole top load. The equation for the capacitance between two metal plates is given as

$$C = \frac{\epsilon A}{d} \tag{6.3}$$

where ϵ is the dielectric permittivity of the medium between the metal plates, A is the plate cross-sectional area and d is the distance between the metal plates. So, as the antenna height is reduced, the distance between the monopole top plate and the ground plane decreases and the effective shunt capacitance increases. To summarize, a decrease in antenna height will have the effect to increase the shunt capacitance and decrease the shunt inductance for the simplified circuit model. This has the effect to alter both the resonant frequency as well as the quality factor. The net effect is less dramatic for the resonant frequency since the inductive and capacitive effects counter one another. But for the Q, the result is clear, if we neglect the resistor R we can deduce an increasing C and decreasing L both have the effect of increasing the Q as given by Equation 6.2.

An alternative expression for the capacitance can be written in terms of the volume, where the volume (V) of a cylinder is

$$V = Ad = \pi r^2 d \tag{6.4}$$

since the cross-sectional area of the cylinder is given by the product of π and the square of the cylinder radius r. The capacitance C is thus

$$C = \frac{\epsilon V}{d^2} \tag{6.5}$$

Two antenna designs with the same volume and different heights (i.e., $d_1 \neq d_2$) will have capacitance expressions as given by

$$C_1 = \frac{\epsilon V}{d_1^2} \tag{6.6}$$

$$C_2 = \frac{\epsilon V}{d_2^2} \tag{6.7}$$

and we define $x = d_2/d_1$ as the height reduction factor, where $d_1 \geq d_2$ and thus $0 < x \leq 1$. The ratio of capacitances for design 2 and 1 is

$$\frac{C_2}{C_1} = \frac{d_1^2}{d_2^2} = \frac{1}{x^2} \tag{6.8}$$

Since $x \leq 1$, the effect of a decrease of the antenna height d is a increase in capacitance by a factor to the second power of the height reduction factor. For example, a design where the height is halved ($x = 1/2$) will yield a fourfold capacitance increase ($C_2 = 4C_1$). Thus the Q will increase (or bandwidth decrease) dramatically with a height reduction.

In the case of volume rebalancing we desire a lower profile antenna but now we compensate the height reduction by increasing the radius so that the antenna volume remains constant. In this scenario, the capacitance increases on two counts, because the patch area increases and the distance between the plates decreases. The short-fat geometry (i.e., low height and large patch area) would result in an even larger antenna Q versus just a simple height reduction.

6.3.1 Patch Height Variation Study

The patch height is adjusted and performance is recorded and the relative difference to Gustafsson's limit is plotted in Figure 6.31 for the Step- and Helical-DRLM Antennas. The other two profiles (Horizontal and Vertical) are not considered for this study since they are not suited for height reduction scenarios. The Vertical profile trends to the Step profile for small patch height, while the Horizontal profile would require narrower gaps between horizontal sections, narrower strip widths or less meander loops, all of which would be detrimental to performance. As shown, the relative performance is similar for the Step and Helical profiles. The relative performance deviation is large for low height profiles while small deviations characterize antennas with aspect ratios closer to unity. The internal performance metrics for the Step ($\alpha = 90°$) and the Helical (Pitch = 3.77 cm) Profiles are shown in Tables 6.4 and 6.5.

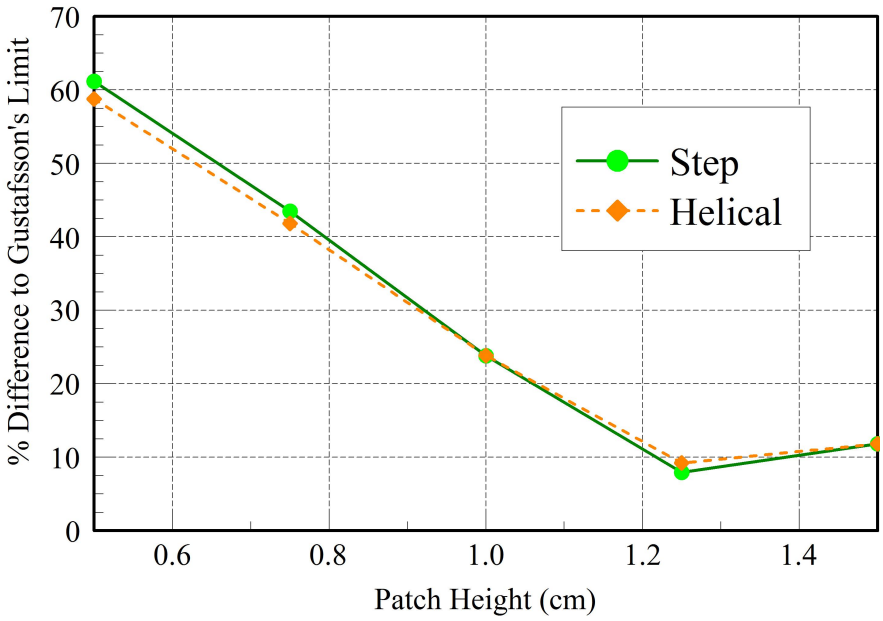

Figure 6.31: Performance Differences Relative to the Gustafsson Limit for Step and Helical Profiles at Various Aspect Ratios

Table 6.4 shows that the resonant frequency increases as the patch height is decreased. The antenna geometry forces a $\lambda/4$ current distribution from the base of the shorting strip to the far end of the patch. By lowering the patch, the quarter wavelength distance is shortened and consequently the

Table 6.4: Step ($\alpha = 90°$) Profile Performance Data for Patch Height Variation

Patch Height (cm)	f_r(MHz)	%BW	η(%)	Difference/Gustafsson (%)
1.5	872.8	1.7	97.14	11.83
1.25	916.7	1.51	96.63	7.92
1	964.7	1.3	95.43	23.78
0.75	1001.9	0.95	92.62	43.47
0.5	1072	0.7	86.28	61.16

resonant frequency is increased. Notice this decrease in height affects the Step profile much less than the Helical profile (see Table 6.5). This makes sense since for the Step the horizontal section is unaffected by the height reduction while for the Helical profile the height decrease shortens the helical shorting strip significantly. Thus the antenna with helical profile experiences almost a 100% increase in resonant frequency for a 67% reduction in height.

Table 6.5: Helical (Pitch = 3.77 cm) Profile Performance Data for Patch Height Variation

Patch Height (cm)	f_r(MHz)	%BW	η(%)	Difference/Gustafsson (%)
1.5	878.7	1.74	97.01	11.84
1.25	966.8	1.74	97.03	9.2
1	1077.4	1.76	97.39	23.85
0.75	1207.8	1.62	97.34	41.83
0.5	1418.6	1.52	97.98	58.76

The bandwidth and efficiency for the Helical-DRLM antenna remains essentially constant for height variations, but its operating frequency increases substantially. As the patch height is decreased the Helical-DRLM Antenna approaches the traditional Circular PIFA which resonates when its circumference is $\approx \lambda/2$ or roughly 1.6 GHz for patch radius equal to 1.5 cm. The Step-DRLM antenna exhibits significant degradation in bandwidth and efficiency with a decrease in patch height. The Step-DRLM geometry supports currents that are aligned parallel to the ground plane, this is the source of performance degradation. In electromagnetic theory we can remove large conductive surface using image theory and add image currents to maintain the equivalent situation. For currents that are parallel to the conductive

surface, the image currents are placed an equal distance from ground plane (now removed) and in the opposite direction, see Figure 6.32.

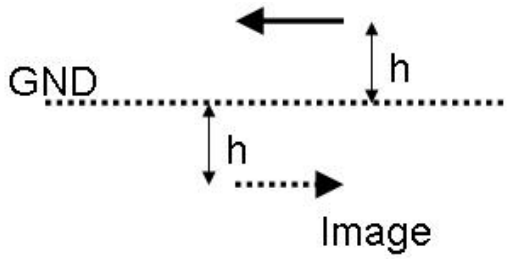

Figure 6.32: Image Theory for Parallel Currents

The fields generated by the surface currents on the antenna (specifically on the horizontal arm of the Step profile) will tend to act destructively with the fields generated by the image currents because the currents flow in opposite directions. This phenomenon will get worse as the current elements get closer to the ground plane which occurs when the patch height is decreased. The destructive superposition of the radiated field yields a lower radiation efficiency while the bandwidth decrease has been explained earlier by the resulting increase in antenna Q. An alternative interpretation of the data for the Step-DRLM Antenna can be shown using characteristic mode theory, see Figure 6.33 which depicts the characteristic angle for mode 1 for various patch heights.

As shown, for decreasing patch height the resonant frequency increases as given by the $\alpha_1 = 180°$ intercept. Also, the bandwidth becomes narrower as the height decreases as given by the relative increase in slope of the characteristic angle curve through the resonance point. It was noted earlier that a volumetric rebalancing, where the patch area is increased to compensate for the height reduction and so doing keeping the volume constant, would result in an even larger Q (or narrower bandwidth). Table 6.6 shows performance data for a volume rebalancing study. Note that for this study the volume was kept constant and equal to the original design (i.e., patch height = patch radius = 1.5 cm). Also, the shorting profile angle was normalized to maintain approximately the same length.

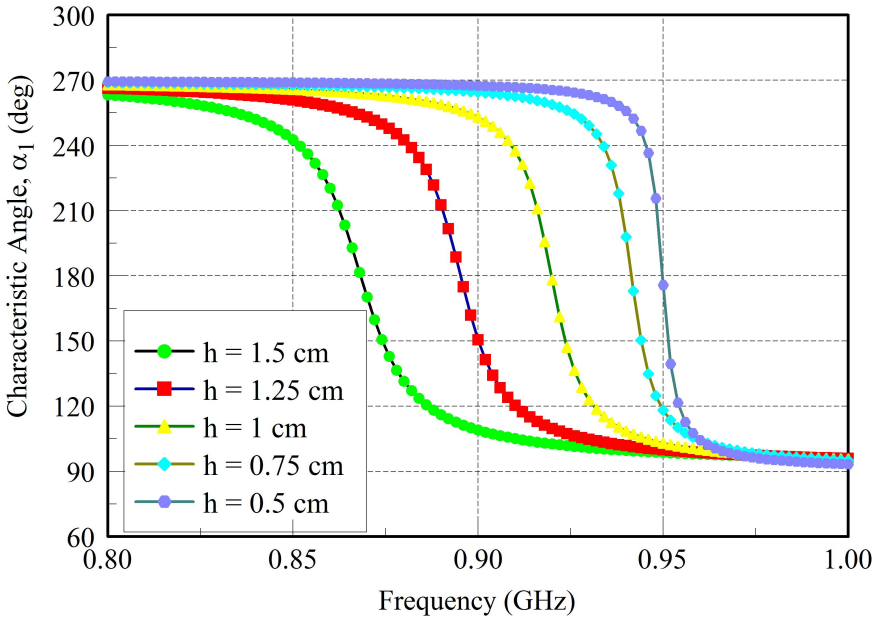

Figure 6.33: Characteristic Angles for the Step-DRLM ($\alpha = 90°$) for Different Patch Heights

Table 6.6: Step Profile ($\alpha = 90°$) Data for Volumetric Rebalancing

Patch Height, Radius (cm)	f_r(MHz)	%BW	η(%)	Difference/Gustafsson (%)
1.5, 1.5	872.8	1.7	97.14	11.83
1, 1.837	840.1	1.15	94.55	38.19
0.75, 2.121	780.3	0.77	89.85	60.38
0.5, 2.598	698.3	0.51	77.68	78.35

As shown, the short-fat topology is not well suited for this antenna as evident by the large difference in performance relative to the Gustafsson limit. This antenna structure has the characteristics of a monopole antenna and as such any contraction of the element in the vertical dimension will cause significant degradation in performance.

6.3.2 Step Profile - Gap Variation Study

The increase of shorting strip length with the constraint of limited volume, forces the structure to achieve the length extension by having long horizontal sections parallel to the ground plane. Up to now the Step profile has been constructed with the horizontal arm placed at the geometric center between

the ground plane and patch. In this section we explore the performance behavior for a variation in the gap between the ground plane and the horizontal arm height. Figure 6.34 depicts the experiment pictorially. The Gap dimension is varied with the patch height held constant.

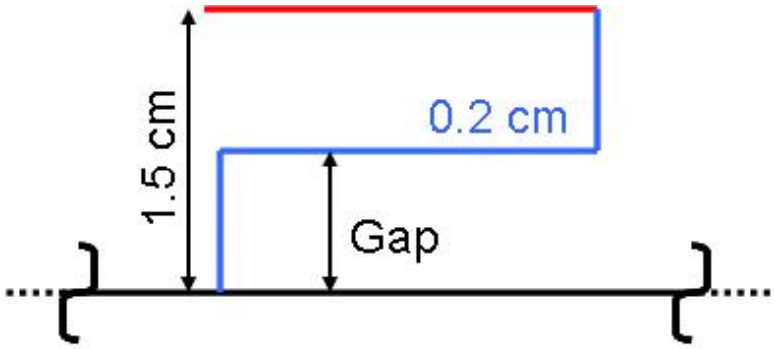

Figure 6.34: Step Profile Geometry Showing the Gap Length

Figure 6.35 shows the performance of the Step-DRLM Antenna with Gap variations and how it compares to the fundamental limit as predicted by Gustafsson for cylindrical volumes. The internal performance metrics are shown in Table 6.7.

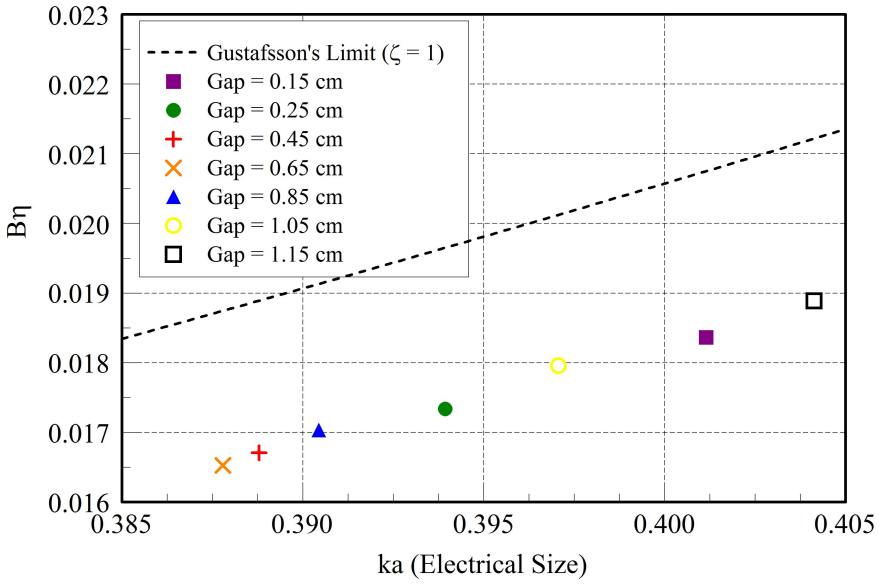

Figure 6.35: Step Profile ($\alpha = 90°$) with Various Gap Lengths

It is interesting to observe that resonant frequency is lowest for the step horizontal arm in the center, while the resonant frequency increases when the arm diverges from this position (either up toward the patch or down to the ground plane). It is possible that as the gap between the horizontal arm and the ground plane (or the patch) gets small the coupling increases and effectively shorten the trace length electrically and thus the resonant frequency increases. The radiation efficiency remains essentially the same for all gap dimensions, this is noticeably different from the case where the patch height is changed. This is due to the fact the shorting trace length remains the same for the gap variation study while it is shortened notably for the patch height study. The bandwidth does change as the gap dimension is altered, smaller bandwidths are observed with the step horizontal arm at the center while larger bandwidths are exhibited with the horizontal arm closer the ground plane or patch.

Table 6.7: Step Profile ($\alpha = 90°$) Data for Gap Variation

Gap (cm)	f_r(MHz)	%BW	η(%)	Difference/Gustafsson (%)
0.15	902.9	1.89	96.96	11.5
0.25	886.7	1.79	97.05	11.76
0.45	875.1	1.72	97.05	11.55
0.65	872.8	1.7	97.14	11.83
0.85	878.8	1.75	97.16	10.97
1.05	893.7	1.85	97.21	10.76
1.15	909.6	1.95	97	10.97

In this section, we developed a theory of understanding for the performance degradation found in planar-type antennas using a simplified circuit model for the antenna. Both height reduction and volume rebalancing cases were analyzed and the antenna structure was found not suitable for the short-fat topology. Finally, the gap variation study examined the effect of off-center placement of the horizontal section for the Step profile. We conclude that a coupling mechanism causes the effective shortening of the trace length when the horizontal section is close to the ground plane or the patch. This phenomenon points to the reason as to why the Horizontal profile's trace is so much longer for a given electrical size.

6.4 Bandwidth Improvement

The DRLM antenna has good range of tunability but the impedance bandwidth is extremely narrow, on the order of 1.7% (VSWR = 2) for moderate levels of inductive loading (i.e., $\alpha = 90°$ or pitch = 3.77 cm). In this section, a method for improving the impedance bandwidth is presented. The method involves using the DRLM in a stacked or nested arrangement, all while still maintaining the fixed volume constraint (i.e., the antenna volume is fixed and is equal to the single DRLM antenna from earlier sections). Stacked arrangements of PIFA elements have been employed in order to increase the bandwidth of the PIFA antenna [51]. The concept is to have a structure that is capable of supporting two closely spaced resonant modes and thus doubling the bandwidth compared to the single resonant mode case.

The stacked Step-DRLM Antenna is shown in Figure 6.36. Both the top and bottom Step-DRLM antennas have identical shorting profile angles and are shown with $\alpha = 90°$. The top element has a patch height and radius equal to 1.5 cm (same as earlier section on individual Step-DRLM Antenna). The bottom element has a patch height equal to 0.4 cm. The patch radius is set to 1.35 cm, so as to avoid contact with the top element's shorting strip. Notice, in this topology the bottom antenna element is probe-fed directly. The distance between the two patch heights is designated as d.

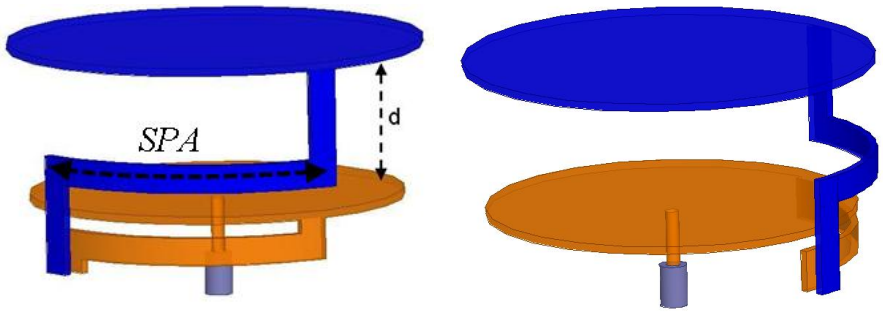

(a) Front View (b) Side View

Figure 6.36: Stacked Step-DRLM Antenna

The stacked arrangement can be viewed as two closely coupled single Step-DRLM Antennas. The lowest resonant mode is essentially derived from the

top element and the second mode from the bottom element. There is however strong coupling and interaction between these modes and as such they cannot simply be controlled independent of one another. Therefore it is best to have essentially (or close to) the same patch radius and shorting profile angles for both the top and bottom elements. In order to promote the smallest antenna (electrically), the patch radius should as large as the volume will allow. The maximum shorting profile angle is limited by how close the individual modes can be brought together, since the larger α will result in smaller individual mode bandwidths and thus the modes would have to be brought ever closer in order to realize a larger overall bandwidth. The closeness of the individual modes is controlled by the separation distance d between the top and bottom patches. The dimension d controls the amount of coupling between the structures, a larger d would yield less coupling. Larger d is desired in order to increase the bandwidth by combining the two lowest order modes. How large we can make d depends on the minimum patch height for the bottom element and the maximum allowable patch height for the top element. Figure 6.37 shows the plots for the characteristic angles (α_1, α_2) for various separation distances (d).

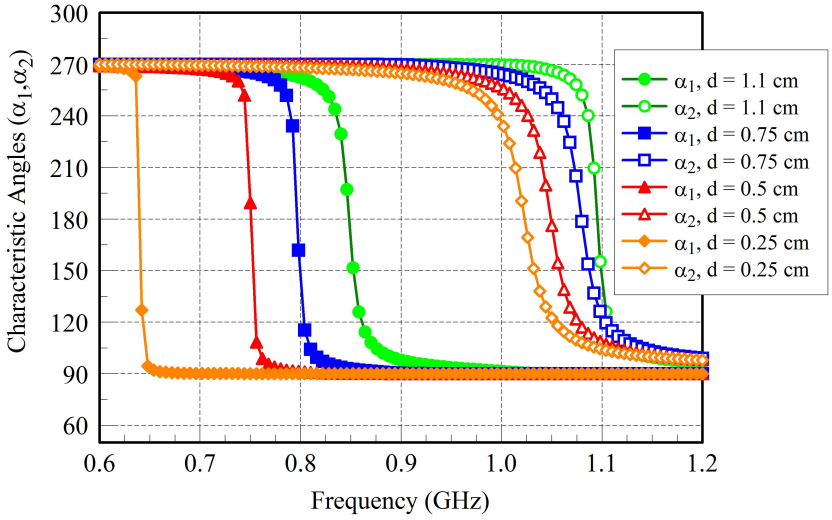

Figure 6.37: Characteristic Angles for Variation of Parameter, d

Modes 1 and 2 for each case of increasing d have ever closer resonant frequencies to one another. Specifically, the lower resonant mode (mode 1) is substantially affected by variation of d. Next, it is shown what the effect of

the changes to the α is on the characteristic behavior of the Stacked Step-DRLM. Note that the shorting profile angle's for both the top and bottom structures are changed in lock step. Figure 6.38 shows the plot for the characteristic angles for a Stacked Step-DRLM Antenna with shorting profile angles (or SPAs) of 60°, 90° and 120°. The resonant mode frequencies move down with increase inductive loading. Additionally, there is some tightening in the separation of mode 1 and 2 characteristic responses.

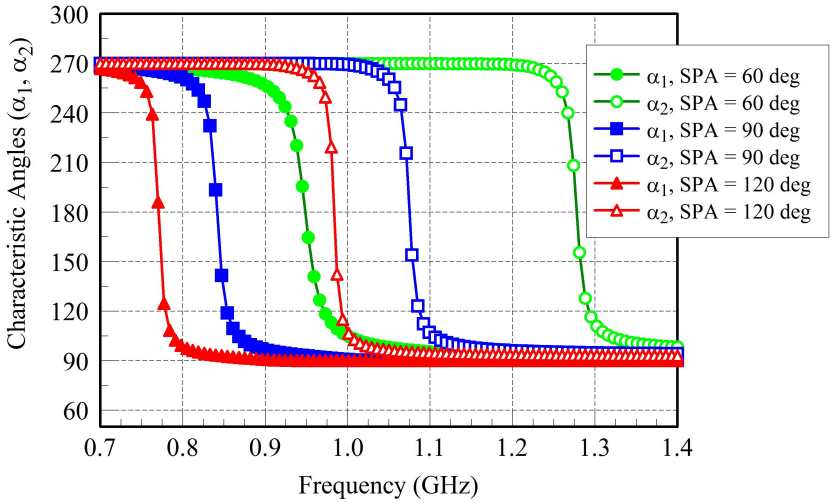

Figure 6.38: Characteristic Angles for Variation of Parameter, *SPA*

Given the understanding obtained from a characteristic mode study, a design is completed with the separation distance $d = 1.1$ cm and both SPAs equal to 90°. The Stacked Step-DRLM Antenna is simulated in the full wave solver HFSS by Ansoft. Figure 6.39 shows the impedance data in Smith chart format. This format is extremely useful in visualizing the matching network that would be appropriate for achieving a good match to 50 Ω.

The knot-like pattern on the Smith chart indicates a multi-mode resonance. The multi-mode resonance translates to larger impedance bandwidth. A conventional stub matching technique is employed in order to achieve a good match and minimize reflections from the antenna. The matching network features a series line from the antenna port to the feed and a shorted TL stub is placed in parallel with the feed port. The series transmission line is designed on a microstrip substrate to be 50 Ω, so that the input impedance trace will follow the locus of points of a constant VSWR circle

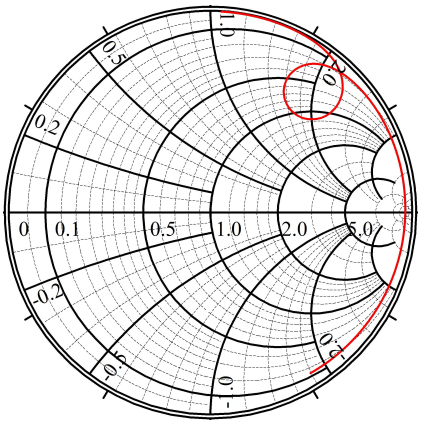

Figure 6.39: Input Impedance for the Stacked Step-DRLM Antenna

for changes in the line length. The series line is made long enough so that the knot in the impedance response now lies around points on the constant conductance circle. The final step is to add a short-circuited stub line. The short-circuited stub line is less than $\lambda/4$ and thus realizes a shunt inductance. This shunt inductance allows movement of the impedance trace up along line of constant conductance until it is centered around the Smith chart center point (i.e., sits inside the VSWR = 2 circle). The line is designed for Rogers Duroid 6006 substrate, which has a dielectric constant $\epsilon_r = 6.15$, loss tangent $\tan\delta = 0.0019$ and thickness $h = 0.635$ mm. Using Agilent's ADS simulation tool the microstrip matching network is designed as a series TL with width = 2.4 mm and length = 40.5 mm, the stub parameters are for width = 2.4 mm and length 9.5 mm. This matching network is implemented in HFSS in curved geometry so as to remain enclosed by the circumscribing cylindrical volume, the layout for the matching network is shown in Figure 6.40. The complete design (antenna with matching circuit) is shown in Figure 6.41.

The magnitude response of the reflection coefficient for the antenna with matching network is shown in Figure 6.42. The impedance bandwidth (VSWR = 2) is 4.8%, this represents a more than doubling over the single-mode Step-DRLM bandwidth performance. The simulated radiation efficiency is 91.8% and its size or $ka = 0.411$. The Stacked version has a bandwidth-efficiency product of 4.42%. The limits for this size antenna are 2.2% (Gustafsson's limit) and 4.2% (Chu's limit). As shown, the Stacked Step-DRLM antenna has performance that surpasses the limits but it should be noted these lim-

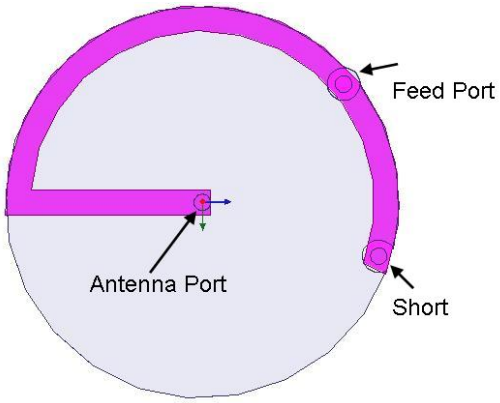

Figure 6.40: Layout for Matching Network

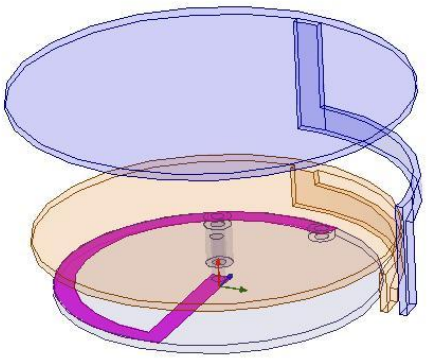

Figure 6.41: Stacked Step-DRLM Design with Matching Network

its are restricted to single-mode antennas and are not valid for multi-mode designs.

Figure 6.43 shows a useful interpretation of the input impedance when the matching network is used to transform the impedance for good match conditions. The knot pattern fits neatly inside a VSWR = 2 circle.

6.4.1 Fabrication and Measurement

The Stacked Step-DRLM antenna is fabricated in the Antenna Lab, using similar techniques to those used for single mode DRLM antenna models. The final constructed antenna is shown in Figure 6.44.

The measured input impedance is shown on the Smith chart in Figure 6.45.

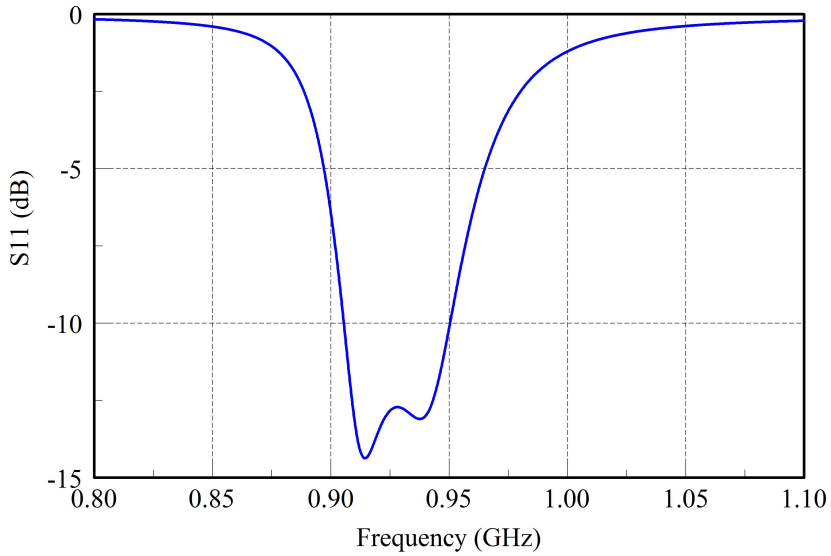

Figure 6.42: Magnitude Response of the Reflection Coefficient (S_{11}) for the Stacked Step-DRLM Antenna with Matching Network (MN)

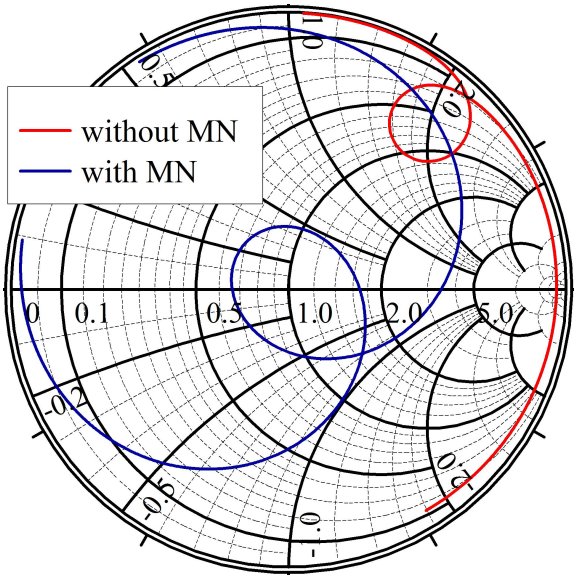

Figure 6.43: Input Impedance for the Stacked Step-DRLM Antenna with Matching Network (MN)

When compared to the simulation there is a noticeable shift in the measured impedance locus. There are often discrepancies between measured and simulated results which can often be attributed to fabrication errors or tolerances. In this case the simulation is used to determine the source of most likely error in fabrication. After back testing in ADS, it is found that the feed point is misplaced by approximately 3 mm. The series line is too long and the stub

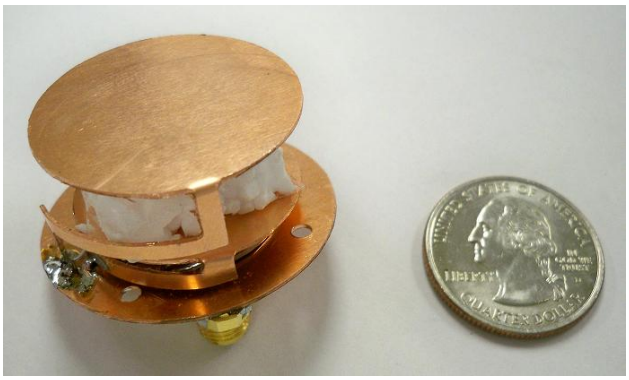

Figure 6.44: Fabricated Stacked Step-DRLM Antenna

section is too short. Figure 6.46 shows the comparison between the measured and simulated results after compensating to re-create the measured data. Though the data is not identical the concept is proven and the remaining differences can be caused by other fabrication effects.

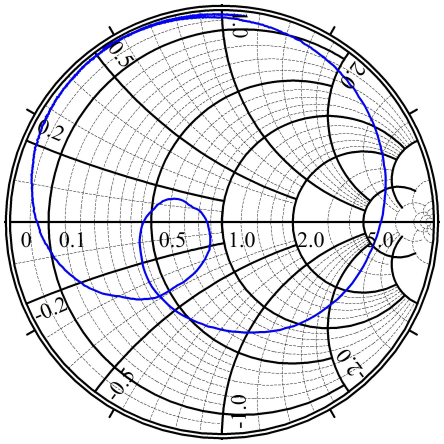

Figure 6.45: Measured Input Impedance for the Stacked Step-DRLM Antenna Shown on Smith Chart

The antenna gain is measured and shown in Figure 6.47. The peak gain is 3.45 dBi at the resonant frequency.

An image of the Stacked Step-DRLM antenna with co-ordinate system axis is shown in Figure 6.48(a) and is to be used as a frame of reference for the measured radiation patterns in Figures 6.48(b), 6.49(a) and 6.49(b). The radiation patterns have the characteristic form of a monopole antenna on a finite-sized ground plane. As expected the cross polarization is relatively high

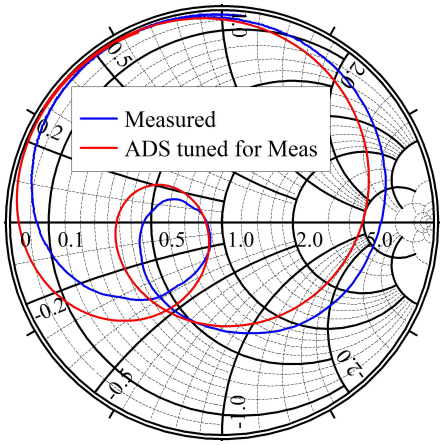

Figure 6.46: Measured Input Impedance Compared to ADS Compensated Simulation

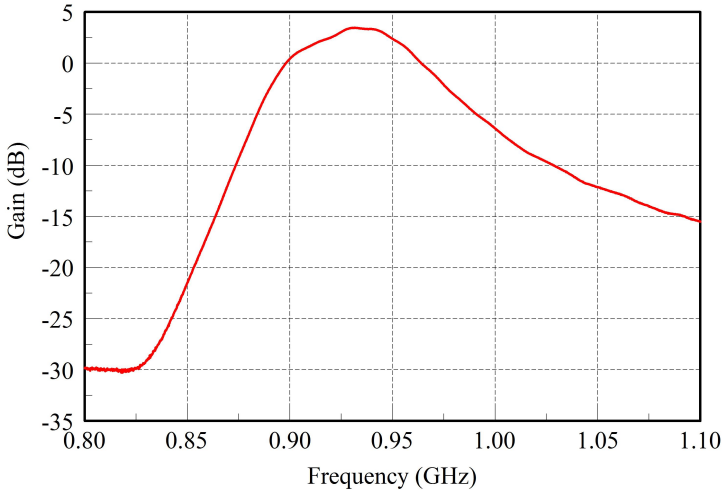

Figure 6.47: Measured Gain vs. Frequency

compared to a traditional monopole due to the presence of the meandered shorting strip.

In this final section of this chapter we explored a broadband design of the DRLM antenna. Using characteristic mode theory we developed design guidelines. The final design exceeded both Gustafsson's and Chu's limits because of its multi-mode operation. This stacked topology for broadbanding is not new but by using the DRLM structure we retain some miniaturization capability.

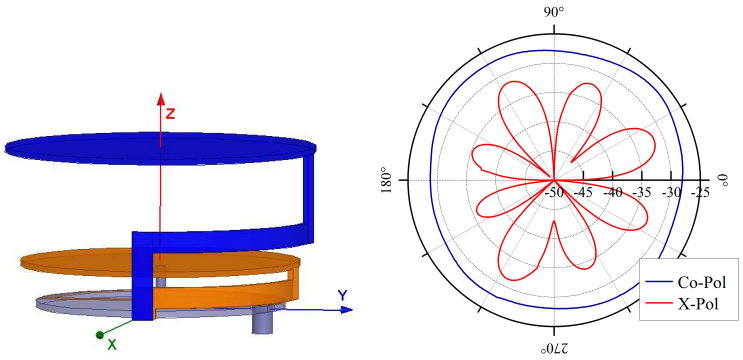

(a) Axis Reference (b) XY Plane

Figure 6.48: Stacked Step-DRLM Antenna Measured Radiation Patterns

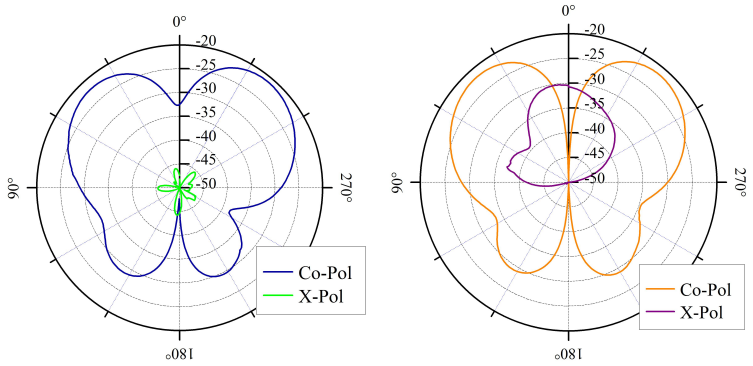

(a) YZ Plane (b) ZX Plane

Figure 6.49: Stacked Step-DRLM Antenna Measured Radiation Patterns

6.5 Summary

A dual reactively loaded monopole antenna is introduced as a solution to the problem of fixed volume applications where small antennas are to be deployed. Various designs are evaluated for tunability and bandwidth-efficiency performance. All antennas are compared to the physical limitations that govern the absolute maximum performance attainable for their size. The implementation of the inductive loading using lumped air core inductors with high Q is investigated and the optimum position for inductor placement for performance is determined. The operation of the DRLM antenna for reduction in the height profile is explained and evaluated. The DRLM antenna was found to be not well suited for use in the short-fat geometry. Finally, a

broadband multi-mode DRLM antenna is designed, simulated and measured. The multi-mode topology achieves a more than doubling of the impedance bandwidth.

CHAPTER 7

CONCLUSIONS

Small antenna theory is well founded in fundamental concepts that define the relationship between radiator performance and electrical size. Thus an antenna cannot be made to operate well independent of size, even though some have suggested that this is possible using metamaterials. The best possible design is one that approaches the defined limit as close as possible. For non-spherical antenna geometry it is more relevant to compare performance to Gustafsson's limit since it provides a more realistic assessment of the potential performance for an arbitrarily shaped antenna. Many reported small antenna designs are not reported against the theoretical limits (as noted by [4]) and even fewer are reported against the Gustafsson limit for the antenna shape. In this document we have consistently given the reader a perspective of the antenna performance relative to the appropriate limits.

Characteristic mode (CM) theory was used extensively as an antenna analysis tool. The CM analysis allowed for the breaking down of complex problems into their individual parts thus simplifying the challenge of determining the method of operation for many of the antennas presented in this document. Two specific antenna structures where we used CM theory to both understand the operation and then to develop useful design guidelines were the Infinite Wavelength Resonant Antenna (or IWRA) and the Stacked Step-Dual Reactively Loaded Monopole (DRLM) Antenna. Both antenna structures involved complex coupling phenomenon where the utility of separating individual modes was critical in understanding the operation of the antenna structure. Also, for the IWRA, the CM analysis revealed the correct position on the antenna which was radiating (i.e., position of radiating edges) which was actually misreported by the authors in [32].

We were able to demonstrate a general traditional analysis approach that provides more insight into operation and design than methods based on metamaterial theory. Using this approach we provide an alternative understanding of operation of a metamaterial antenna and also put its performance into context by comparing it to traditional antennas with similar radiation characteristics. Using this methodology similar antenna topologies (for example, utilizing interdigital capacitors) based on the so-called composite right left handed transmission line concept can be analyzed [38].

A hybrid design is developed that incorporates properties of both the capacitively loaded (commonly referred to as "top-loaded") monopole antenna as well as the inductively load patch antenna or PIFA. This new antenna topology allows for flexibility in design of resonant frequency while keeping the volume the antenna occupies as constant. Herein lies a key contribution to the field of antennas, an antenna that is frequency agile while maintaining a fixed size. A number of geometrical profiles for the shorting trace were studied and the traditional horizontal meander is found to be the outperformer due to its geometry which better utilizes the volume.

High Q-factor inductors are good candidates as loading elements in antenna radiating applications. The performance of a lumped inductor - DRLM antenna is evaluated and its viability as a loading element for antennas is demonstrated. The placement sensitive performance is characterized in both simulation and measurement. The Top position resulted in the best tradeoff between antenna size and performance. Measurements indicate that the lumped inductor loaded antenna has better performance than the distributed models for small ka sizes since it is not subject to the "wrap-around effect." The hybrid implementation (lumped and distributed) shows that a performance improvement can be achieved for light loading (i.e., small inductances).

A simplified circuit model derivation of the DRLM antenna provides the intuitive understanding as to why the patch height is so crucial to the antenna's performance. How the reduction in patch height affects the antenna Q (and consequently the bandwidth) will be of particular focus. Conventional wisdom would be to assume that if the volume remains constant, the

performance should be relatively the same. Alternatively, a height reduction could be offset with a radius increase (cylindrical volume), essentially moving to a short-fat model. This was disproved both in simplified analysis and simulation.

Finally, a multi-mode antenna based on a stacked topology of the single-mode DRLM antenna geometry is designed and evaluated. Using a matching network, an impedance bandwidth of more than double the single-mode DRLM was reported. This concept for bandwidth enhancement has been illustrated using quarter-wave patch antenna elements [51], but using elements with meandered shorting profiles the antenna can be made electrically smaller.

7.1 Future Work

The work in this document has been based on miniaturization of planar-type antenna structures, specifically those derived from the patch antenna geometry. In the future it would useful to examine the miniaturization potential of other planar structures (e.g., spirals, vivaldi etc.). These antenna are relatively wideband for low profile antennas and thus they could prove to be promising candidates for good miniaturization-performance tradeoff.

Based on the lumped inductor - DRLM antenna measurements, the performance is much improved over the distributed line implementations in the low ka regions (where the wrap-around effect degradation phenomenon occurs). There is interest in understanding the outperformance of the lumped inductor implementation. This analysis problem could involve modeling techniques and using the theory of characteristic modes in order to determine the associated Q-factor of the distributed models while comparing to the lumped inductor. Additionally, the use of the lumped inductors in applications for frequency reconfigurability of electrically small antennas can be investigated for viability and effectiveness.

One method for bandwidth enhancement for the DRLM antenna has been presented, future work should include a broad band designs using slot loading

the radiator or ground plane (or some other method). This exercise can be used to gain perspective on the tradeoffs associated will the different methods that can be employed.

REFERENCES

[1] RNCOS E-Services Private Limited. (2010, August). *Global RFID Market Analysis till 2010* [Online]. Available: http://www.researchandmarkets.com/reports/c77745. (URL)

[2] H.A. Wheeler, "Fundamental limitations of small antennas," *Proc. IRE*, vol. 35, pp. 1479-1484, Dec. 1947.

[3] K.L. Wong, *Compact and Broadband Microstrip Antennas*. New York, NY: John Wiley & Sons, 2002.

[4] D.F. Sievenpiper, D.C. Dawson, M.M. Jacob, T. Kanar, K. Sanghoon, J. Long, and R.G. Quarfoth, "Experimental validation of performance limits and design guidelines for small antennas," *IEEE Transactions on Antennas and Propagation*, vol. AP-60, no. 1, pp. 8-19, Jan. 2012.

[5] J.L. Volakis, C.C. Chen, and K. Fujimoto, *Small Antennas: Miniaturization Techniques and Applications*. New York, NY: McGraw-Hill, 2010.

[6] S.R. Best, *Antenna Engineering Handbook*, 4th ed. J.L. Volakis, Ed. New York, NY: McGraw-Hill, 2007, ch. 6: Small Antennas.

[7] H.A. Wheeler, "Small antennas," *IEEE Transactions on Antennas and Propagation*, vol. 23, pp. 462-469, July 1975.

[8] H.A. Wheeler, "The radiansphere around a small antenna," *Proc. IRE*, vol. 47, pp. 1325-1331, Aug. 1959.

[9] L.J. Chu, "Physical limitations of omni-directional antennas," *Journal of Applied Physics*, vol. 19, pp. 1163-1175, Dec. 1948.

[10] R.C. Hansen, "Fundamental limitations in antennas," *Proceedings of the IEEE*, vol. 69, no. 2, pp. 170-182, Feb. 1981.

[11] R.F. Harrington, "Effect of antenna size on gain, bandwidth and efficiency," *J. Res. Nat. Bur. Stand.*, vol. 64-D, pp. 1-12, Jan./Feb. 1960.

[12] R.E. Collin and S. Rothschild, "Evaluation of antenna Q," *IEEE Transactions on Antennas and Propagation*, vol. AP-12, pp. 23-27, Jan. 1964.

[13] R.L. Fante, "Quality factor of general ideal antennas," *IEEE Transactions on Antennas and Propagation*, vol. AP-17, pp. 151-155, March 1969.

[14] A.D. Yaghjian and S.R. Best, "Impedance, bandwidth, and Q of antennas," *IEEE Transactions on Antennas and Propagation*, vol. AP-53, pp. 1298-1324, April 2005.

[15] S.R. Best, "The performance properties of electrically small resonant multiple-arm folded wire antennas," *IEEE Antennas and Propagation Magazine*, vol. 47, no. 4, pp. 13-27, Aug. 2005.

[16] S.R. Best, "Bandwidth and the lower bound on Q for small wideband antennas," *IEEE Int. Symp. on Antennas and Propagation*, pp. 647-650, 2006.

[17] S.R. Best, "The radiation properties of electrically small folded spherical helix antennas," *IEEE Transactions on Antennas and Propagation*, vol. AP-52, no. 4, pp. 953-960, April 2004.

[18] S.R. Best, "Low Q electrically small linear and elliptical polarized spherical dipole antennas," *IEEE Transactions on Antennas and Propagation*, vol. AP-53, pp. 1047-1053, March 2005.

[19] H.L. Thal, "New radiation Q limits for spherical wire antennas," *IEEE Transactions on Antennas and Propagation*, vol. AP-54, pp. 2757-2763, Oct. 2006.

[20] H.L. Thal, "Gain and Q bounds for coupled TM-TE modes," *IEEE Transactions on Antennas and Propagation*, vol. AP-57, no. 7, pp. 1879-1885, July 2009.

[21] M. Gustafsson, C. Sohl, and G. Kristensson, "Physical limitations on antennas of arbitrary shape," *Proceedings of the Royal Soceity A: Mathematical, Physical and Engineering Sciences*, vol. 463, issue 2086, pp. 2589-2607, 2007.

[22] R.W.P. King, *The Theory of Linear Antennas*. Cambridge, MA: Harvard University Press, 1956.

[23] M. Gustafsson, C. Sohl, and G. Kristensson, "Illustrations of new physical bounds on linearly polarized antennas," *IEEE Transactions Antennas Propagation*, vol. 57, pp. 1319-1327, May 2009.

[24] M. Gustafsson, "Polarizability and physical bounds on antennas in cylindrical and rectangular geometries," Lund University, Department of Electrical and Information Technology, Lund, Sweden, Tech. Rep. LUTEDX/(TEAT-7195)/1-11/(2010), 2010.

[25] R.J. Garbacz and R.H. Turpin, "A generalized expansion for radiated and scattered fields," *IEEE Transactions on Antennas and Propagation*, vol. AP-19, pp. 348-358, May 1971.

[26] R.F. Harrington and J.R. Mautz, "Theory of characteristic modes for conducting bodies," *IEEE Transactions on Antennas and Propagation*, vol. AP-19, no. 5, pp. 622-628, Sept. 1971.

[27] R.F. Harrington and J.R. Mautz, "Computation of characteristic modes for conducting bodies," *IEEE Transactions on Antennas and Propagation*, vol. AP-19, no. 5, pp. 629-639, Sept. 1971.

[28] R.J. Garbacz and D.M. Pozar, "Antenna shape synthesis using characteristic modes," *IEEE Transactions on Antennas and Propagation*, vol. AP-30, no. 3, pp. 340-350, May 1982.

[29] D. Liu, R.J. Garbacz, and D.M. Pozar, "Antenna synthesis and optimization using generalized characteristic modes," *IEEE Transactions on Antennas and Propagation*, vol. AP-38, no. 6, pp. 862-868, June 1990.

[30] R.F. Harrington and J.R. Mautz, "Control of radar scattering by reactive loading," *IEEE Transactions on Antennas and Propagation*, vol. AP-20, no. 4, pp. 446-454, July 1972.

[31] M. Cabedo-Fabrés, E. Antonio-Daviu, A. Valero-Nogueira, and M.F. Bataller, "The theory of characteristic modes revisited: A contribution to the design of antennas for modern applications," *IEEE Antennas and Propagation Magazine*, vol. 49, no. 5, pp. 52-68, Oct. 2007.

[32] A. Lai, K.M. Leong, and T. Itoh, "Infinite wavelength resonant antennas with monopolar radiation pattern based on periodic structures," *IEEE Transactions on Antennas and Propagation*, vol. AP-55, no. 3, pp. 868-876, March 2007.

[33] B.A. Munk, *Metamaterials: Critique and Alternatives*. New York, NY: John Wiley & Sons, 2009.

[34] V.G. Veselago, "The electrodynamics of substances with simultaneously negative values of permittivity and permeability," *Soviet Physics Uspekhi*, vol. 10, no. 4, pp. 509-514, 1968.

[35] R.A. Shelby, D.R. Smith, and S. Schultz, "Experimental verification of a negative index of refraction," *Science*, vol. 292, pp. 77-79, 2001.

[36] J.B. Pendry, A.J. Holden, D.J. Robbins, and W.J. Stewart, "Magnetism from conductors and enhanced nonlinear phenomena," *IEEE Transactions on Microwave Theory and Techniques*, vol. 47, no. 11, pp. 2075-2084, 1999.

[37] C. Caloz and T. Itoh, *Electromagnetic Metamaterials: Transmission Line Theory and Microwave Applications*. New York, NY: John Wiley & Sons, 2006.

[38] A. Sanada, M. Kimura, I. Awai, C. Caloz, and T. Itoh, "A planar zeroth-order resonator antenna using a left-handed transmission line," *34th European Microwave Conference*, Amsterdam, vol. 3, pp. 1341-1344, Oct. 2004.

[39] C. Caloz, H. Okabe, T. Iwai, and T. Itoh, "Transmission line approach of left-handed (LH) materials," *Proceedings USNC/URSI National Radio Science Meeting*, San Antonio, TX, 2002.

[40] D. Sievenpiper, L. Zhang, F.J. Broas, N.G. Alexopulos, and E. Yablonovitch, "High-impedance electromagnetic surfaces with a forbidden frequency band," *IEEE Transactions on Microwave Theory and Techniques*, vol. 47, pp. 2059-2074, Nov. 1999.

[41] F.J. Herraiz-Martinez, V. Gonzalez-Posadas, L.E. Garcia-Munoz, and D. Segovia-Vargas, "Multifrequency and dual-mode patch antennas partially filled with left-handed structures," *IEEE Transactions on Antennas and Propagation*, vol. AP-56, no. 8, pp. 2527-2539, Aug. 2008.

[42] J. Zhu and G.V. Eleftheriades, "A compact transmission-line metamaterial antenna with extended bandwidth," *IEEE Antennas and Wireless Propagation Letters*, vol. 8, 2009.

[43] D. Schaubert, F.G. Farrar, A. Sindoris, and S.T. Hayes, "Microstrip antennas with frequency agility and polarization diversity," *IEEE Transactions on Antennas and Propagation*, vol. AP-29, no. 1, pp. 118-123, Jan. 1981.

[44] H. Pues and A. Van De Capelle, "Accurate transmission-line model for the rectangular microstrip antenna," *IEE Proceedings*, vol. 131, Pt. H, no. 6, Dec. 1984.

[45] D.M. Pozar, *Microwave Engineering*, 3^{rd} ed. New York, NY: John Wiley & Sons, 2005.

[46] R. Waterhouse, *Printed Antennas for Wireless Communications*. New York, NY: John Wiley & Sons, 2007.

[47] J.R. James, P.S. Hall, and C. Wood, *Microstrip Antenna Theory and Design*. IEE Electromagnetic Wave Series 12, London, Peter Perigrinus, pp. 102-107, 1981.

[48] Coilcraft, "Midi Spring Air Core Inductors," Datasheet Doc # 184-1 and 184-2, May 2012.

[49] Coilcraft, "Transmission Line Model: Midi Springs," Datasheet Doc # 346-1 and 346-2, Feb. 2008.

[50] R. Hansen, "Efficiency and matching tradeoffs for inductively loaded short antennas," *IEEE Transactions on Communications*, vol. 23, no. 4, pp. 430-435, April 1975.

[51] J. Ollikainen, M. Fischer, and P. Vainikainen, "Thin dual-resonant stacked shorted patch antenna for mobile communications," *Electronic Letters*, vol. 35, pp. 437-438, March 18, 1999.